Temperature dependence of slip deformation under monotonic/cyclic stresses in Ti-6Al-4V

アンネ, バーガヴィ, ラーニ

Temperature dependence of slip deformation under monotonic/cyclic stresses in Ti-6Al-4V

Ti-6Al-4V における単一および繰返し応力下での辷り変形挙動とその温度依存性に関する研究

Kyushu University

2020

Bhargavi Rani Anne

Temperature dependence of slip deformation under monotonic/cyclic stresses in Ti-6Al-4V

Ti-6Al-4V における単一および繰返し応力下での辷り変形挙動とその温度依存性に関する研究

By: Bhargavi Rani Anne

Supervisor: Professor Masaki Tanaka

A thesis submitted to the Graduate Studies Office in Fulfillment of the Requirements for the Degree of Doctor of Engineering

Department of Materials Process Engineering,

Kyushu University, Fukuoka, Japan

March 2020

Dedicated

To parents

To the teachers who have inspired me

Acknowledgments

I would like to express my profound gratitude to my supervisor Prof. Masaki Tanaka for his excellent guidance throughout my Ph.D. Firstly, I would like to thank for choosing me to this work. He always encouraged me to think independently and asked several significant questions many times to acquire in-depth knowledge. His constructive criticism always headed for betterment in the work and writings as well. Not only the research techniques and technical knowledge, but I also learned many professional ethics, being dedicated to work and to the society as well which inspired me to look up to him. I believe, whatever I learned from him in these years will be helpful throughout my entire life.

My sincere thanks to Prof. Toshihiro Tsuchiyama and Prof. Hirofumi Miyahara for spending their valuable time to evaluate my thesis. Their impeccable suggestions and critical comments contributed to the betterment in presenting the thesis. I also would like to appreciate the support given whenever possible by Dr. Tatsuya Morikawa, Assistant Professor of Tanaka Lab. My heartfelt thanks to Late.Prof. M.C. Valsakumar, for his generous support and for his immense dedication to the work that made me to become much more disciplined.

I extend my sincere thanks to Dr. VVSS Srikanth, Assoc. Prof., SEST, UoH, for his support and valuable suggestions in career. I would like to thank my previous supervisors, Asst. Prof. Swati Ghosh Acharyya, Asst. Prof. Prasant Jyoti Gautam, Assoc.Prof. M.R.Majhi for their contributions in improving my research abilities. Also, my sincere thanks to all the teachers in my life. I also would like to acknowledge the help of Dr. Yelm Okuyama, former post-doctoral fellow, Tanaka lab; I thank him for sharing his valuable opinions and inputs to the work.

I would like to thank Japanese government for providing financial support through MEXT during my Ph.D. I would like to extend my thanks to Mr. Tatsuo Yokote, Senior Technical staff of Tanaka lab for making and taking care of equipment very well. Also, thanks to Mrs. Yumi Shimada for helping in documentation whenever required. I also would like to

thank Ms. Yasura Oiwa, student support division, Kyushu University, for her kind welcoming nature, for the documentation and for her patience in answering many doubts with a kind gesture.

I thank all the students of Tanaka lab during these three years for their help and support; for creating a friendly atmosphere in the laboratory. Special thanks to Mr. Yukihiro Hayashi and Mr. Karokaro Haranas, who graduated from Tanaka lab, for teaching me the operation of equipment and for the help whenever required. I also appreciate the help of Mr. Imayama and Mr. Yoshida from the day one. I also wish to thank the staff of Ultramicroscopy Research Center, Kyushu University for their worthwhile support and guidance during the usage of equipment. I also thank the staff of Kyushu University library, Fukuoka City library, Fukuoka-shi Seibu library for their patience and kindness.

At last and foremost, my heartfelt thanks to my parents for giving me this life, for their unconditional love & support, for not restricting my abilities and for allowing me to achieve my dreams. Special thanks to my brother for his unconditional love and support, for helping me in difficult situations and for sharing his ideologies to make me think better. My heartfelt thanks to my schoolteacher and friend Ms. Pavani for always encouraging and motivating me in difficult situations. Thanks are due to teaching me the ethics, and thanks for sharing her knowledge and philosophies in many areas to broaden my views on many things. Special thanks to Ratna aunty for her valuable and experienced guidance in my personal and professional life as well. Special mention to my friend Shajahan for always discussing the basic concepts of MME, for criticizing me constructively. Many thanks to Matsuo Tsuji san and his wife Junko Tsuji san for their absolute warmness and kindness, for introducing me to many Japanese traditions, for helping in all the difficult situations that made my stay in Fukuoka much more comfortable. Thanks to my friend Sakamoto for his help several times during the stay in Fukuoka. Finally, Thanks to my friend Karuna, for being a stress reliever in all the difficult situations of my life especially during the last three years. I am nowhere in this position comfortably without their contributions in my life.

Abstract

Over the period of years, Ti alloys have been commercially used in several applications notably in aerospace and biomedical industries peculiarly Ti-6Al-4V. Temperature dependence on the mechanical properties concerning on thermally activated processes has been investigated in the specimens with single phase α alloys such as CP-Ti and Ti-Al, and dual phase alloys such as Ti-6Al-4V. As Ti-6Al-4V is available in many microstructures, it is difficult to comprehend or compare the mechanisms between them. The most complex microstructure is the one containing multiple phases with different crystal structures. Bimodal microstructure is one among them. The mechanism behind the temperature dependence of mechanical properties in such alloys is much more complicated. Therefore, the present thesis dedicated to elucidating the mechanisms behind thermally activated processes that involved in the deformation mechanisms of Ti-6Al-4V.

In Chapter 1, the temperature dependence on the mechanical properties is reviewed for α alloys, β alloys, and α + β alloys. Although the mechanism behind the temperature dependence of α alloys has been well studied, the mechanism in commercial alloys such as Ti-6Al-4V which consists of both α and β phases have not been well discussed yet because of the complexity of its microstructure. It was stressed that it is important to understand the mechanisms behind thermally activated processes involved in the deformation of Ti-6Al-4V to enhance the utilization of titanium alloys.

In Chapter 2, the temperature dependence of fundamental mechanical properties in bimodal Ti-6Al-4V was obtained, concluding several points. Temperature dependencies of yield stress and effective stress change in their trends approximately between 225 K and 300 K. The trend of the temperature dependence of effective stress suggests the controlling mechanisms behind yielding changes at the temperature range between 225 K and 300 K. Activation volume increases with temperature except for the temperature range between 225 K and 300 K. The

temperature dependence of the activation enthalpy obtained in this study suggests that both basal and prismatic slips are dominant at yielding. Thus, there is a great need to study the change in slip activity at those temperatures as thermally activated processes, which was investigated in the next chapter.

In Chapter 3, in order to assess the activated slip systems which associated with the change in the trend of effective stress, the temperature dependence of activated slip systems was investigated. The trace analysis and Schmid factor distributions indicated that basal slips are dominant at 77K, both basal and prismatic slips were identically dominant at 225 K, and pyramidal slips were dominant at 550 K. The onset of the pyramidal slips should lead to the change in the trend of the temperature dependence of effective stress approximately 325 K, *that is*, the change in the dominant active slip systems with temperature can explain the change in the trend of temperature dependence of the effective stress approximately at 325 K.

In Chapter 4, the expanded usage of Ti-6Al-4V in aerospace, structural and biomedical application necessitates the study on fatigue properties. The study on deformation mechanisms under monotonic loads also intensives to extend the work on to determine deformation mechanisms under cyclic loads. The major intention is to interpret the evolution of temperature dependence of fatigue crack propagation with the change in the stress ratio. The effect of stress ratio on the temperature dependence of fatigue crack propagations was investigated. Fatigue crack growth rates were nearly independent of temperature in cases of R = 0.1, 0.7, and 0.8 while it is dependent on temperature in case of R = 0.9. It can be explained by the assumptions that the fatigue crack growth is controlled by the dislocation activities with respect to work-hardening in the conditions of $R \leq 0.8$ while it is controlled by dislocation glide in the condition of R = 0.9. The change in the temperature dependence of the fatigue crack growth rate also suggests the change in the distance between a dislocation source and a crack tip.

In Chapter 5, all results obtained in this study are summarized. It was concluded that the controlling mechanisms behind temperature dependence of yield stress and fatigue crack growth rate with $R \leq 0.8$ are not the same. However, the fatigue crack growth rate with $R = 0.9$ is expected to be controlled by dislocation glide.

Table of Contents

Chapter 1 Introduction

1.1 Overview of Titanium alloys

Titanium is one of the youngest and promising structural alloys as well as an excellent biomaterial. Titanium is preferable over other materials due to having a combination of excellent physical properties, mechanical properties, and corrosion properties such as high specific strength, good creep resistance, high longevity due to greater fatigue resistance, improved ductility without compromising strength in some of its alloys, better oxidation resistance, etc. Titanium is renowned as strong metal with low density in combination with ductility, particularly at oxygen-free environments. Titanium grabs attention for many desirable applications due to its par excellence in acquiring a combination of key properties. Titanium also referred to as refractory metal due to having an apparently high melting point *i.e.* around 1940 K. Titanium alloys can be used at both ends of temperatures from cryogenic to higher temperatures. Many researchers have contributed enormously to develop and improve the properties of titanium and its alloys for the last few decades. Though titanium developed over 50 decades ago, the fundamental theories in deformation correlating dislocations are still ambiguous. Because it has excellent properties but high production costs due to the high affinity towards oxygen and nitrogen many researchers have dedicated to build fundamentals in deformation and to reduce underlying economic cost [1–6].

1.2 History and utilization of titanium and its alloys

Titanium exists all over the universe, such as in the stars, in interstellar dust, or in meteorites. Titanium universally expanded and is the fourth most abundant structural material in the earth's crust with a concentration of 0.6% after aluminum, iron, and magnesium. The only available source of titanium is in its mineral forms viz., ilmenite, titanomagnetite, rutile, anatase, and brookite. Amongst them, ilmenite and rutile are the important sources of titanium.

The foundation of titanium commenced after early traces of titanium in the 17th century. M. H. Klaproth first discovered the source of titanium as an oxide in rutile, which was an unknown element in 1790. Around the corner, W. Gregor suspected there should be a different element other than Fe and O in dark and magnetic iron sand which was ilmenite ($FeTiO_3$) in 1791. Titanium is named according to Greek mythology as it is hard to extract the ore, which was derived from the Titans, the powerful sons of the earth, the children of Uranos and Gaia [1,6].

It was focused to develop the properties of titanium started over a century around the 1950s during world war. One of the outstanding developments is the advancement in the production of titanium. In the early days, titanium was obtained from $TiCl_4$ using Na or Mg, which outcomes brittle natured titanium. After several years of dedication and attempts, the renowned "Krolls" process came into limelight developed by Kroll in the 20th century. Krolls process involves the reduction of $TiCl_4$ by magnesium under an inert gas atmosphere which consequences in "titanium sponge". The first commercial Titanium was produced by DuPont company in 1948 and the first commercial mill products were by TMCA (Titanium Metals Company of America), later the high production was handled by TIMET (1951), Osaka Titanium and Toho Titanium (1952) and RMI (1958) [4,7–9]. The development in titanium alloys came into widespread after the first international conference held on titanium [2,10]. Almost 30 commercial titanium alloys were occupied in the market by 1972. Ti-6Al-4V, Ti-5Al-2.5Sn, Ti-8Al-1Mo, Ti-6Al-4V-2Sn and Ti-13V-11Cr-3Al alloys are commercially favorable, which accounted for 90% of titanium sales [11].

Many accomplished researches were available on alloy development accordingly with microstructures such as α-alloys, α+β alloys and β-alloys including processing, improving properties and reducing cost etc., In the earliest stages of the development of titanium alloys, 90% alloys were developed for aerospace applications, which increased the production of titanium world-widely, and increased the production of commercially pure (CP) titanium for

non-aerospace applications. Later on, titanium and its alloys dispersed towards other applications such as biomaterial products. Titanium and its alloys are widely applied in the aerospace industry from the early stages of evolution of the metal, which includes airframes and aero-engines. The historical growth of titanium in aerospace increased peculiarly after being used in Boeing airframes. The well-known first commercial airplane, Boeing 777, 10% of her airframe weight occupied by a classical titanium alloy, *i.e.* Ti-6Al-4V. Components of aero-engine are designed with titanium alloys, and landing gears are made of β-Ti alloys [4,12,13]. Ti-6Al-4V outweighs 50% of aerospace applications [14]. The usage of titanium alloys in an aero-engine is as shown in Fig.1.1.

Apart from aerospace applications such as jet engines, space crafts, missiles [13,15], titanium alloys are widely used in turbine engines [16–19], marine applications [20–22], biomedical implants, devices [23–28], coatings [29–31], heat exchangers [17,22,32,33], and automotive parts [34] as shown in Fig. 1.2. Ti-6Al-4V is used in sporting goods such as golf club heads, tennis rackets, bicycle components [35,36], etc. One of the major applications of titanium is structural materials [35,37,38]. Some monuments in the world were made of titanium such as the monument of Yuri Gagarin who was the first man to the space, and the conquerors of space. Guggenheim Museum Bilbao, which is the first titanium building of Europe as shown in Fig. 1.3., Fig. 1.4. shows a multi-purpose dome named originally as Fukuoka Dome, which has a retractable titanium roof made for all weather-purposes [5,35,39] as shown in Fig. 1.4.

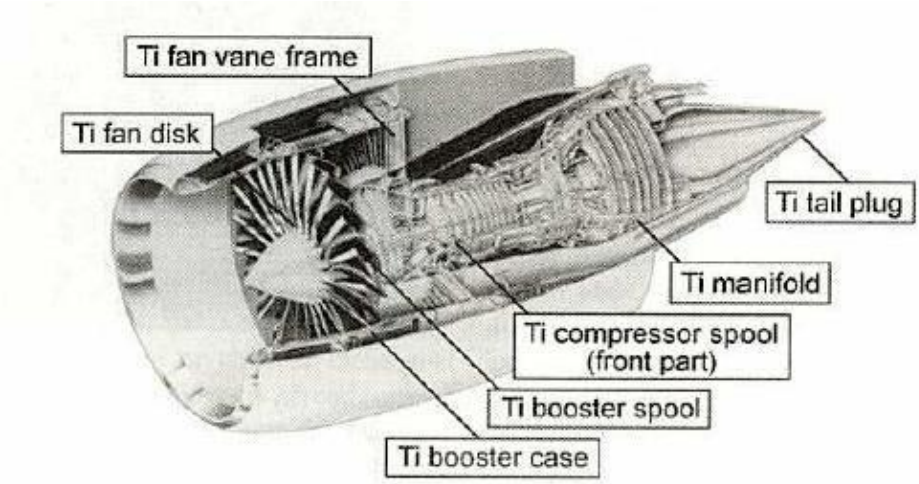

Figure 1.1. Titanium usage in GE-90 aero-engine [5].

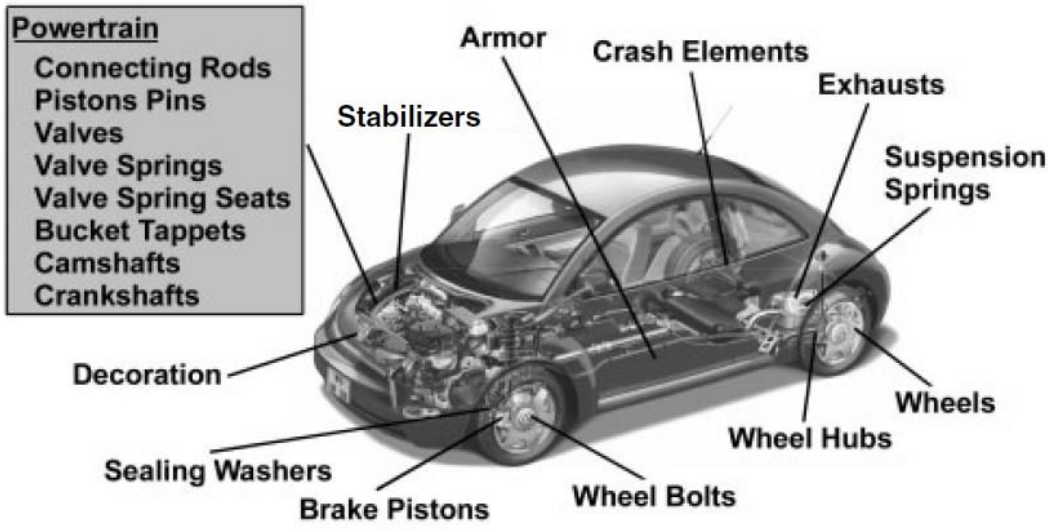

Figure 1.2. The possible applications of titanium for vehicles [34].

Figure. 1.3. Titanium cladding to the Guggenheim Museum Bilbao [35].

Figure. 1.4. Fukuoka dome (originally named) with a retractable titanium roof [5].

1.3 Physical metallurgy of titanium alloys:

Fundamental theories behind the properties of Titanium are complex as well as fascinating. Titanium comes under the classification of nonferrous and light metal with density of 4.51 g/cm^3 which is approximately one half of iron and nickel. Titanium is non-magnetic and exhibits poor conductivity towards heat and electricity. Solid-state transformation, i.e. a material transforming from one crystal structure to another at a specific temperature is called as allotropic transformation. The transformation temperature is known as transus temperature. Pure titanium undergoes an allotropic transformation between α phase, *i.e.* hexagonal close-packed (HCP) at room temperature and β phase, i.e. body centered cubic (BCC) at high temperatures. The transus temperature is highly sensitive to the alloy composition. Pure titanium undergoes an allotropic transformation at around 882°C. The possession of a wide range of properties of Ti alloys is predominantly associated with the allotropic transformation temperature as the deformation and diffusion are influenced by the crystal structure.

Generally, titanium alloys are classified into four different categories based on their phase stability. The first one is α alloys which are developed by α stabilizers such as Al, O, N, C, B, Ga, and Ge. α alloys come under non-heat treatable alloys. CP-Ti, Ti-6Al, Ti-8Al-1Mo-1V and Ti-5Al-2Sn-ELI are some of the commercial alloys of α alloys. The second category is near α alloy. These alloys contain little amount of ductile β phase with nearly 2% of β stabilizers such as V, Mo, and Nb. Ti-5Al-5Sn-2Zr-2Mo and Ti-6Al-2Sn-4Zr-2Mo are the best examples of β alloys. The third type of alloys is α+β alloys that are alloyed by both α and β stabilizers. α+β alloys are heat treatable alloys. Ti-6Al-4V, Ti-6Al-6V-2Sn, Ti-6Al-7Nb, and Ti-6Al-4V-ELI are widely used and most successful alloys of this class. Fourth most titanium alloys are β and near β alloys that are comprised of sufficient β stabilizers which help to stabilize β phase in the alloy during quenching. Beta stabilizers are subdivided into two categories viz., β-isomorphous: V, Mo, Nb, Ta and β-eutectoid: Fe, Mn, Cr, Ni, Cu, H, Si are helpful to obtain β

eutectoid systems. Generally, β alloys are solution-treated and aged to improve the mechanical properties such as strength, hardness, and toughness. Beta alloys are also renowned to have metastable alloy phases. Some of the famous β alloys are Ti–29Nb–13Ta–4.6Zr, Ti-8Mo-8V-2Fe-3Al, Ti-13V-11Cr-3Al, etc., Zr, Sn, Hf are considered as neutral for stabilizing the phase. They have no influence on microstructure rather they strengthen α phase mechanically. Alloying elements greatly affect the transus temperature as well as mechanical properties. The effect of alloying elements on phases is as shown in Fig. 1.5. Each element has different solubility compatibility with Titanium [1,11,33,36]. Titanium alloys are classified based on their microstructure and chemical composition at room temperature.

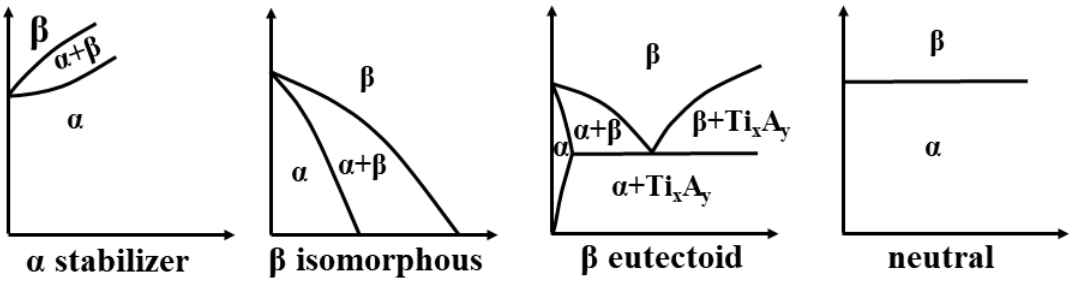

Figure. 1.5. Effect of alloying elements on phase diagrams of titanium alloys.

1.4 Alpha alloys

1.4.1 Commercially pure titanium

The crystal structure of α Ti is as shown in Fig. 1.6. Mostly, the microstructures of α and near-α Ti alloys have nodular grains with different grain morphologies or have secondary phases depending on the processing conditions and heat treatments. The microstructure of near α alloys contains a low amount of dispersions of a β phase in between the α phases. Commercially Pure Ti (CP-Ti), titanium with interstitial impurities also comes under α alloys. Universally, titanium without impurities is not commercially useful for several applications as they lack desired properties. Also, β phase cannot be obtained at room temperature with unalloyed titanium even with the highest cooling rates because it rather transforms into α′ martensitic phase. The yield strength and the ultimate tensile strength of pure Ti is approximately 110 MPa and 250 MPa, respectively, with 72% relative elongation and 820 MPa Vickers hardness. On the other hand, titanium with interstitial impurities endures ultimate tensile strength up to 550 MPa in which oxygen contributes to a great extent and nitrogen to little part. The β-transformation range of CP-Ti varies between 865 °C and 920 °C as a result of the addition of oxygen and nitrogen [4].

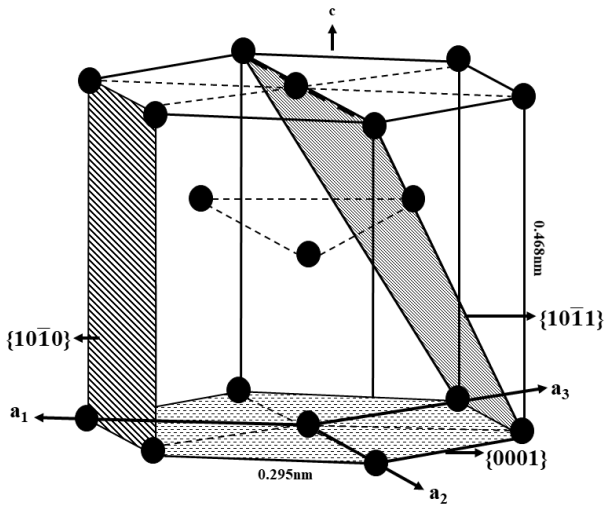

Figure 1.6. Unit cell and crystal structure of α titanium.

CP-Ti is widely used as a pure Ti due to the advantages of CP-Ti over pure Ti. Many studies focused on CP-Ti with varying interstitial contents. The microstructure and properties of Ti alloys are highly influenced by minute changes in composition and processing. The processing of CP-Ti or α alloys majorly concerns on controlling crystallographic nature and grain size as the microstructure cannot be tailored as much as are in α+β alloys and β alloys. The large production of CP-Ti available in rolled products. Vacuum arc-melted ingots are forged to make slabs with a uniform grain size, then rolled. Extensive cold working can be done to produce α alloys which have high strength of titanium. Furthermore, recrystallization is performed after the cold working as the cold-worked titanium lacks in ductility, which is unfavorable for further manufacturing options. The detailed processing procedure is as shown in Fig. 1.7. There are two important processing parameters that need to be considered: the degree of deformation in processing step II and the annealing temperature in step III. The former controls both texture intensity and α grain size, and the latter controls α grain size [40].

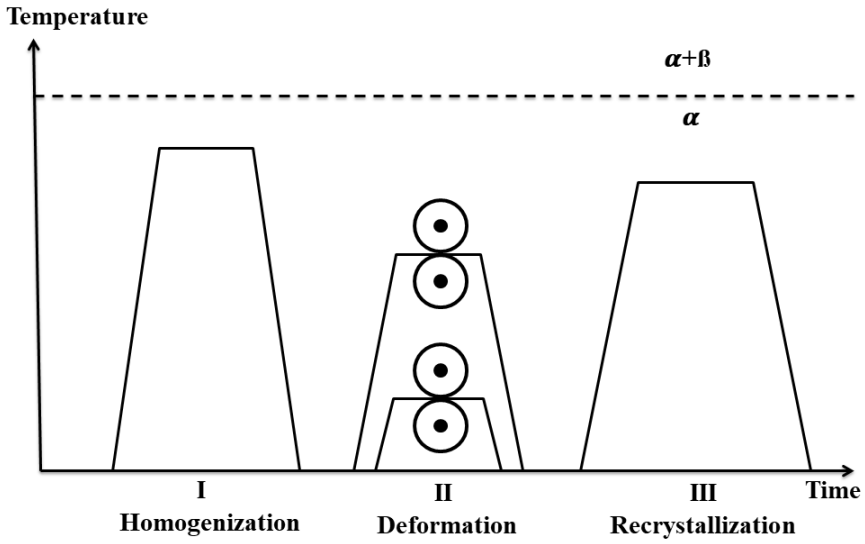

Figure. 1.7. Processing steps in the production of CP-Ti and α Ti alloys.

Figure 1.8 shows a schematic of three slip systems for α titanium alloys, which are basal, prismatic, and pyramidal. The details of possible slip systems in α-Ti are given in Table 1.1. Basal of $\{0001\}$, prismatic of $\{10\bar{1}0\}$, and pyramidal of $\{10\bar{1}1\}$ deform against the slip direction of $< 11\bar{2}0 >$ which is a $\vec{a}$ type Burgers vector. There is a possibility of slip on $\{11\bar{2}2\}$ planes for prismatic and pyramidal against the direction of $< 11\bar{2}3 >$ which is a $\vec{c} + \vec{a}$ type Burgers vector. $\{11\bar{2}2\}$ slip planes have a higher Schmid factor in the case that the stress axis is parallel to the c-axis as shown in Fig.1.8. Prismatic slip is the easiest to be activated in CP-Ti amongst three slip systems due to low CRSS particularly at lower temperatures. Additionally, twinning is more prominent in CP-Ti over alloyed Ti. Twinning contributes to the ductility of CP-Ti especially at low temperatures, where $\{10\bar{1}2\}$, $\{11\bar{2}1\}$ and $\{11\bar{2}2\}$ are the primary twinning planes. Twinning deformations are very crucial to achieve plastic deformation and ductility when the stress axis is parallel to the c-axis as the dislocations on basal slip hindered [41] in CP-Ti. Twinning plays an important role only in pure titanium or CP-Ti with low oxygen content as the solute content such as oxygen, aluminum suppresses the twinning occurrence in α-Ti [42]. Also, oxygen concentration over 0.25 mass% changes a slip character from wavy to planar due to the strain localization and reduction of twinning. However, the effect of oxygen on deformation modes of CP-Ti is consistent only up to 300°C [43].Table. 1.1. Possible slip systems in hexagonal α phase [41,44].

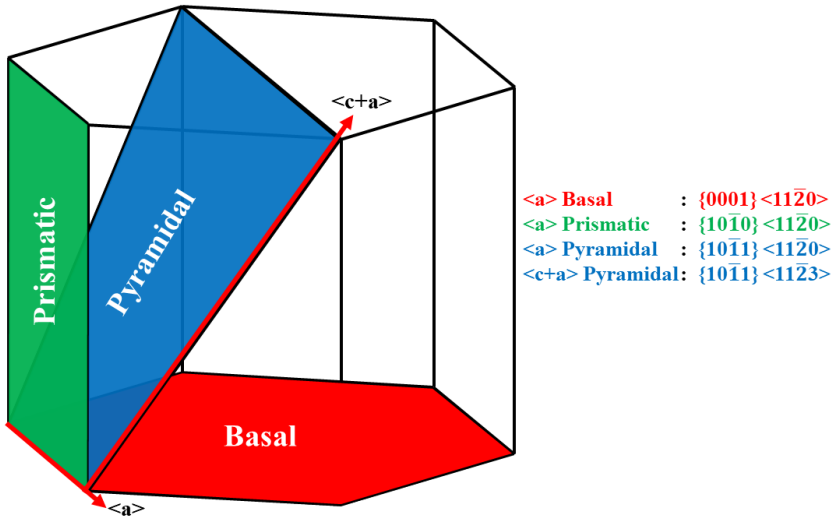

Figure. 1.8. Possible slip systems in alpha phase

Table.1.1. Possible slip systems in alpha phase.

Type of slip system	**Burgers vector**	**Slip direction**	**Slip plane**	**No. of slip systems**	
				Total	Independent
1	$\vec{a}$	$< 11\bar{2}0 >$	$\{0001\}$	3	2
2	$\vec{a}$	$< 11\bar{2}0 >$	$\{10\bar{1}0\}$	3	2
3	$\vec{a}$	$< 11\bar{2}0 >$	$\{10\bar{1}1\}$	6	4
4	$\vec{c} + \vec{a}$	$< 11\bar{2}2 >$	$\{11\bar{2}2\}$	6	5

As CP-Ti only has interstitial impurities as alloying elements, the properties of CP-Ti are greatly influenced by the slight changes in interstitial contents such as oxygen in the majority, nitrogen, and carbon in minority. There are three basic strengthening mechanisms in CP-Ti: solid solution strengthening due to interstitial oxygen, nitrogen, and carbon [45–49]; strengthening by crystallographic orientations [50]; grain boundary strengthening known as Hall-Petch effect [51,52]. The ultimate tensile strength (UTS) of CP-Ti increases of 60 MPa with the 0.05 mass% oxygen content, 125 MPa with 0.05 mass% nitrogen, and 35 MPa with 0.05 mass% carbon. Though iron forms a substitutional solid solution in titanium, it only increases the ultimate tensile strength of 10 MPa with 0.05 mass% addition. The addition of silicon from 0 % to 16 mass% can largely vary the Vickers hardness from 1470 MPa to 6320 MPa, suggesting that 1 mass% silicon contributes to 300 MPa increase in UTS of titanium. The addition of nitrogen above 0.5 mass% is not much commercially used as it induces embrittlement in titanium. Carbon is not utilized as much as it enhances the formation of brittle carbide phase at above 0.2 mass% [53]. Aluminum is the most significant alloying element among α stabilizers as it changes not only mechanical properties but also slip characteristics of deformation. Thus, it is essential to review a Ti-Al system.

1.4.2 Ti-Al binary alloys

Figure 1.9 shows a phase diagram of Ti-Al. Ti with up to 10 at% Al does not evidence any intermetallic secondary phases. Aluminum is the most consistent and substantial substitutional element in titanium alloys. The processing of Ti-Al binary alloys is similar to that of CP-Ti as shown in Fig. 1.7. However, the evolution of secondary phases or precipitates depends on the solution treatments and aging. The crystal structure and deformation modes of Ti-Al are nearly the same as those of CP-Ti as shown in Fig. 1.6., and Fig. 1.8., respectively. Although there are many arguments on the change in c/a ratio with aluminum addition, it has

not been well established. According to Fitzner *et al* [54], c/a ratio increases nonlinearly with the aluminum concentration in both recrystallized and aged specimens, which suggests the ease of activation of basal slip in Ti-Al alloys. However, there is no direct relationship shown between c/a ratio and CRSS.

Aluminum addition brings many changes in the mechanical properties of titanium. It reduces elongation to failure [55] and leads to unstable shear [56]. Addition over 10 at% aluminum completely eliminates twinning according to Lutjering *et al* [5,56]. Al addition is usually considered to induce solid solution strengthening, especially in α phase. However, Sakai and Fine [57] reported that at certain concentrations of aluminum, the material undergoes solid solution softening by scavenging of interstitials. On the basis of hardening of crystals by solute atoms can be classified into rapid hardeners which produce large hardening per atom and lesser hardeners as they produce lesser hardening per atom. Among the substitutional elements in titanium, aluminum is considered to be the rapid hardener as it produces large and asymmetrical strains. Hence, aluminum interacts with both edge and screw dislocations, inducing very strong contribution to the increase in CRSS. Figure 1.10 shows the effect of several α stabilizers which contribute to the hardening of titanium, where the x-axis is a misfit parameter with respect to edge or screw dislocations, and solutions. Y-axis is the increase rate of yield stress with the concentration of elements. Fig. 1.10 (a) and (b) shows the solute atoms interactions with edge dislocations and screw dislocations, respectively. Aluminum equally and strongly interacts with both edge and screw dislocations that contributes to the hardening of the alloy [58,59]. The most significant change in titanium by the addition of aluminum is the change in CRSS of basal and prismatic slips. The ratio of CRSS of basal to the prismatic decreases as aluminum concentration increases due to the substantial increase of CRSS in prismatic slip. The detailed effect of aluminum on CRSS pertaining to Ti-6Al would be explained in the next section, i.e. mechanical behavior of titanium alloys.

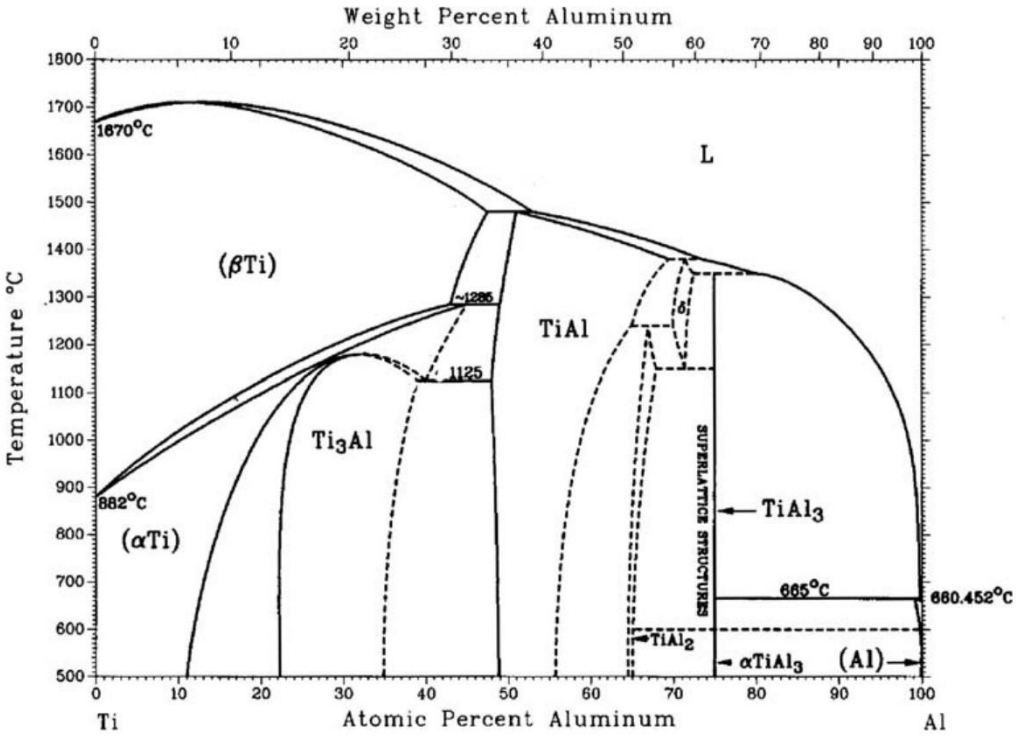

Figure. 1.9. Phase diagram of Ti-Al [60].

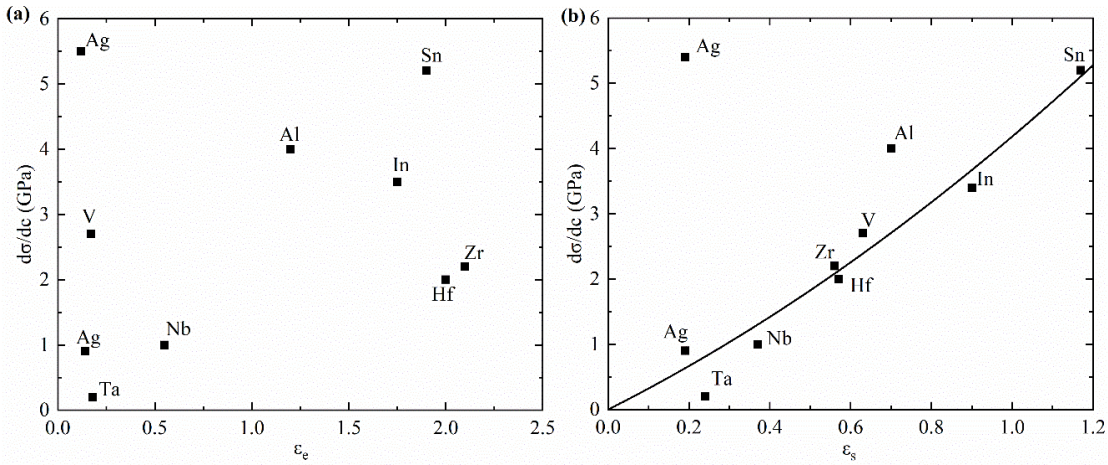

Figure. 1.10 Substitutional solid solution strengthening of α phase. (a) resulted from the interaction with edge dislocations [58], (b) interaction with screw dislocations [59].

1.5 Beta alloys

The alloys with the microstructure of β phase in many forms such as lathe, needle-like, lamellae are known as β alloys. The unit cell and crystal structure of β Ti are shown in Fig.1.11, indicating the densest packed plane of BCC *i.e.* {110}. <111> direction is the nearest direction of an atom in BCC with four equivalent directions. In general, 100 % transformation of the β phase to martensite is nearly impossible, thus the metastable β phase retains. Thus meta stable β alloys are highly prone to show artifacts of martensitic phase even under minimal applied stress such as stress-induced martensite during mechanical polishing, irradiation of X-Ray during characterization which are disappeared after immediate electropolishing [61–63].

β alloys shall contain different forms of secondary precipitates or phases, depending on the processing history and heat treatments. The metastable β phase is transformable to very fine platelets of α phase with high volume fractions [64,65]. Generally, the concentration of β stabilizers defines the stability of β phase as shown in Fig. 1.12. However, stable β alloys are ruled out from commercial materials as the metastable β alloys are well-established as commercially successful alloys due to acquiring desired properties compared to stable β alloys. Metastable β alloys are situated in the equilibrium (α+β) phase region as shown in Fig. 1.12. Transition metals are used as β stabilizers. The prominent attribute of β alloys is that they can be hardened to obtain higher yield stresses than those of α alloys and α+β alloys. β transus temperature decreases to a great extent as the concentration of β stabilizers increases, which enables the manufacturing processing done at lower temperatures. There are different processing steps to obtain different microstructures in β alloys. The important processing parameters to be controlled in all the cases are recrystallization temperatures to control β grain size, annealing temperature, pre-aging temperature along with cooling rate to determine the volume fraction and morphology of α platelets, and the final aging temperatures to stabilize the size and volume fractions of α platelets [65–68].

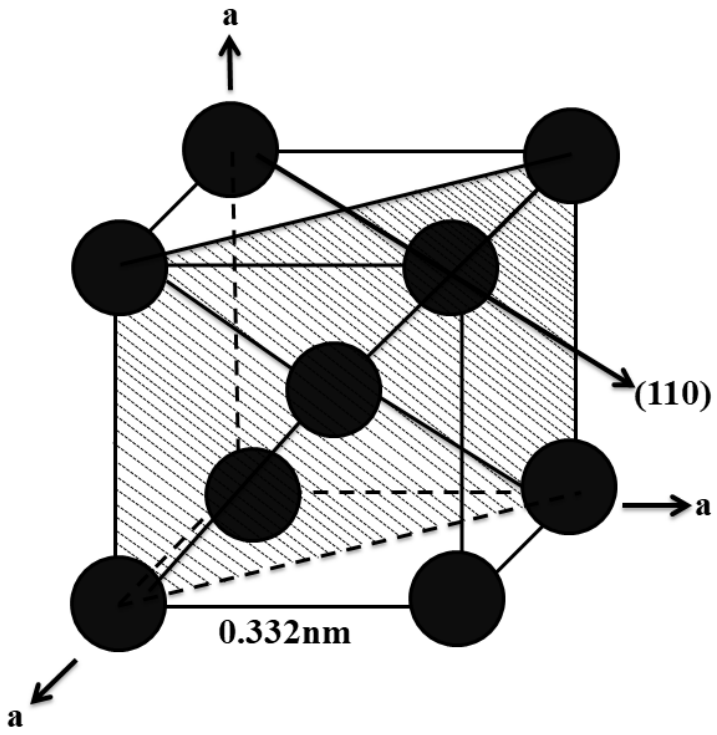

Figure. 1.11. Unit cell and crystal structure of β phase

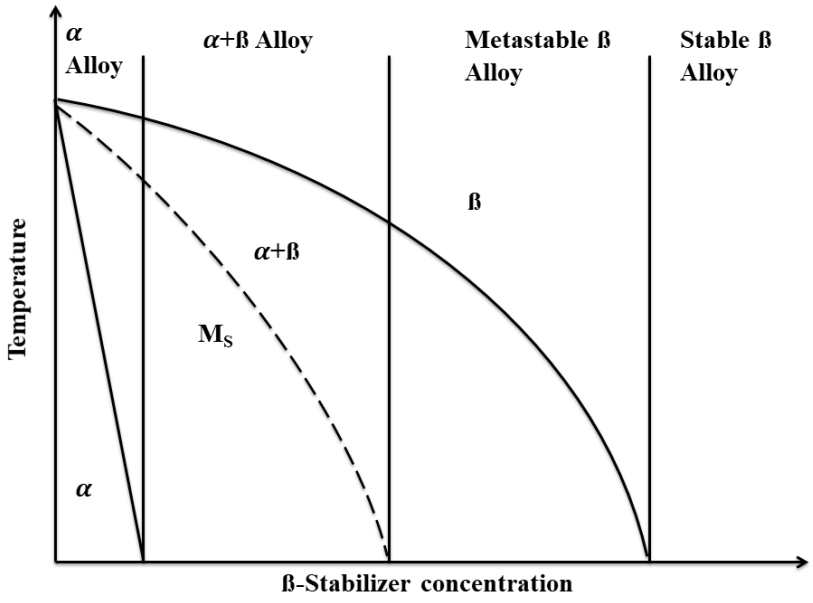

Figure. 1.12. Pseudo-binary section of β isomorphous phase diagram.

Solid solution strengthening of β phase is very hard to analyze compared to that of α phase due to the fact that the effects of metastable ω and β′ phases cannot be distinguished from the solute effects, neither that the effects of α precipitates cannot be separated from solute effects in over-aged β alloys. Although in such a situation, the effects of β stabilizers such as V, Nb, Cr and Fe on the lattice parameter were investigated, which can be derived from analyzing the slope of solute concentrations vs lattice parameters. The slope gives the implication on the misfit parameter qualitatively for binary alloys. Ti-Fe indicates the steepest slope followed by Cr and V while Nb and Mo only have lesser effects on the lattice parameter [69]. One of the major distinguishable changes in mechanical properties is the increase in yield stress by the addition of β stabilizer due to the presence of ω and β′ metastable phases. Apart from the solid solutes, oxygen also affects the β alloys by enhancing twinning deformation. Mo or Zr based β alloys reported to have twinning that contains over 1000 ppm oxygen [70–72]. It is important to note that the presence of oxygen in α phase reduces the probability of twinning.

Ti-V system is the primary concern to understand the effect of vanadium on titanium in this study. Figure 1.13 shows a phase diagram of Ti-V, indicating that vanadium has limited solid solubility in α titanium only up to about 2 at%. According to the studies reported by Hanada *et al* [73–75], the binary titanium alloys such as Ti-V, Ti-Mo, and Ti-Cr result in low yield stress and large elongation due to twinning with {332} <113>. However, the increase in alloying elements leads to the decrease in twinning and increase in <111> slip, which further contributes to higher yield stress.

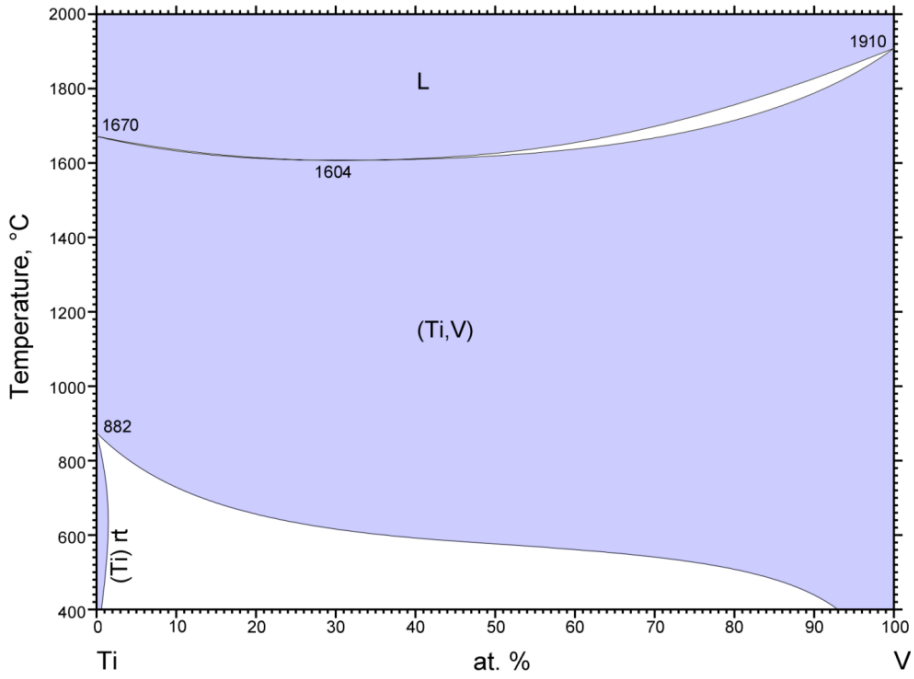

Figure. 1.13. Phase diagram of Ti-V [76].

1.6 Alpha+Beta alloys:

The alloys that contain both α and β phases are termed as α+β alloys. The alloys share the microstructure of both phases, inheriting some properties from both the phases. For example, α and β phases contribute to the strength of the alloy in the mixture-rule average. The contributions of each phase draw interest to study [77–80]. The α+β alloys are the most important class of titanium alloys as they yield the advantages of properties from both the phases. The major disadvantages of α Ti alloys are phase instability at higher temperatures, the lack of mechanical properties such as the combination of strength and ductility, and low resistances against creep resistance and fracture toughness [81–84]. The major disadvantage of β alloys is that they show brittle-to-ductile transition as well as other BCC alloys, which limits the applications at low temperatures [84–88]. The α+β alloys overcome the disadvantages in individual alpha alloys and beta alloys to a great extent, so that they are successfully applied to be used in the wide range of temperatures, *that is* from cryogenic to high temperatures, by obtaining a superior combination of properties [1,5,15].

One of the greatest assets of α+β is obtaining various microstructures by playing with thermo-mechanical processing parameters. The possible microstructures of this class are fully nodular, fully lamellar, duplex, bimodal, and mill-annealed [89–95]. Figure 1.14 shows a schematic of processing to obtain bimodal microstructure which was used in this study. In the first step, a specimen is homogenized in β phase-field as shown step I in Fig. 1.14, then deformed and recrystallized at the temperature of α+β phase as shown in steps II and III, respectively, and then annealed or aged at lower temperatures as shown in step IV.

There are several important parameters to be focused to obtain a perfect bimodal structure as the slight changes in parameters significantly affect the microstructure of titanium. The cooling rate is one of the important parameters in step I which controls the width of α lamellae. The deformation and recrystallization of obtained α lamellae are in step II and step

III, respectively. Deformation temperature, the amount of deformation, and the mode of deformation in step II determine the symmetry/intensity of texture and dislocation density. Annealing temperature and cooling rate in step III control (i) the volume fraction of primary α which located at the triple points of recrystallized β grains, (ii) grain size of β, (iii) element partitioning inside phases accordingly to the respective stabilizing elements, and (iv) width of α lamellae. Finally, the annealing temperature in step IV contributes to the age hardening of Ti_3Al particles due to the partitioning of alloying elements in step III, which causes lower concentrations of aluminum and oxygen in secondary α in a/β lamellae.

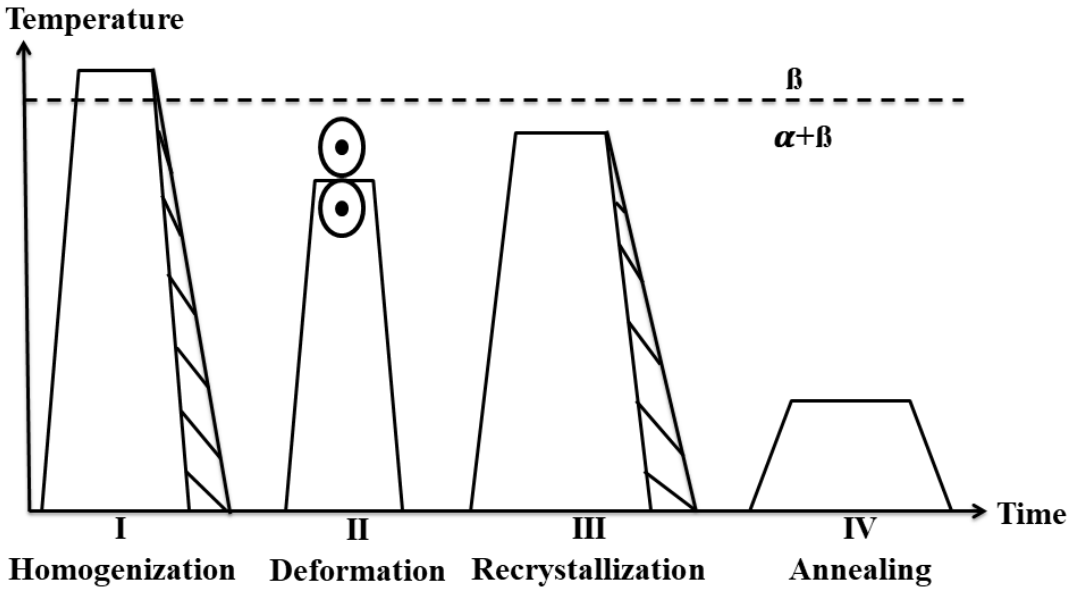

Figure 1.14. Processing route to obtain bimodal microstructure of α+β alloys.

1.7 Ti-6Al-4V: A peculiar commercial alloy

Ti-6Al-4V is a classical alloy of titanium, which has been commercially using over the decades. Much attention has been given to the alloy due to having desirable properties for many crucial applications. Ti-6Al-4V is superior to other α+β alloys in terms of having good weldability and formability along with high room-temperature strength which can be maintained also at higher temperatures [84]. Also, Ti-6Al-4V is widely used compared to any other α+β alloy at both ends of operating temperatures such as low and very low temperatures (cryogenic tanks, superconducting magnet support systems), body temperature (biomedical materials), and high temperatures (jet engines, gas turbines) [15–17,19,23,35]. As similar to the other α+β alloys, Ti-6Al-4V also can be available in different microstructural forms such as bimodal with primary α nodular grains and lamellae colony consists of secondary α and β phases, duplex with primary α along with secondary phases, equiaxed nodular, martensitic, and widmanstätten structures. The processing steps to obtain bimodal structure is as shown in Fig. 1.14. The β transus temperature demonstrates the conditions of thermomechanical processing to obtain the desired microstructure and the β transus temperature is highly sensitive to the concentration of the alloying elements. Phase transformation temperatures α+β→β for Ti-6Al-4V in comparison with other popular β alloys are mentioned in Table 1.2. Figure 1.15 (a) shows classical tertiary phase diagrams of Ti-Al-V marked with Ti-6Al-4V composition at various isothermal temperatures and corresponding expectable phases. The broad types of microstructural features obtainable in titanium alloys demonstrating the composition of Ti-6Al-4V are shown in the 3D phase diagram along with the classical phase diagram shown in Fig. 1.15 (b).

Table 1.2. Start and finish temperatures of α+β→β phase transformation in duplex titanium alloys [96].

Phase transformation	**Alloy (phase transformation temperature °C)**		
	Ti-6Al-4V	Ti-6Al-2Mo-2Cr	Ti-6Al-5Mo-5V-1Cr-1Fe
$T^{ns}_{\alpha+\beta\rightarrow\beta}$	890	840	790
$T^{ps}_{\alpha+\beta\rightarrow\beta}$	930	920	830
$T^{f}_{\alpha+\beta\rightarrow\beta}$	985	980	880
$T^{s}_{\beta\rightarrow\alpha+\beta}$	950	940	850
$T^{f}_{\beta\rightarrow\alpha+\beta}$	870	850	810

*where ns represents nucleation starts, ps-precipitation starts, s meant for start and f for finish.

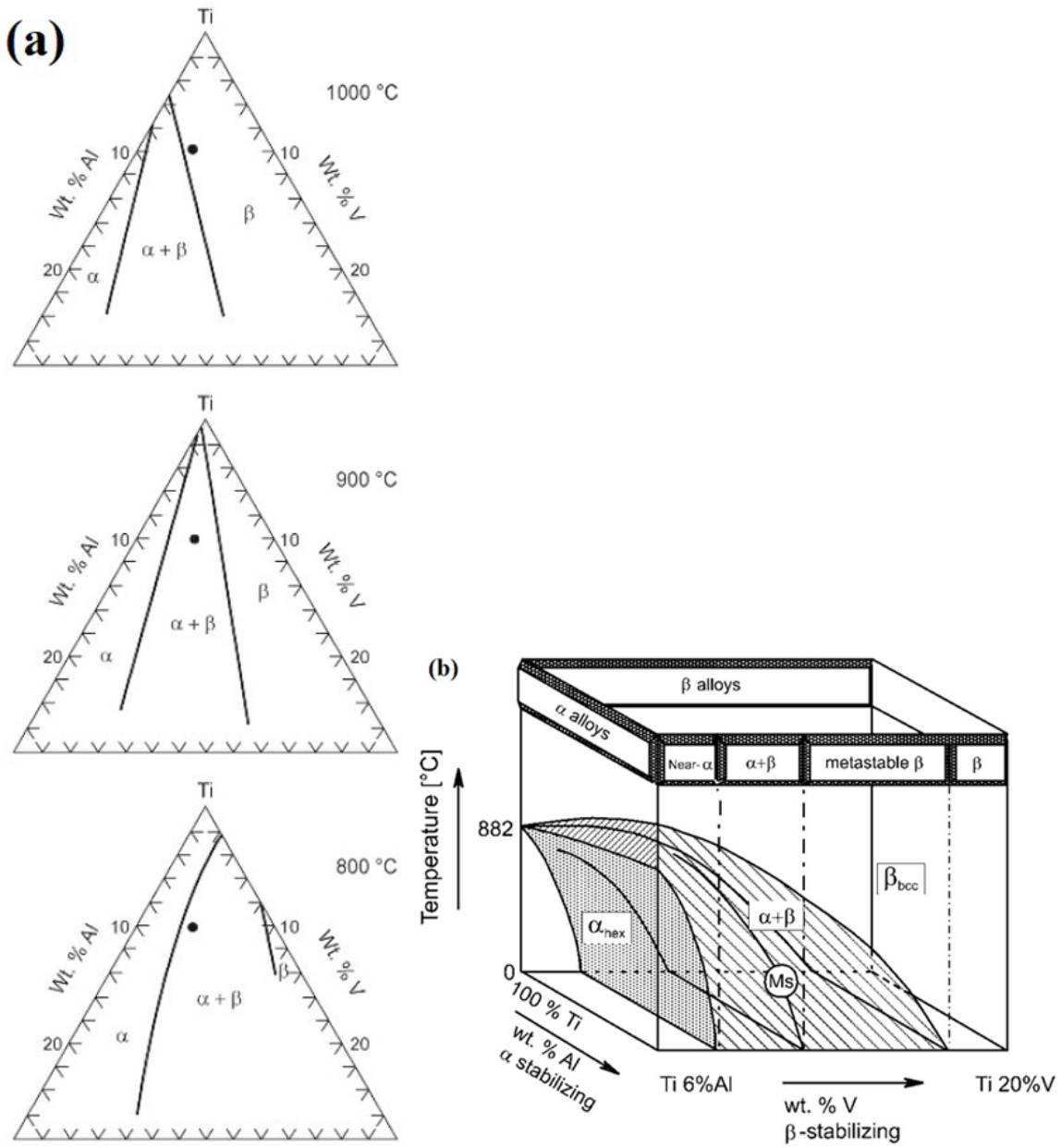

Figure 1.15. Ternary phase diagrams of Ti-Al-V. (a) Isothermal sections at 1000°C, 900°C, and 800°C through the Ti-rich corner of the ternary where Ti-6Al-4V composition with solid points are indicated [97], (b) 3D phase diagram to classify Ti alloys pertaining to Ti-6Al-V [53]

In contrast to the α or β single phase alloy, α+β alloys contain both elements of α and β stabilizers. Each alloying element would have significant and different effects on the properties of the alloy, which makes it much more complex to comprehend the fundamental theories involved in the changing properties. In Ti-6Al-4V, apart from the interstitial oxygen, substitutional aluminum and vanadium are important elements in determining the basic properties of the alloy. The effects of aluminum and vanadium on α phase and β phase are as explained in CP-Ti and Ti-V, respectively. In Ti-6Al-4V, the estimations from the effect of alloying elements which were studied in CP-Ti and Ti-V might be valid or not as the Al and V in Ti-6Al-4V might have the different effects from those do individually in other mentioned binary alloys. The cumulative effects of both α and β stabilizers on Ti-6Al-4V were not yet well augmented. However, the performance and basic nature of the phases can be correlated to the properties of individual α and β phases. Also, there is no apparent evidence on the distribution of each alloying element among both phases [79]. Therefore, it can be considered that Al and V change the mechanical properties of α and β phases, respectively.

Al and V contribute to the solid solution strengthening of their respective stabilizing phases. One percent Al contributes to the UTS of titanium by 50 MPa while V by 35 MPa. 6 mass% of Al and 4 mass% of V for Ti-6Al-4V are the best composition to avoid the formation of intermetallic brittle phases to obtain the best combination of strength and ductility. The fact that Al is a rapid hardener while V is a lesser hardener suggests that Al and V in Ti-6Al-4V should work as the average effect of hardening by the rule of mixing. Similarly, Al increases the elastic modulus whereas the existence of vanadium known to lower the elastic modulus. Although vanadium might not contribute to the strength to a great extent, transition metals in titanium affect the lattice stability as explained in section 1.5. The detailed change in mechanical properties with respect to the alloying elements would be discussed in the later section.

Apart from solid solution strengthening, the constitution of bimodal microstructure itself plays an important role in strengthening by having α and β interfaces, which can act as obstacles to dislocation movement in addition to grain boundaries. The crystallographic orientation relationship *i.e.* Burgers relationship between α and β has been first investigated in zirconium as $(110)_\beta \parallel (0002)_\alpha$ slip planes and the slip direction of $[1\bar{1}1]_\beta \parallel [11\bar{2}0]_\alpha$ [98]. Later the Burgers relationship was validated experimentally in titanium [99]. During phase transformations, bcc crystal can transform to 12 variants of hcp crystal according to the Burgers relationship which is valid in case of martensitic transformation as well as conventional nucleation and growth process.

1.8. Mechanical behavior of Titanium and its alloys

1.8.1. Temperature dependence of tensile deformation in CP-Ti

The change in mechanical properties with respect to the alloying elements and temperature under monotonic uniform loads will be reviewed in this section. Since the strengthening due to microstructure is not significant in CP-Ti as that in α+β alloys, the effect of temperature on CP-Ti will be discussed by taking effect of alloying elements into account, the effects of interstitial impurities especially oxygen at first followed by the effects of substitutional elements of aluminum and vanadium.

All grades of CP-Ti exhibit good ductility even at lower temperatures. Elongation to fracture increases as the temperature decreases, in fact, they exhibit 40% ~ 50% elongation to fracture at 77 K. It is considered to be the onset of twinning during the deformation. Twinning is also a more prominent mode of plastic deformation in CP-Ti. $\{10\bar{1}2\}$ and $\{11\bar{2}2\}$ can be twinning planes depending on the stress direction with respect to the crystallographic axes and

temperature [41,100,101]. Cold rolling of CP-Ti increases strength off-trading ductility. Interstitials, particularly oxygen, also affect the strength of CP-Ti which was the primary focus by Conrad and coworkers [49,102–104]. One of the key points to understand mechanical properties is slip modes. As shown in Fig.1.8, the major slip planes in CP-Ti are $\{10\bar{1}0\}$, $\{10\bar{1}1\}$ and (0001) with $\vec{a}$ Burgers vector and the possible slip systems in CP-Ti. As the interstitial content or temperature increases, $\{10\bar{1}1\}$ and (0001) are more preferable than $\{10\bar{1}0\}$ [45]. TEM analysis [101,105,106] and slip trace analysis [101,105] evidenced the activation of slips with a Burgers vector out of the basal plane. Cass [106] studied the dislocation structure in deformed single crystals of titanium, indicating that the prismatic slip has been demonstrated by long lengths of dislocation lines which are very proximate to the orientation of screw dislocations. The dislocations in basal slips also exhibit screw components without dissolving in the deformed specimen.

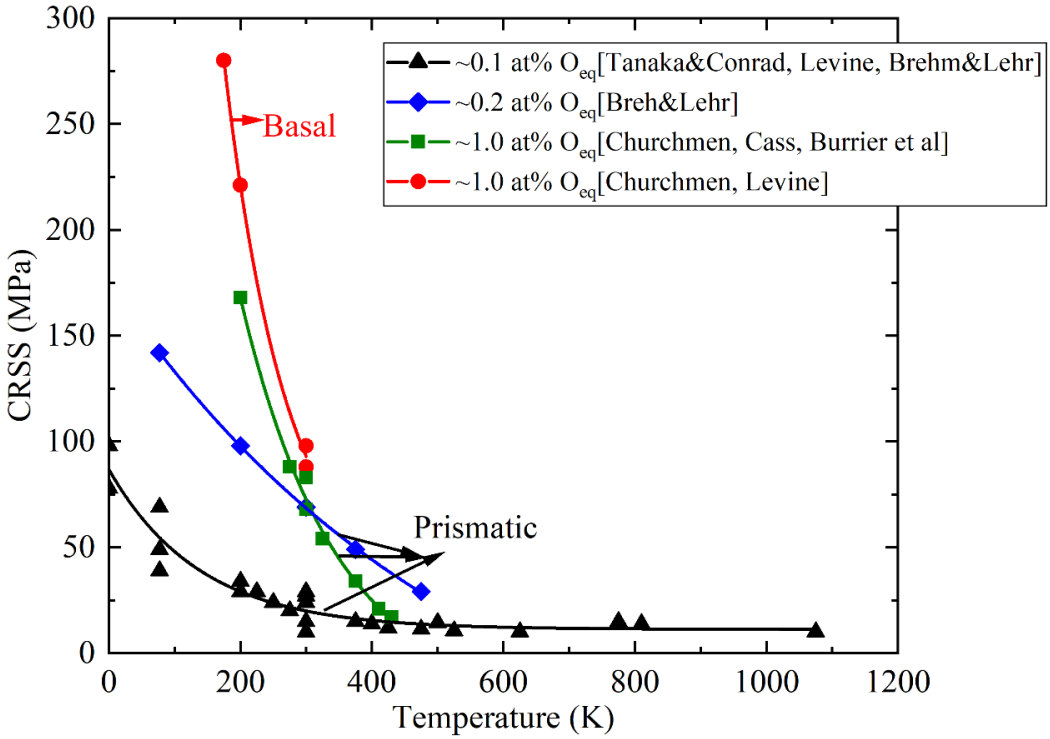

Figure. 1.16. Effects of interstitial content and temperature on CRSS of prismatic [46,101,105,107–111] and basal slips [46,108] in CP-Ti.

The mechanical properties of CP-Ti changes with the change in the concentration of interstitial elements such as oxygen and carbon. Figure 1.16 shows the effect of interstitials content and temperature on CRSS of CP-Ti in different slip planes although the effect of interstitials on the CRSS of basal slips has not been studied much. Here, the oxygen equivalent, O_{eq}, is considered as the cumulative of oxygen, carbon, and nitrogen as C = ¾ O and N = 2O. There exists a strong effect of oxygen on CRSS of prismatic slip in CP-Ti. CRSS increases as intestinal concentration increases. The results from 1.0 at% O_{eq} exhibit the values of CRSS for prismatic and basal are close at high temperatures, suggesting the activation of both prismatic and basal slips in the specimens with O_{eq} = 1.0 at% as the temperature increases. Extrapolating the results of prismatic and basal slips from 1.0 at% O_{eq} in Fig.1.16, the values of CRSS of prismatic and basal slips should be closer at high temperatures. It suggests the possibility of the activation of basal slip at high temperatures in polycrystalline CP-Ti.

The effects of interstitial content and temperature on 0.2% proof stress were also investigated. Figure 1.17 shows the relationship between temperature and 0.2% proof stress along with the effect of interstitials. CP-Ti exhibits strong temperature dependence of yield stress as CRSS decreases with increasing temperature as shown in Fig.1.16. The effect of interstitials on the proof stress is stronger at low temperatures, however, it becomes weak at higher temperatures.

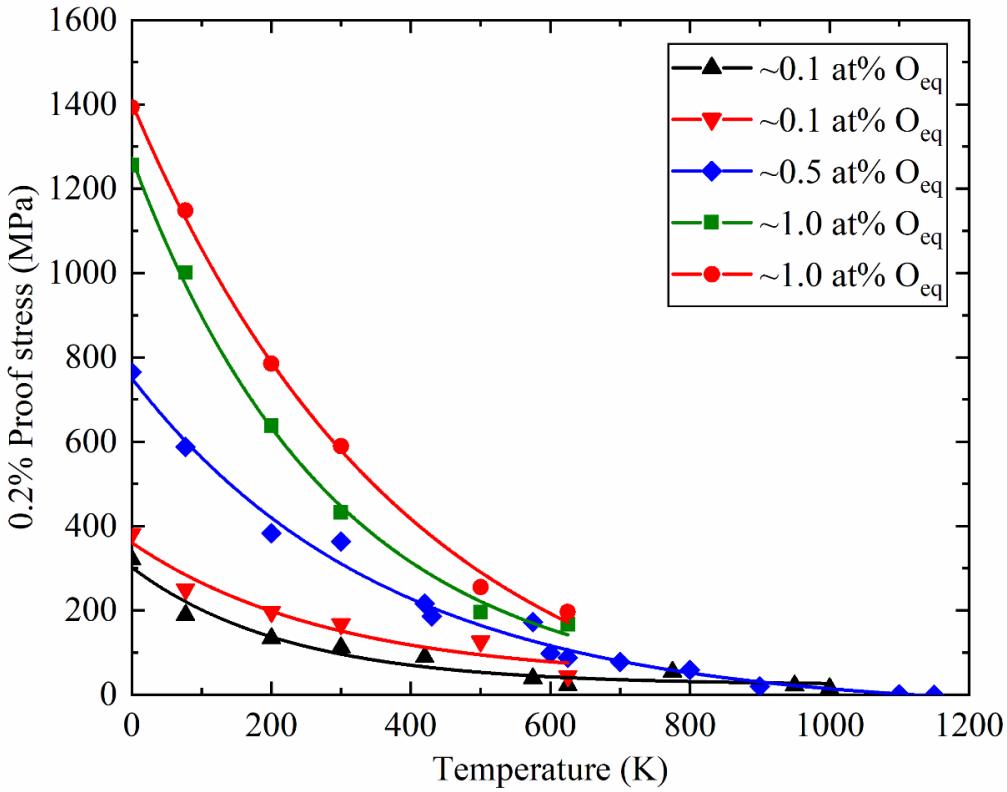

Figure. 1.17. The effect of interstitial content and temperature on the 0.2% proof stress [111–114].

1.8.2. Temperature dependence of tensile deformation in Ti-6Al

The next set of mechanical properties is in aluminum added titanium *i.e.* Ti-6Al which is the basis to understand the mechanical properties of Ti-6Al-4V. The principal effect of aluminum is changing the slip systems compared to CP-Ti. The ductility of CP-Ti can be explained by the complex twinning and first-order prismatic slip as the principal deformation mechanism. On the contrary, the suppression of twinning and the possibility for activation of basal slip increases with aluminum content can be explained by the CRSS profiles. Figures 1.19 (a) and (b) show the effect of both aluminum concentration and temperature on the CRSS of basal and prismatic slips, respectively. Figures 1.19 (a) shows, at lower aluminum concentrations, CRSS exhibited fluctuations several times with respect to temperature, which can be explained by the onset of twinning deformation. The onset of deformation twinning is suppressed with the increase in temperature compared to CP-Ti [56]. At sufficient aluminum concentration *i.e.* Ti-6.6 mass% Al, twinning was suppressed as the CRSS of basal slip becomes lower than that of twinning with increasing temperature. On the other hand, CRSS of prismatic slip merely increased with increasing aluminum concentration and decreases with increasing temperatures as shown in Fig. 1.19 (b) [41,57,106].

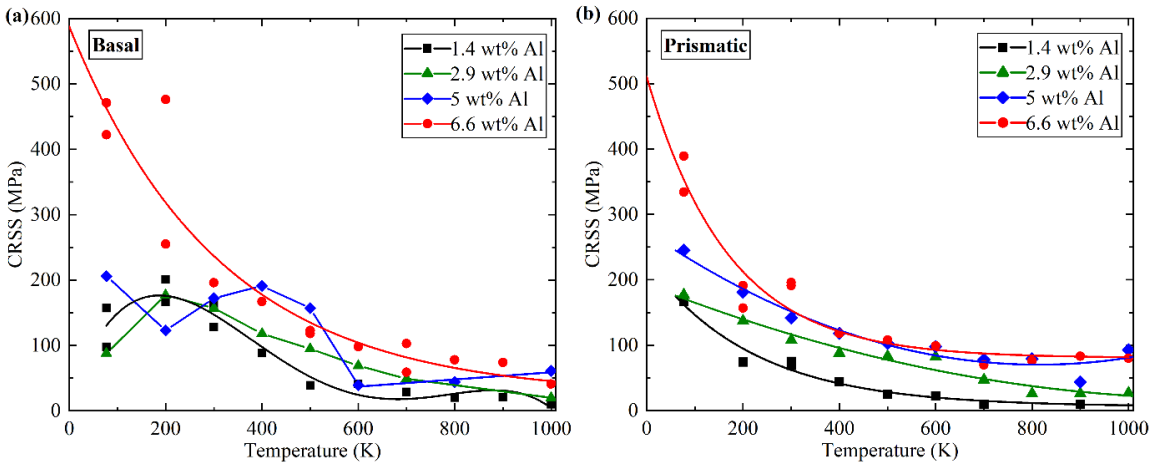

Figure. 1.19. Temperature dependence of CRSS with respect to the aluminum concentration in titanium [56]. (a) CRSS of basal slip, (b) CRSS of prismatic slip.

1.8.3. Effect of alloying addition on the elastic modulus

The other significant effect of Al and V is on the elastic modulus of titanium. Figure 1.20 (a) shows the effect of Al concentration on the elastic modulus of titanium. Elastic modulus increases continuously with increasing Al content. The increase in the elastic modulus over 10 mass% Al is due to the intermetallic phase of Ti_3Al. The phase diagram of Ti-Al as shown in Fig. 1.9 indicates the existence of $\alpha + Ti_3Al$ in between 11 to 23 at% Al. Figure 1.9 (b) shows that vanadium decreases the elastic modulus of titanium up to 10 mass% that corresponded to the α+β region in the phase diagram with respect to β stabilizers as shown in Fig. 1.15 (b). The rapid increase in elastic modulus at 10 mass% V is presumed to be associated with the metastable β phase and ω phase. β phase is stabilized as the concentration of β stabilizer increases, which explains the decrease in elastic modulus from the highest point. The consistent increase after that in elastic modulus can be explained by the solid-solution and precipitations [115].

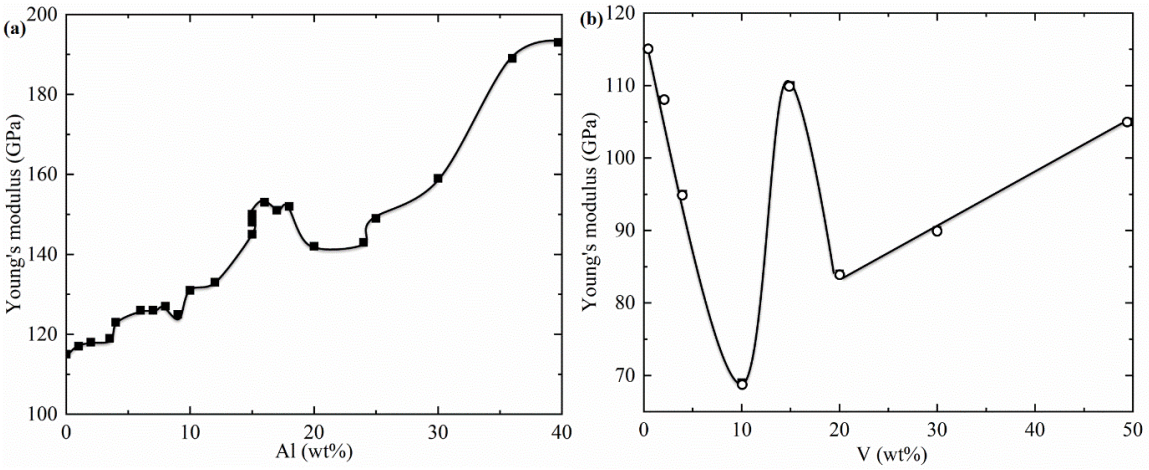

Figure. 1.20. Effect of alloying elements on the elastic modulus of titanium. (a) effect of aluminum [115], (b) effect of vanadium [116].

1.9. Fatigue properties

1.9.1. Overview

The wide usage of titanium alloys in the applications which often exposed to cyclic loads such as in aerospace, gas turbines, etc., demands the study of fatigue properties in titanium. The lifetime of a component can be estimated through fatigue properties as it is the most eminent criteria to safeguard humankind especially in aero and structural components. The damage tolerance tests at laboratory experiments are performed with notched specimens because all the materials are not defect-free like an ideal one. It is very important to consider the factor of temperature due to the applications involved at higher temperatures and often operates cyclically between room temperature and high temperatures. The structural components must bear all the atmospheric conditions. There are several parameters that influence the fatigue crack propagation rate such as chemical composition, microstructure, load ratio, load amplitudes, load frequency, mean stress, atmosphere, and temperature. There are a lot of results on the fatigue tests in terms of changing mechanical variables in Ti alloys. However, it is the fundamental theories behind fatigue that are not fully understood especially on the temperature dependence of fatigue crack growth.

Microstructure plays an important role in correlating fatigue properties in titanium alloys. Fine equiaxed microstructures have higher fatigue strength compared to coarsened microstructure as the result of higher resistance to crack initiation. The fatigue crack growth rate (da/dN) also greatly influenced by the microstructure; the specimen with a fully-lamellar structure exhibits a slower crack growth rate compared to that with an equiaxed structure in Ti-6Al-4V under the constant load amplitudes and R ratio [117–119]. Other microstructural parameters affect da/dN, such as grain size, phase morphology, crystallographic texture, processing parameters such as age hardening condition, degree of work hardening, and elastic constants [120,121]. Phenomenologically, fatigue crack propagation divided into two

components. One is the early stage of the fatigue life, *i.e.*, at the time of crack initiation or microcrack growth. The other is the late stage of fatigue life, *i.e.*, at the time of macrocrack growth. In general, these two components have a contradictory effect by microstructural parameters. The resistance to microcrack propagation should be considered in case of a short lifetime at high-stress level while macrocrack propagation should be conserved in case of long lifetime at lower stress levels [121–123].

1.9.2. CP titanium

Titanium alloys usually take short time for crack initiation in a notched specimen compared to overall fatigue lifetime of N_I/N_F=0.01 where N_I is the number of cycles for crack initiation and N_f is the number of cycles to failure. Thus, resistance to crack propagation largely contributes to the lifetime under high cycle fatigue (HCF) and vice-versa under low cycle fatigue (LCF) in the notched specimens [118,119]. Typical defect-free titanium alloys under HCF should withstand a very large number of cycles which can implicate to the high resistance to crack initiation. The fatigue resistance of CP-Ti is influenced by grain size, oxygen content and degree of work hardening. The fatigue strength of CP-Ti with respect to these parameters under HCF has been investigated by Turner and Roberts [124]. Figure 1.21 (a) shows the effect of grain size on fatigue strength, exhibiting the fatigue strength that has an inverse relationship with grain size as similar to that of strength under uniform loads. Reduction in grain size from 110 microns to 6 microns extends the fatigue strength from 160 MPa to 210 MPa as shown in Fig. 1.21. (a). Figure 1.21 (b) and (d) show that fatigue strength increases with the oxygen equivalent and work-hardening, respectively. Figure 1.21 (d) shows da/dN curves from two different grain sizes with two different oxygen concentrations in CP-Ti, indicating the smaller grain size, the lager da/dN along with the effect of oxygen concentration. As the oxygen concentration increases, the effect of grain size becomes more significant on the crack propagation rate [124,125].

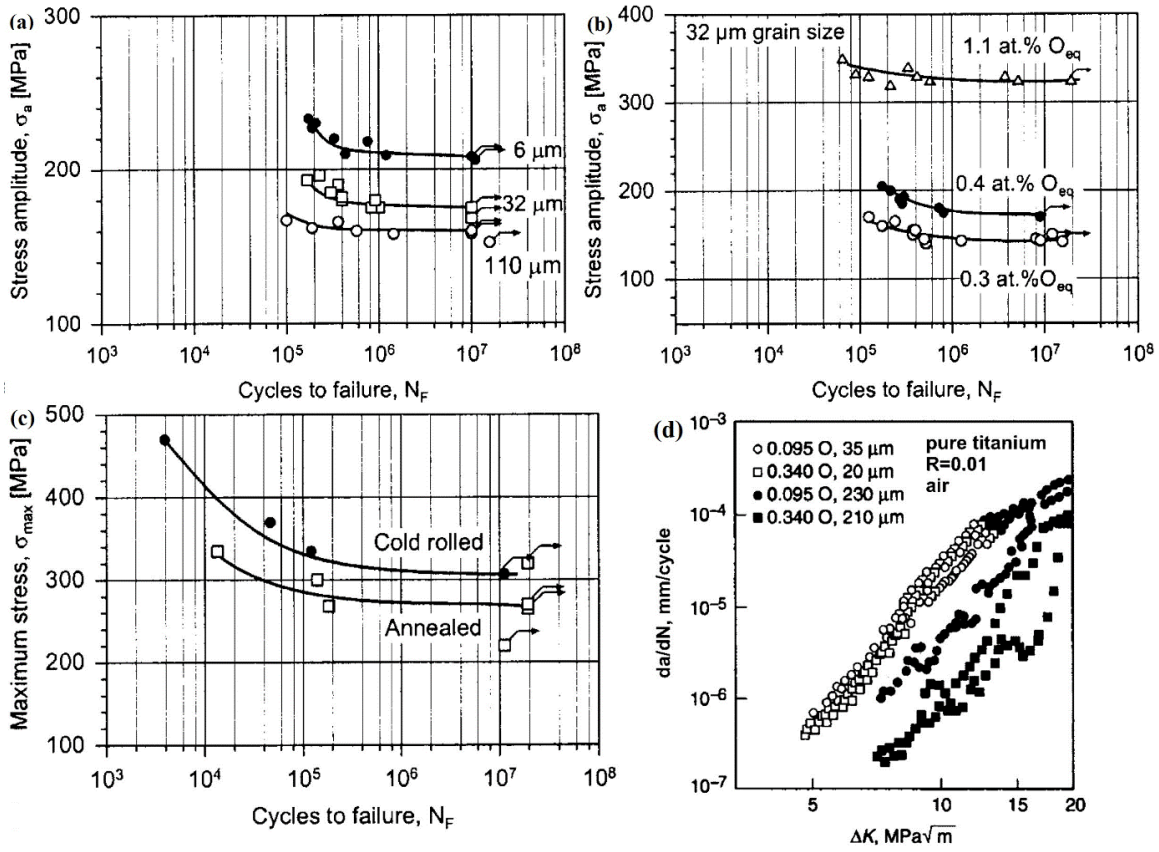

Figure. 1.21. Effect of several parameters on CP-Ti under HCF. (a) Effect of grain size (R= -1) [124], (b) Effect of oxygen concentration (R= -1) [124], (c) effect of work hardening (R=0.1) [125]. (d) Effect of oxygen concentration and grain size on FCG rates of CP-Ti at R=0.01 [125].

1.9.3. Ti-Al binary alloys

In Ti-Al alloys, precipitations also influence the fatigue behavior of Ti-Al alloys in addition to the parameters that influence on the fatigue resistance of CP-Ti. The microstructure in Ti-Al changes with aging. Gysler et al [126] studied the effect of the evolution of coherent Ti_3Al particles on the fatigue behavior of Ti-8.6Al. Figure 1.22 (a) indicates that the fatigue strength is increased by aging. Wanger et al [122] observed planar slips play a significant role in aluminum added titanium *i.e.* Ti-8.6Al as the nucleation of fatigue cracks initiated along the planar slip bands. They also observed that microcracks propagate faster in the specimen with coarse grains than that with fine-grained under the constant stress intensity range, ΔK, as the frequency of encountering grain boundaries as obstacle decreases with the increase in grain size as shown in Fig.1.22 (b).

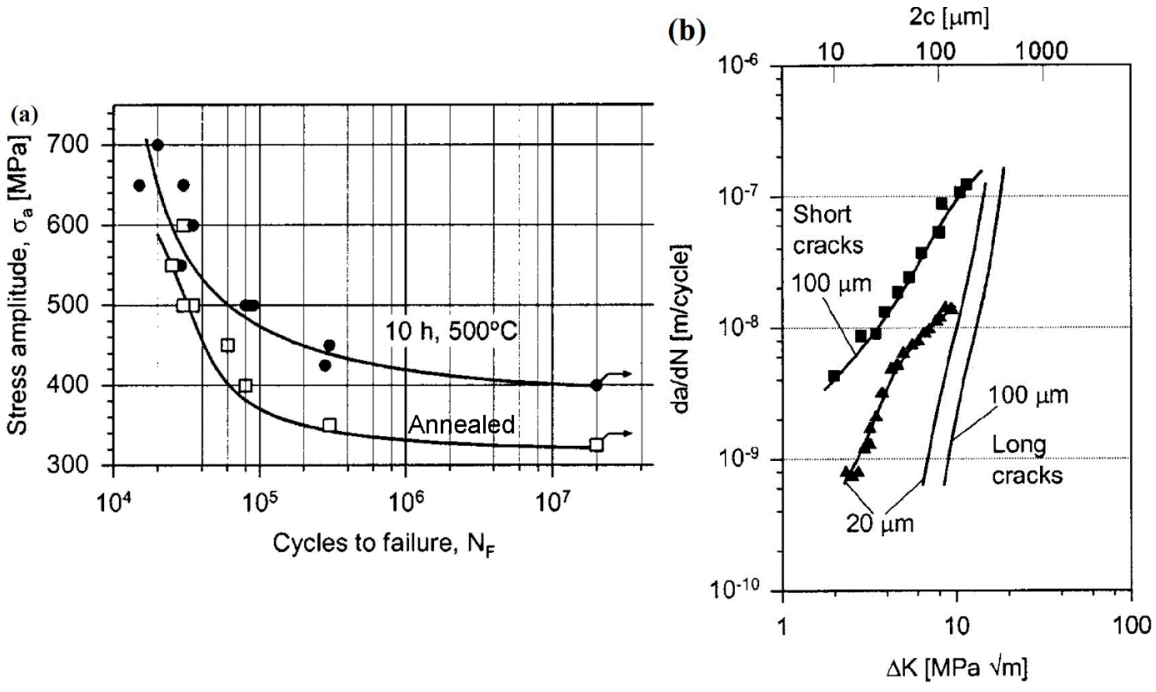

Figure. 1.22. Fatigue behavior of Ti-8.6Al. (a) Stress – Number of cycles to failure (S-N) curves from Ti-8.6Al, where one specimen was aged at 500 °C for 10 hours. The test was performed with R= -1 [122], (b) Crack growth rates of micro (short) and macro (long) cracks [127].

1.9.4. Ti-6Al-4V

As Ti-6Al-4V can have different types of microstructure, they exhibit different fatigue behaviors with different microstructural parameters. There are many important parameters which affect the fatigue behavior such as the grain size of primary α, β grain size, the volume fraction of primary α, the packet size of α+β lamellae, α lamellar size, β lamellar size. Several researches contributed to find out the effect of these parameters in Ti-6Al-4V [128–134]. Their experimental results were replicated here. Figure 1.23 (a) shows the increase in fatigue strength from 480 MPa to 675 MPa in the fully lamellar microstructure of Ti-6Al-4V under HCF due to the reduction of α lamellae width from 10 microns to 0.5 microns [130]. A similar effect can be observed in equiaxed microstructures of Ti-6Al-4V as the fatigue strength increases from 560 MPa to 720 MPa with the decrease in grain size from 12 microns to 2 microns as shown in Fig. 1.23. (b) [130,131]. In duplex structures of Ti-6Al-4V, Fig. 1.23 (c) shows that the fatigue strength increased up to 95 MPa with the reduction in the width of α lamellae in the lamellar matrix from 1 micron to 0.5 microns [131]. Wanger et al [132] studied the difference of microcrack and macrocrack propagations in coarse lamellae and equiaxed microstructures of Ti-6Al-4V. It indicates that macrocracks propagated with lower crack growth rates due to the resistance caused by microstructural geometry and crack closure effects whereas the microstructure. However, the magnitude of the decrease in da/dN from microcrack to that in macrocrack is different between coarse lamellae and equiaxed microstructures.

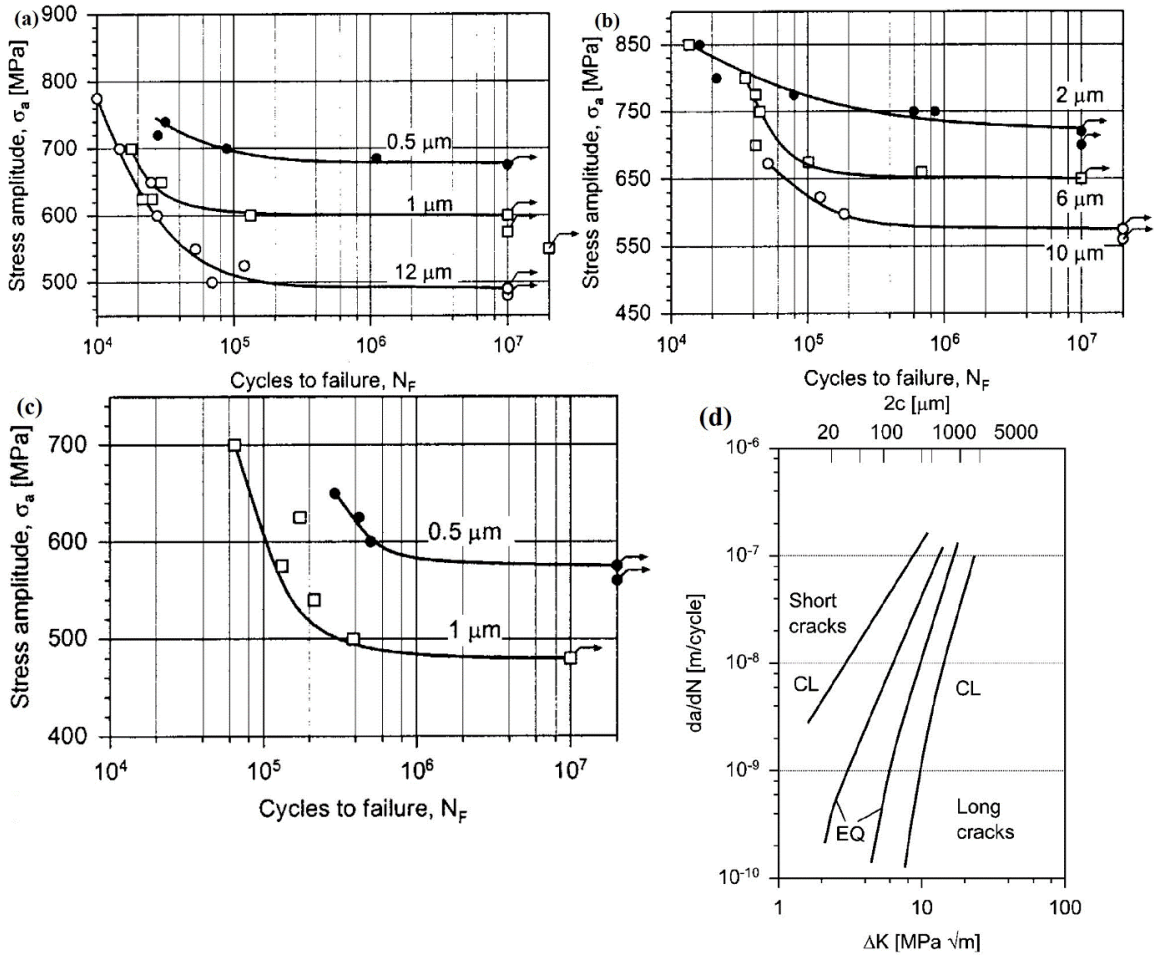

Figure 1.23. Fatigue behavior of Ti-6Al-4V containing different microstructural effects under HCF (R= -1). (a) Effect of lamellae width in lamellar microstructure [130], (b) effect of α grain size in equiaxed microstructure [130], (c) effect of lamellae width in duplex microstructure [131], (d) influence of micro and macro cracks on fatigue crack growth in Ti-6Al-4V with coarse lamellar (CL) microstructure and equiaxed (EQ) microstructure [132].

Yoder et al [135,136] investigated the effect of grain size, the oxygen concentration in both the equiaxed and duplex microstructures in Ti-6Al-4V. The effects of grain size and oxygen concentration are similar to those in CP-Ti and Ti-8.6Al, however lamellar width should be considered in two phase alloys such as Ti-6Al-4V which contains lamellae. The crack growth rate is faster in the case of smaller grain size in Ti-6Al-4V as shown in Fig. 1.24. (a). However, the effect is not as significant as those seen in CP-Ti and Ti-Al. The effect of oxygen cannot be distinguishable as shown in Fig. 1.24. (b) as the effect of microstructural parameters on da/dN is much stronger in the fatigue crack propagation rate. Actually, the effect of oxygen is also not noticeable in CP-Ti, Ti-Al [135–138]. The number of studies of Ti-6Al-4V is limited in terms of the phenomenological relations between microstructural parameters, processing parameters, and mechanical variables in equiaxed and duplex microstructures comparing to those of CP-Ti and Ti-Al. The bimodal microstructure is much more complex than these microstructures as there is a necessity to consider the effect of microstructure and deformation mechanisms of both the phases. The literature gap is higher in the field of the temperature dependence of fatigue crack growth especially pertaining to bimodal microstructures. Even there was no literature works on the change in mechanical variables available, the fundamental theories that connecting to the temperature dependence, microstructure and slip modes are still ambiguous in bimodal Ti-6Al-4V.

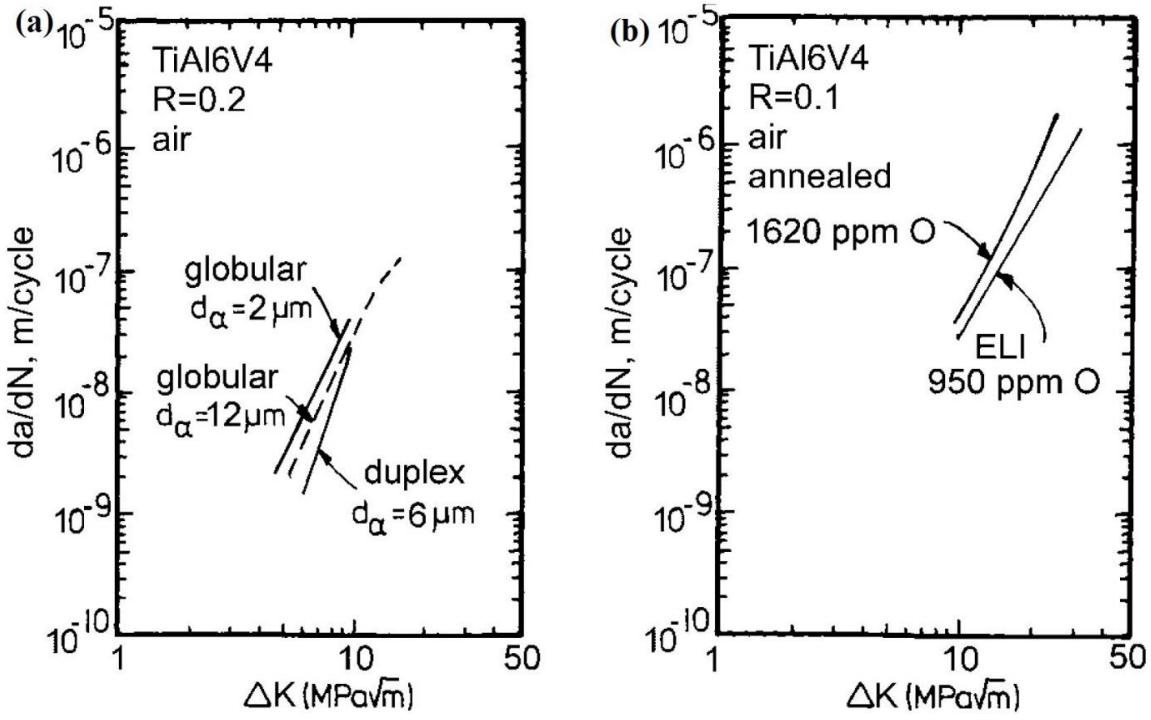

Figure. 1.24. Fatigue crack propagation rate in Ti-6Al-4V. (a) Effect of grain size in equiaxed and duplex microstructures [137], (b) Effect of oxygen in annealed condition [138].

1.10. Objective of the thesis

The temperature dependence of deformation modes and the associated effects of alloying elements, microstructural parameters, processing parameters in single phase titanium alloys such as CP-Ti and Ti-Al have been well established and understood as reviewed in this chapter. Several researchers contributed to the mechanical properties of widely used commercial Ti-6Al-4V, however, the mechanisms behind the temperature dependence of mechanical properties are still ambiguous, which should be understood in terms of thermally activated processes. Also, there were several works provided on fatigue properties of Ti-6Al-4V except focusing on the temperature dependence of fatigue crack propagation in bimodal Ti-6Al-4V. Hence, the current thesis intended to contribute to understanding the temperature dependence concerning the thermally activated process in bimodal Ti-6Al-4V to the possible extent.

In Chapter 1, the overview of titanium alloys and their mechanical properties were presented.

In Chapter 2, the aim is to obtain the fundamental mechanical properties of uniform deformation such as yield stress, effective stress, activation volume, and activation energy, and to observe the change in thermally activated processes with the help of temperature dependence of effective stress.

In Chapter 3, the aim is to investigate the slip activities at different temperatures with the help of trace analysis, Schmid factor distributions, and Taylor factor analysis. An effort was made to elucidate the phenomenon behind the change in the trend of effective stress with respect to temperature, which was elucidated in Chapter 2.

In Chapter 4, the aim is to establish the relationship between fatigue crack propagation rate and temperature under cyclic deformation and to find out the effect of stress ratio on the temperature dependence of fatigue crack propagation rate.

In Chapter 5, the conclusion of this thesis has been presented.

References

[1] R. Boyer, G. Welsch, E.. Collings, Materials Properties Handbook: Titanium Alloys, ASM International, Ohio, 1994.

[2] R.. Jaffee, N.. Promisel, eds., The Science, Technology and Application of Titanium, in: Proc. First Int. Conf. Titan., Pergamon Press, London, 1970.

[3] C. Leyens, M. Peters, eds., Titanium and Titanium Alloys: Fundamentals and Applications, Wiley-VCH, Weinheim, Germany, 2003.

[4] V.. Moiseyev, Ttainum Alloys Russian Aircraft and Aerospace Applications, Volume 5, Taylor & Francis, Boca Raton, 2006.

[5] G. Lutjering, J.C. Williams, Titanium, Second, Springer, Berlin, 2007.

[6] H.. Bomberger, F.. Froes, P.. Morton, Titanium- A historical perspective, in: Titan. Technol. Status Futur. Trends, Titanium Development Association, USA, 1985.

[7] T.. Lippert, Titanium in USA, in: R.. Jaffee, N.. Promisel (Eds.), Sci. Technol. Appl. Titan., Pergamon Press, Oxford, 1970: pp. 5–9.

[8] P. Hodgkinson, Titanium in Europe, in: R.. Jaffee, N.. Promisel (Eds.), Sci. Technol. Appl. Titan., Pergamon Press, Oxford, 1970: pp. 11–17.

[9] S.. Seagle, The state of the USA Titanium Industry, Mater. Sci. Eng. A. A213 (1996) 1–6.

[10] U. Zwicker, Titan and Titanlegierungen, Volume 21, Springer-Verlag, Heidelberg, 1974.

[11] R.. Wood, Titanium Alloys Handbook, Publicatio, Metals and Ceramics Information Center, Battelle, 1972.

[12] E.. Krebs, The History and Use of Our Earth's Chemical Elements: A Reference Guide, Second, Greenwood Press, Westport, 2006.

[13] R. Boyer, An overview on the use of titanium in the aerospace industry, Mater. Sci. Eng. A. A213 (1996) 103–114.

[14] M.J. Donachie, Titanium: A Technical Guide, ASM International, Ohio, 1988.

[15] I. Inagaki, Y. Shirai, T. Takeuchi, N. Ariyasu, Application and Features of Titanium for the Aerospace Industry, 2014.

[16] J.. Nicholls, M.. Deakin, T. Rose, Surface Engineering of Titanium Alloys for High Temperature Applications, in: M.. Winstone (Ed.), Titan. Alloy. Elev. Temp. Struct. Dev. Serv. Behav., The University Press, Cambridge, London, 2001: pp. 187–218.

[17] C.. Hanson, Some technical considerations on the use of titanium consider tubing in public utility power generation turbines, in: R.. Jaffee, H.. Burte (Eds.), Titan. Sci. Technol., The Metallurgical Society of AIME, Newyork, 1972: pp. 145–156.

[18] W.. Brindley, Oxidation resistant coatings for Ti3Al+Nb and SiC/ Ti3Al+Nb, in: HITEMP Rev. 11 Compressor/Turbine Mater. (Metal/Intermetallic Matrix Compos., Ohio, 1992: pp. 41.1-41.15.

[19] C.. Jones, Surface and Substrate stability of Titanium Alloys used in Aerospace

Applications, in: M.. Winstone (Ed.), Titan. Alloy. Elev. Temp. Struct. Dev. Serv. Behav., The University Press, Cambridge, London, 2001: pp. 219–235.

[20] A.G.. Morton, I.. Lane, Titanium castings for Marine propellers, in: R.. Jaffee, H.. Burte (Eds.), Titan. Sci. Technol., Volume 1, The Metallurgical Society of AIME, Newyork, 1972: pp. 119–130.

[21] L.. Sanders, R.. Baxter, R.. Juergens, Titanium! The bridge to composites, in: R.. Jaffee, H.. Burte (Eds.), Titan. Sci. Technol., Volume 1, Metallurgical Society of AIME, Newyork, 1972: pp. 105–117.

[22] W.. Williams, Marine applications of Titanium, in: J. R.I, N. Promisel (Eds.), Sci. Technol. Appl. Titan., Pergamon Press, Newyork, 1970.

[23] W. Wang, C.. Poh, Titanium alloys in orthopaedics, in: J. Sieniawski, W. Ziaja (Eds.), Titan. Alloy. Prop. Control, InTech, Croatia, 2013: pp. 1–19.

[24] J.. Sobiecki, T. Wierzchon, T. Karpinski, J. Rudnicki, Modification of the Microstructure and Properties of Ti-1AI-1Mn Titanium Alloy due to Nitriding and Oxynitriding under Glow Discharge Conditions, in: M.. Winstone (Ed.), Titan. Alloy. Elev. Temp. Struct. Dev. Serv. Behav., The University Press, Cambridge, London, 2001: pp. 229–235.

[25] A.. Fraker, A.. Ruff, P. Sung, A.. Van Orden, Surface Preparation and Corrosion Behaviour of Titanium Alloys for Surgical Implants, in: Titanium'80 Sci. Technol., Plenum Press, Newyork, 1980: p. 2447.

[26] P.. Higham, Ion Implantation as a Tool for Improving the Properties of Orthopedic Alloys, in: Proc. Conf. Biomed. Mater., Materials Research Society, Boston, 1986: p. 253.

[27] H.. Rack, J.. Qazi, Titanium alloys for biomedical applications, Mater. Sci. Eng. C. 26 (2006) 1269–1277.

[28] J. Emsley, Titanium, in: Nature's Build. Blocks An A-Z Guid. to Elem., Oxford University Press, England, 2001.

[29] K. Rudinger, The role of Titanium in anodizing and electroplating, in: R.. Jaffee, H.. Burte (Eds.), Titan. Sci. Technol., The Metallurgical Society of AIME, Newyork, 1972: pp. 165–184.

[30] A. Raveh, A. Bussiba, A. Bettelheim, Plasma nitrided α+β Ti alloy: layer characterization and mechanical properties modification, Surf. Coatings Technol. 57 (1993) 19–29.

[31] A. Wypych, P. Siwak, D. Andrzejewski, J. Jakubowicz, Titanium Plasma-Sprayed Coatings on Polymers for Hard Tissue Applications, Mater. 11 (2018) 1–7.

[32] T. Tetsui, Application of TiAl in a Turbocharger for Passenger Vehicles, Adv. Eng. Mater. 3 (2001) 307–310.

[33] D.. Lide, ed., CRC Handboook of Chemistry and Physics, 86th ed., CRC Press, Boca Raton, 2005.

[34] O. Schauerte, Titanium in Automotive production, in: C. Leyens, M. Peters (Eds.), Titan. Titan. Alloy. Fundam. Appl., Wiley-VCH, Germany, 2003: pp. 467–482.

[35] C. Leyens, M. Peters, Non-Aerospace Applications of Titanium and Titanium Alloys, in: C. Leyens, M. Peters (Eds.), Titan. Titan. Alloy. Fundam. Appl., Wiley-VCH, Germany, 2003: pp. 393–422.

[36] R.. Davis, Metals Handbook, ASM International, Ohio, 1998.

[37] F.. Froes, Developments in Titanium Applications, 1995.

[38] F.. Froes, P.. Allen, M. Niinomi, Non-Aerospace applications of Titanium, TMS, Warrendale, USA, 1998.

[39] M. Gruntman, Blazing the Trail: The Early History of Spacecraft and Rocketry, American Institute of Aeronautics and Astronautics, Reston, 2004.

[40] J.. Hall, D. Banerjee, T. Wardlaw, Titanium, Science and Technology, DGM, Oberursel, Germany, 1985.

[41] P.. Partridge, The crystallography and deformation modes of hexagonal close-packed metals, Metall. Rev. 12 (1967) 169–194.

[42] N.E. Paton, J.C. Williams, G.. Rauscher, No Title, in: Titan. Sci. Technol., Plenum Press, Newyork, 1973: p. 108.

[43] R. Boyer, G. Welsch, E.. Colligns, Materials Properties Handbook: Titanium Alloys, ASTM International, USA, 2007.

[44] M.. Yoo, Slip, twinning, and fracture in hexagonal close-packed metals, Metall. Trans. A. 12 (1981) 409–418.

[45] H. Conrad, M. Doner, B. de Meester, Critical review: Deformation and fracture, in: Titan. Sci. Technol., Newyork, 1973: pp. 969–1005.

[46] T. Churchman, The slip modes of titanium and the effect of purity on their occurrence during tensile deformation of single crystals, Proc. R. Soc. A. 226 (1954) 216–226.

[47] M. Hansen, Constitution of binary alloys, McGraw Hill Inc, 1958.

[48] W.. Tyson, Interstitial strengthening of titanium alloys, in: R.. Jaffee, N.. Promisel (Eds.), Sci. Technol. Appl. Titan., Pergamon Press, Oxford, London, 1970: pp. 479–487.

[49] H. Conrad, Effect of interstitial solutes on the stength and ductility of titanium, Pergamon Press, London, 1981.

[50] A. Zarkades, F.. Larson, Elasticity of titanium sheet alloys, in: R.. Jaffee, N.. Promisel (Eds.), Sci. Technol. Appl. Titanium1, Pergamon Press, Oxford, London, 1970: pp. 933–941.

[51] K. Okazaki, H. Conrad, Grain Size Distribution in Recrystallized Alpha-Titanium, Trans. JIM. 13 (1972) 198–204.

[52] K. Okazaki, H. Conrad, No Title, in: Titan. Titan. Alloy., Plenum Press, Newyork, 1982: p. 429.

[53] V.. Moiseyev, Structure of Titanium alloys, in: Titan. Alloy. Russ. Aircr. Aerosp. Appl., Taylor & Francis, Boca Raton, 2006: pp. 5–8.

[54] A. Fitzner, D.. Leo Prakash, J.. da Fonseca, M. Thomas, S.. Zhang, J. Kelleher, P.

Manuel, M. Preuss, The effect of aluminium on twinning in binary alpha-titanium, Acta Mater. 103 (2016) 341–351.

[55] D.. Truax, C.. McMahon Jr, Plastic behavior of titanium-aluminum alloys, Mater. Sci. Eng. 13 (1974) 125–139.

[56] J.C. Williams, R.G. Baggerly, N.E. Paton, Deformation behavior of HCP Ti-Al alloy single crystals, Metall. Mater. Trans. A. 33 (2002) 837–850.

[57] T. Sakai, M.E. Fine, Plastic deformation of Ti-Al single cyrstals in prismatic slip, Acta Metall. 22 (1974) 1359–1372.

[58] H. Sesano, H. Kimura, No Title, in: H. Kimura, O. Izumi (Eds.), Titan. '80, 1980: p. 1147.

[59] R.. Fleischer, Substitutional solid solution hardening of titanium, Scr. Metall. 21 (1987) 1083–1085.

[60] J.. Murray, The Al-Ti (Aluminum-Titanium) System, Phase Diagrams of Binary Titanium Alloys, ASM International, Newyork, 1987.

[61] M.. Blackburn, J.C. Williams, The preparation of thin foils of titanium alloys, Metall. Trans. AIME. 239 (1967) 287–288.

[62] C.. Rhodes, J.C. Williams, The precipitation of α-phase in metastable β -phase Ti alloys, Metall. Trans. A. 6 (1975) 2103–2114.

[63] D. Banerjee, J.C. Williams, The effect of foil preparation technique on interface phase formation in Ti alloys, Scr. Metall. 17 (1983) 1125–1128.

[64] D. Benjamin, ed., Properties and Selection: Stainless Steels, Tool Materials and Special- Purpose Materials, Volume 3, ASM, Metals Park, USA, 1980.

[65] N.. Ageev, L.. Petrova, The theoretical basis of the development of the high strength metastable beta aluminum alloys of Titanium, in: R.. Jaffee, N.. Promisel (Eds.), Proc. First Int. Conf. Titan., Pergamon Press, Oxford, London, 1970: pp. 809–814.

[66] F.. Froes, J.. Capenos, M.G.. Wells, Alloy Partitioning in Beta III and Effects on Aging Characteristics, in: Proc. Second Int. Conf. Titan. Sci. Technol., Plenum Press, Boston, 1973: pp. 1621–1633.

[67] T. Nishimura, M. Nishigaki, H. Kusamichi, Aging Characteristics of Beta Titanium Alloys, in: J.C. Williams, A.. Belov (Eds.), Proc. Third Int. Conf. TitaniumTitanium Titan. Alloy. Sci. Technol. Asp., Plenum Press, Moscow, 1982: pp. 1675–1689.

[68] G. Vigier, J. Merlin, P.. Gobin, Decomposition of the Solid Solution in the All-Beta III, in: J.. Williams, A.. Belov (Eds.), Proc. Third Int. Conf. Titan. Titan. Alloy. Sci. Technol. Asp., Plenum Press, Moscow, 1982: pp. 1691–1701.

[69] W.. Pearson, Handbook of Lattice Spacings and Structures of Metals and Alloys, Volume 2, Pergamon Press, London, 1967.

[70] M.. Blackburn, J.. Feeney, Stress-induced transformations in Ti-Mo alloys, JIM. 99 (1971) 132–134.

[71] J.. Roberson, S. Fujishiro, V.. Arunachalam, C.. Sargent, Stress induced transformations in Beta III Ti alloy single crystals, Metall. Trans. A. 5 (1974) 2317,

2322.

[72] S. Hanada, O. Izumi, Deformation and Fracture of Metastable Beta Titanium Alloys (Ti–15Mo–5Zr and Ti–15Mo–5Zr–3Al), Trans. JIM. 23 (1982) 85–94.

[73] S. Hanada, O. Izumi, Correlation of tensile properties, deformation modes, and phase stability in commercial β-phase titanium alloys, Metall. Mater. Trans. A. 18 (1987) 265–271.

[74] S. Hanada, T. Yoshio, O. Izumi, Effect of plastic deformation modes on tensile properties of beta titanium alloys, Trans. JIM. 50 (1986) 496–503.

[75] S. Hanada, O. Izumi, Transmission electron microscopic observations of mechanical twinning in metastable beta titanium alloys, Metall. Mater. Trans. A. 17 (1986) 1409–1420.

[76] M. Nishimura, T. Tokunaga, H. Ohtani, M. Hasebe, Thermodynamic Calculation of Phase Equilibria in the Be-Ti-V Ternary System, J. JIM. 70 (2006) 122–125.

[77] H. Margolin, J.. Nielsen, Titanium Metallurgy, in Modern Materials, Advances in Development and Application, Volume2 ed., Academic press, 1960.

[78] R.. Jaffee, The Physical Metallurgy of Titanium Alloys, Prog. Met. Phys. 7 (1958) 149.

[79] R.. Jaffee, Metallurgical Synthesis; A Critical Review, in: R.. Jaffee, H.. Burte (Eds.), Proc. Second Int. Conf. Titan. Sci. Technol., Plenum Press, Boston, 1973: pp. 1665–1693.

[80] C.. Chen, J.. Coyne, Relationships Between Microstructure and Mechanical Properties in Ti-6Al-2Sn-4Zr-2Mo~0.1Si Alloy Forgings, in: H. Kimura, O. Izumi (Eds.), Proc. Fourth Int. Conf. Titan. ’80 Sci. Technol., The Metallurgical Society of AIME, Kyoto, 1980: pp. 1197–1207.

[81] M. Hoch, N.. Birla, S.. Cole, H.. Gegel, The Development of Heat-Resistant Titanium Alloys, 1973.

[82] H.. Gegel, M. Hoch, Thermodynamics of alpha-Stabilized Ti-X-Y Systems, in: R.. Jaffee, H.. Burte (Eds.), Proc. Second Int. Conf. Titan. Sci. Technol., Pergamon Press, Boston, 1973: pp. 923–931.

[83] H.. Gegel, J.. Ho, An Electronic Approach to Solid Solution Strengthening in Titanium Alloys, Volume 1 (, 1973.

[84] D.. Salmon, Low Temperature Data Handbook, Titanium and Titanium Alloys, 1979.

[85] M.. Godden, W.. Roberts, Ductility of Ti-Al-Ga Alloys, in: R.. Jaffee, H.. Burte (Eds.), Proc. Second Int. Conf. Titan. Sci. Technol., Pergamon Press, Boston, 1973: pp. 2207–2218.

[86] E.. Fisher, D. Dever, Relation of the C Elastic Modulus to Stability of b.c.c. Transition Metals, Acta Metall. 18 (1970) 265–269.

[87] E.. Fisher, Review of Solute Effects on the Elastic Moduli of bcc Transition Metals, in: E.. Collings, H.. Gegel (Eds.), Phys. Solid Solut. Strength., Plenum Press, 1975: pp. 199–225.

[88] C. Zener, Elasticity and Anelasticity of Metals, University of Chicago press, Chicago, 1948.

[89] H.. Flower, Microstructural development in relation to hot working of titanium alloys, Mater. Sci. Technol. 6 (2013) 1082–1092.

[90] M. Stoschka, W. Tan, W. Eichlseder, M. Stockinger, Introduction to an approach based on the alpha+beta microstructure of elements of alloy Ti-6Al-4V, Procedia Eng. 1 (2009) 31–34.

[91] R. Ding, Z.. Guo, A. Wilson, Microstructural evolution of a Ti–6Al–4V alloy during thermomechanical processing, Mater. Sci. Eng. A. 327 (2002) 233–245.

[92] S. Mironov, M. Murzinova, S. Zherebtsov, G.. Salishchev, S.. Semiatin, Microstructure evolution during warm working of Ti–6Al–4V with a colony-α microstructure, Acta Mater. 57 (2009) 2470–2481.

[93] A.. Kalinyuk, N.. Trigub, V.. Zamkov, O.. Ivasishin, P.. Markovsky, R.. Teliovich, S.. Semiatin, Microstructure, texture, and mechanical properties of electron-beam melted Ti–6Al–4V, Mater. Sci. Eng. A. 346 (2003) 178–188.

[94] L. Guo, X. Fan, G. Yu, H. Yang, Microstructure control techniques in primary hot working of titanium alloy bars: A review, Chinese J. Aeronaut. 29 (2016) 30–40.

[95] F.. Gil, M.. Ginebra, J.. Manero, J.. Planell, Formation of α-Widmanstätten structure: effects of grain size and cooling rate on the Widmanstätten morphologies and on the mechanical properties in Ti6Al4V alloy, J. Alloys Compd. 329 (2001) 142–152.

[96] J. Sieniawski, W. Ziaja, K. Kubiak, M. Motyka, Microstructure and Mechanical Properties of High Strength Two-Phase Titanium Alloys, in: J. Sieniawski, W. Ziaja (Eds.), Titan. Alloy. - Adv. Prop. Control, InTech, Croatia, 2013: p. 71.

[97] E.. Collings, Materials Properties Handbook: Titanium Alloys, ASM, Metals Park, USA, 1994.

[98] W.. Burgers, On the process of transition of the cubic-body-centered modification into the hexagonal-close-packed modification of zirconium, Physica. 1 (1934) 561–586.

[99] J.. Newkirk, A.. Geisler, Crystallographic aspects of the beta to alpha transformation in titanium, Acta Metall. 1 (1953) 373–374.

[100] A.. Mcquillan, M.. Mcquillan, Titanium, Academic press, Newyork, 1956.

[101] N.E. Paton, W.. Backofen, No TitlePlastic deformation of titanium at elevated temperatures, Metall. Trans. 1 (1970) 2839–2847.

[102] H. Conrad, Thermally Activated Deformation of á Titanium Below 0.4 TM, Can. J. Phys. 45 (1967) 581–590.

[103] H. Conrad, Effects of Interstitial Content and Grain Size on the Mechanical Behavior of Alpha Titanium Below 0.4 Tm, in: R.. Jaffee, N.. Promisel (Eds.), Proc. First Int. Conf. Titan., Pergamon Press, London, 1970: pp. 489–501.

[104] H. Conrad, B. de Meester, K. Okasaki, Strengthening of Alpha Titanium by the Interstitial Solutes in C, N, and O, in: E.. Collings, H.. Gegel (Eds.), Phys. Solid Solut. Strength., Plenum Press, 1975: pp. 1–45.

[105] J.C. Williams, M.. Blackburn, The identification of a Non-basal slip vector in Titanium and Titanium-Aluminum alloys, Phys. Status Solidi. 25 (1968) K1–K3.

[106] T.. Cass, Slip modes and dislocation substructures in titanium and titanium-aluminum single crystals, in: R.. Jaffee, N.. Promisel (Eds.), Sci. Technol. Appl. Titan., Pergamon Press, Newyork, 1970: pp. 459–477.

[107] H. Burrier, M. Amateau, E. Steigerwald, The relationship between plastic deformation and fracture in alpha titanium, 1965.

[108] E.D. Levine, Deformation Mechanisms in Titanium at low temperatures, Trans. AIME. 236 (1964) 1558–1565.

[109] C. Brehm, P. Lehr, Etude dynamique du glissement prismatique dans le cas de monocristaux de titane, Mem. Sci. La Rev. Metall. LXVIII (1971) 277–285.

[110] T. Tanaka, H. Conrad, No Title, in: Second Int. Conf. Strength Met. Alloy., ASM, 1970: p. 224.

[111] T. Tanaka, H. Conrad, Deformation kinetics for $\{10\bar{1}0\}\ \langle 11\bar{2}0\rangle$ slip in titanium single crystals below 0.4 T m, Acta Metall. 20 (1972) 1019–1029.

[112] H. Conrad, Plastic flow and fracture of titanium at low temperatures, Cryogenics (Guildf). 24 (1984) 293–304.

[113] C. Yin, M. Doner, H. Conrad, Effects of interstitial content on the texture of swaged and of recrystallized titanium wire, J. Less Common Met. 33 (1973) 229–238.

[114] M. Doner, H. Conrad, Deformation mechanisms in commercial Ti (0.5 at. pct oineq) at intermediate and high temperatures (0.3 - 0.6 tinm), Metall. Trans. 4 (1973) 1809–2817.

[115] S.. Fedotov, Dependence of the Elastic Properties of Titanium Alloys on Their Composition and Structure, in: I.. Kornilov (Ed.), Titan. Its Alloy., IPST, 1963: pp. 199–215.

[116] S.. Fedotov, Peculiarities of Changes in Elastic Properties of Titanium Martensite, in: R.. Jaffee, H.. Burte (Eds.), Proc. Second Int. Conf. Titan. Sci. Technol., Pergamon Press, Boston, 1973: pp. 871–881.

[117] L.. Burck, C.. Sullivan, C.. Wells, Fatigue of a glass bead blasted nickel-base superalloy, Metall. Trans. 1 (1970) 1595–1600.

[118] C.. Wells, C.. Sullivan, he Effect of Temperature on the Low-Cycle Fatigue Behavior of Udimet 700, Trans. ASM. 60 (1967) 217.

[119] D.. Benson, J.. Grosskreutz, G.. Shaw, Mechanisms of fatigue in mill-annealed Ti-6Al-4V at room temperature and 600°F, Metall. Trans. 3 (1972) 1239–1248.

[120] S. Suresh, Fatigue of materials, Cambridge University Press, Cambridge, 1998.

[121] L. Wagner, J.. Bigoney, Fatigue of titanium alloys, in: C. Leyens, M. Peters (Eds.), Titan. Titan. Alloy. Fundam. Appl., Wiley-VCH, Weinheim, Germany, 2003.

[122] L. Wagner, J.K. Gregory, A. Gysler, G. Lütjering, No Title, in: R.. Ritchie, J. Lankford (Eds.), Small Fatigue Cracks, TMS, Warrendale, 1986: p. 117.

[123] J.K. Gregory, No Title, in: A. Carpinteri (Ed.), Handb. Fatigue Crack Propag. Met. Struct., Elsevier Science, 1994: p. 281.

[124] N.. Turner, W.. Roberts, Fatigue behavior of titanium(Ti fatigue properties, noting minor importance of strain aging, annealing effects and dislocation locking), Trans. AIME. 242 (1968) 1223.

[125] J.. Robinson, C.. Beevers, The Effects of Load Ratio, Interstitial Content and Grain Size on Low- Stress Fatigue Crack Propagation in-Titanium, Met. Sci. J. 7 (2013) 153–159.

[126] A. Gysler, J. Lindigkeit, G. Lütjering, No Title, in: P. Haasen, V. Gerold, G. Kostorz (Eds.), Proc. 5th Int. Strength Met. Alloy., Pergamon Press, 1979: p. 1113.

[127] G.T. Gray, G. Lütjering, No Title, in: C.. Beevers (Ed.), Fatigue ’84, EMAS, 1984: p. 707.

[128] L. Wagner, G. Lütjering, No Title, in: Titan. ’88 Sci. Technol., Les Editions de Physique, 1988: p. 345.

[129] J.M. Larsen, T. Nicholas, A.W. Thompson, J.C. Williams, No Title, in: R.. Ritchie, J. Lankford (Eds.), Small Fatigue Cracks, TMS, Warrendale, 1986: p. 499.

[130] M. Peters, G. Lutjering, No Title, 1983.

[131] L. Wagner, G. Lütjering, R.I. Jaffee, Microstructure/Property Relationships in Titanium Aluminides and Alloys, TMS-AIME, 1991.

[132] L. Wagner, G. Lütjering, No title, Z. Met. 87 (1987) 369.

[133] G.W. Kuhlman, Microstructure/Property Relationships in Titanium Aluminides and Alloys, TMS-AIME, 1991.

[134] R.R. Boyer, J.A. Hall, Titanium ’92: Science and Technology, TMS, Warrendale, 1993.

[135] G.R. Yoder, L.A. Cooley, T.W. Crooker, Fatigue Crack Propagation Resistance of Beta-Annealed Ti-6Al-4V Alloys of Differing Interstitial Contents, Metall. Trans. 9 (1978) 1413–1420.

[136] G.R. Yoder, F.H. Froes, D. Eylon, Effect of Microstructure, Strength, and Oxygen Content on Fatigue Crack Growth Rate of Ti-4.5Al-5.0Mo-1.5Cr, Metall. Trans. 15 (1984) 183–197.

[137] P. Bania, D. Eylon, Fatigue Crack Propagation of Titanium Alloys under Dwell-Time Conditions, Metall. Trans. A. 9 (1978) 847–855.

[138] M. Peters, A. Gysler, G. Lütjering, Influence of Microstructure on the Fatigue Behavior of Ti-6Al-4V, in: H. Kimura, O. Izumi (Eds.), Titan. ’80 Sci. Technol., TMS-AIME, 1980: pp. 1777–1786.

Chapter 2 Temperature dependence of deformation under monotonic tensile loads

2.1 Introduction

Number of studies have been attained on mechanical properties of pure titanium [1–5]. The macroscopic deformation of the materials is associated with the yielding of individual grains, which depends on grain orientations, grain sizes, and so on. The major slip systems of hexagonal close-packed (hcp) crystals are basal, prismatic, and pyramidal [6–8] as shown in Fig. 1.8. In pure titanium, the prismatic slip is the easiest to be activated amongst all slip systems at room temperature and is prominent in slip deformation. Two possible Burgers vectors are <a> ($a/3 < 11\bar{2}0 >$) and <a + c>($a/3 < 11\bar{2}0 > + c < 0001 >$), where a and c are the lattice constants along the a-axis and c-axis, respectively. The Burgers vectors of <a>, and <a+c> are also shown in Fig. 1.8. Dislocations with the Burgers vector of <a> have the shortest length among the possible Burgers vectors, so that it is considered to be the essential one in the prismatic slip [9–16].

Mechanical properties in Ti-6Al-4V with bimodal structure of primary α nodular grains and α/ß lamellar colonies are influenced by the microstructures as the mechanical properties of primary α nodular grains and α/ß lamellar colonies are not the same [17]. In Ti-6Al-4V with bimodal microstructure, the controlling mechanism behind the temperature dependence of the yield stress is more complicated than α-Ti because the temperature dependence is influenced by the thermally activated process of dislocation glide in both α and ß phases, where the effects of solute atoms such as Al, V, and O are essential. It was reported that both solute oxygen and aluminum atoms contribute to the change of slip systems in α phase as they affect the CRSS by modifying the c/a ratio. The CRSS of prismatic slip increases as the concentration of aluminum increases as shown in Fig. 2.1. The increase in the CRSS of prismatic slip is much higher than that of basal slip [18–20], which leads to

the activation of basal slips. On the other hand, solute vanadium in ß phase is expected to decrease the yield stress of the phase by the decrease in the elastic modulus with vanadium [21].

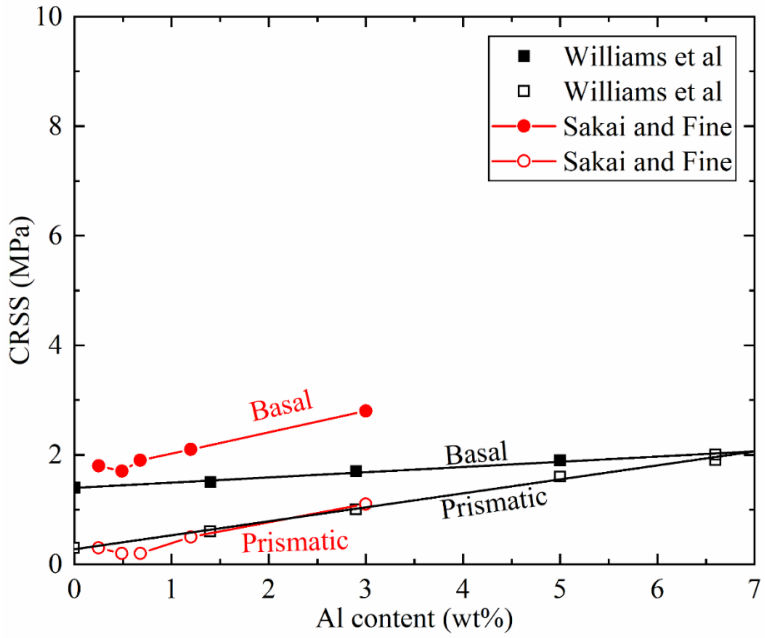

Figure 2.1. CRSS of basal and prismatic slips by changing Al content [19,20,22].

In addition to the effect of microstructure and solute atoms, the effect of temperature on mechanical properties is also very important. Various researches were performed to improve the mechanical properties of Ti-6Al-4V in different temperature ranges and strain rates varying aging and annealing temperatures of samples. Gysler *et al.* [23] studied the temperature dependence of yield stress in aged Ti-6Al-4V at between room temperature and 773 K. They showed that interstitial atoms influenced the temperature dependence of yield stress up to 573 K while there is no temperature dependence observed above 573 K. Lee *et al.* [24] investigated deformation mechanisms at high strain rates, and temperatures between room temperature and 1373 K. They mentioned that both the strain rate and temperature could affect flow stress as well as the work hardening coefficient of Ti-6Al-4V

at high strain rates. Flow stress is much more sensitive towards strain rate than temperature and increases linearly with strain rate, which suggests the deformation process is controlled by thermally activated processes. De Meester *et al.* [25] studied the deformation kinetics of Ti-6Al-4V at low temperatures (42 K to 760 K) with additional interstitials. They showed that the rate-controlling mechanism in Ti-6Al-4V is the thermally activated process of dislocations overcoming interstitial solutes. The strengthening mechanism of the alloy is governed by substitutional solid solution atoms such as Al and V. Follansbee *et al.* [26] used the Kocks-Mecking model to explain the changes in deformation mechanisms at low temperatures between low strain rates and high strain rates. The model gives a phenomenological view of thermally activated interactions of dislocations. They found that the rate of strain-hardening at low temperatures is quite higher than those expected. It is due to the contribution from the athermal component. Although substantial studies were continuing on studying mechanical properties of Ti-6Al-4V, less focus has been given to the dislocation activity by precise altering of the temperature range in bimodal microstructure which was emphasized in the present study.

It is substantial to study effective stress to understand thermally activated processes. Obtaining the value of activation enthalpy for yielding gives an insight into the slip activities which control the temperature dependence of yielding in the bimodal Ti-6Al-4V in the viewpoint of thermally activated processes. In this chapter, therefore, the temperature dependence of mechanical properties of Ti-6Al-4V with the bimodal structure was investigated highlighting effective stress and activation enthalpy to determine slip activities. The temperature dependence of yield stress, effective stress, activation volume, and activation enthalpy was measured from the results obtained by tensile tests. The temperature dependence of activation enthalpy for yielding was investigated in detail in

order to discuss the thermally activated process which controls the yielding in the bimodal Ti-6Al-4V employed in this study.

2.2. Experimental

Titanium alloy with 6 mass% of aluminum and 4 mass% of vanadium along with some substitutional (Fe, Si) and interstitial (O, traces of N, H) was employed in this study. The precise composition of the alloy is as shown in Table 2.1. The prior processing was performed to obtain bimodal microstructure. The processing history is as follows; a hot-forged billet was heat-treated at 1213 K for 2 hours followed by normalising at 978K for 3 hours, and then air-cooled.

Table 2.1. Chemical composition of the alloy used in the study.

Element	**Al**	**V**	**O**	**Fe**	**Si**	**Ti**
Mass %	6.2	4.2	0.17	0.21	0.013	Bal

An electric discharge machine (Mitsubishi Electronic, MV1200R) was used to make tensile samples and metallography ones. Pinholes were drilled with a diameter of 2mm for holding the specimen using another electric discharge machine (Mitsubishi, RH3525). The pin holes were extended to 4mm diameter using MV1200R. The thickness of the tensile specimens was 1 mm. The length and the width of the parallel portion of the tensile specimen were 8 mm and 2 mm, respectively as shown in Fig. 2.2. Specimens were initially polished with the emery grits in the order of #320, #600, #800, #1000, #1200, #1500, #2000. Furthermore, the final mirror polishing was obtained using the suspension of colloidal silica (particle size: 0.05μm) and hydrogen peroxide mixed in 9:1 volume ratio. Metallography samples were electro-polished by using electrolyte CH_3OH and $HClO_4$ of 9:1 ratio. The microstructure was observed by using scanning electron microscopy (Hitachi, SU3400).

Tensile tests were conducted in the temperature range between 77 K and 650 K to determine the temperature dependence of yield stress, effective stress, and activation volume. Two types of tensile tests were conducted viz., continuous strain rate tests to acquire continuous nominal stress-strain curves and strain rate jump tests to obtain activation volume. The strain rate jump test was depicted in Fig. 2.3 for visualization. The initial strain rate was 5×10^{-4} s^{-1} and the strain rate was increased ten order higher in case of the strain rate jump test just after yielding for about 20 seconds. For all the conditions, a strain gauge was attached to the parallel portion of the specimen to aggregate nominal strain. At first, the parallel portion was scribed with emery paper #320, and later respective strain gauge for low temperatures (model number: KFL-02-120-C1-11N1M2, adhesive: EA- 2A), for high temperatures (model number: KFH-02-120-C1-11F2M3, adhesive: PC-12B) were adhered. Later, the adhesive EA-2A was maintained under pressure at room temperature for 24 hours while PC-12B was for 2~3 hours for better binding. The maximum capacity of all the strain gauges is up to 20000 με.

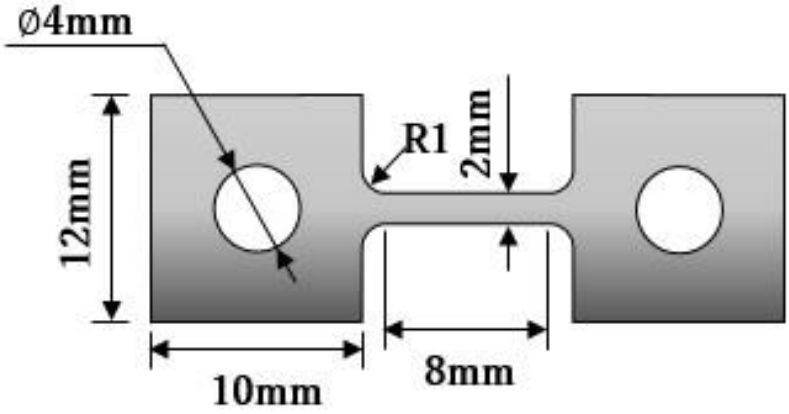

Figure 2.2. Schematic diagram of tensile specimen

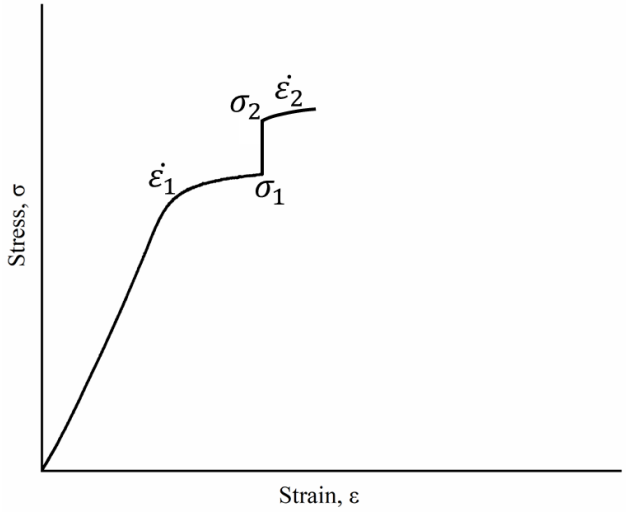

Figure 2.3. Strain rate jump test

2.3. Results

2.3.1. Bimodal microstructure of Ti-6Al-4V

Figure 2.4 show scanning electron micrographs, indicating that the microstructure of the employed Ti-6Al-4V is bimodal, containing primary α nodular grains and α/ß lamellar colonies of secondary α and ß phases. The volume fractions of α nodular and α/ß lamellar colonies are both nearly 50% where the volume fraction of α phase itself is of 97% and that of β phase itself is of 3%. The distribution of nodular grains and lamellar colonies have nearly the same volume fractions with the average grain size of 8 µm in an equivalent circular diameter. Evolution of secondary α from primary α grains is observed as shown as circular shape in Fig 2.4. (c).

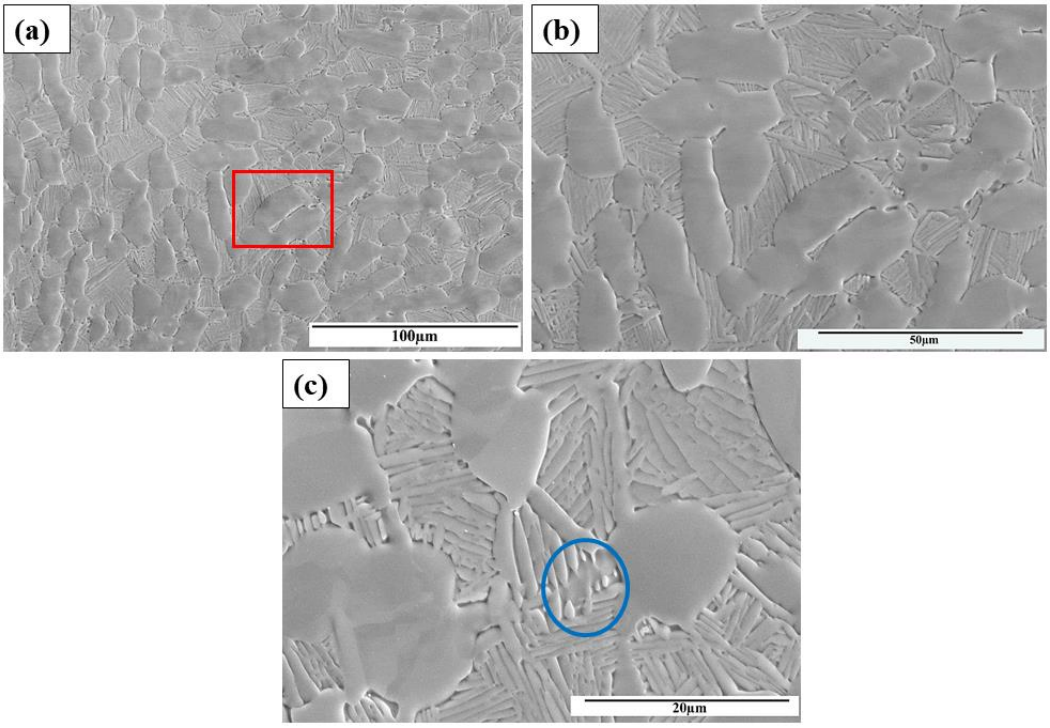

Figure 2.4 SEM micrographs of the specimen employed (a) Low magnification. (b) Enlarged image from a square indicated in (a), (c) Evolution of Secondary α.

2.3.2. Temperature dependence of yield stress in monotonic tensile tests

Figure 2.5 shows nominal stress-strain curves, indicating that yield stress decreases with increasing temperature while the total elongation has no strong temperature dependence especially at high temperatures. The reason why the total elongation shows nearly independent from temperature will not be discussed further in this thesis. However, it would depend on the temperature dependence of work-hardening. The magnitude of the work-hardening rate of hcp metals in stage II is one order lower than that of fcc crystals [27]. It is because the number of slip systems are so limited in hcp crystals that the dislocation density does not increase as does in fcc crystals. The specimen tested at 298 K possesses the highest uniform strain. Ductility is low for the specimens tested at low temperatures compared to those tested at high temperatures.

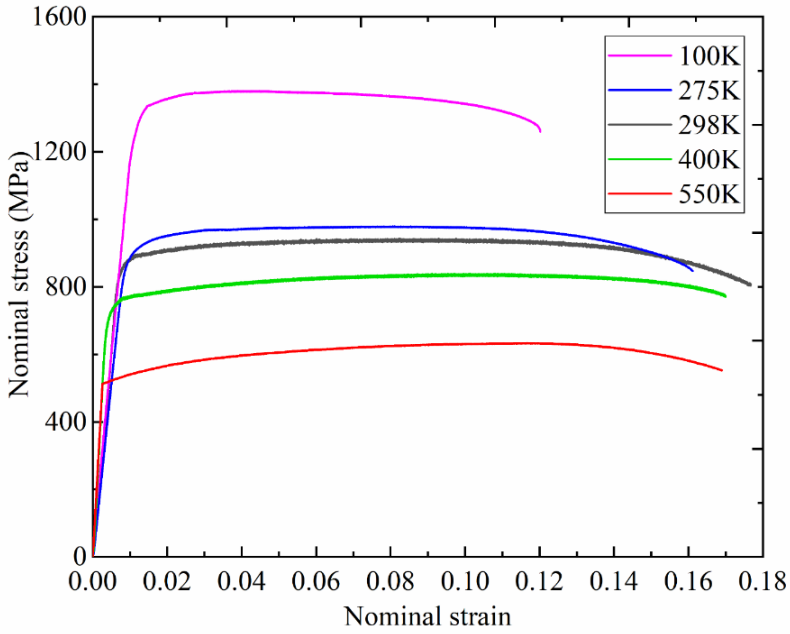

Figure 2.5 Nominal stress-strain curves at different temperatures.

Figure 2.6 (a) represents the relationship between yield stress and temperature. Here, the 0.2 % proof stress was taken as the yield stress in this study. Yield stress holds an inverse relationship with temperature although there is a strong scattering between 225 K and 300 K. Yield stress decreases with temperature, and loses the temperature dependence over at 450 K. In order to study thermally activated processes, the yield stress is divided into two components as shown in Fig. 2.6 (b). One is effective stress, which is temperature dependent, another is athermal stress which is temperature independent. The effective stress is obtained by subtracting the athermal stress from the yield stress at a given temperature as below [28,29].

$$\sigma_e = \sigma_y - \sigma_{ath}, \quad (2.1)$$

where σ_e, σ_y, and σ_{ath} are the effective stress, yield stress, and athermal stress, respectively. The effective stress infers the thermal activation of dislocation motion aided by the thermal energy of lattice vibrations. The obstacles for dislocations to overcome with the thermal activation are called short-range obstacles such as solute atoms, point defects, and Peierls potential. Athermal stress comes from the stress for dislocations to overcome long-range obstacles such as large secondary phases, and grain boundaries [28,29].

The athermal stress obtained as the average of yield stress at above 450 K in Fig.2.6 (a) is approximately 580 MPa. Here, the value of yield stress is divided into two components of effective stress and athermal stress. The controlling mechanism behind yield stress depends on the temperature range. In the athermal region, dislocation-dislocation interactions, *i.e.*, the multiplication process of dislocations play major role in the yield stress. Therefore, microstructures such as the existence of fine grains of primary alpha, and the distribution of interfaces in lamellar colonies affects the value.

Because the temperature dependence of yield stress is the main point to discuss in this study, the effects of microstructure will not be discussed further.

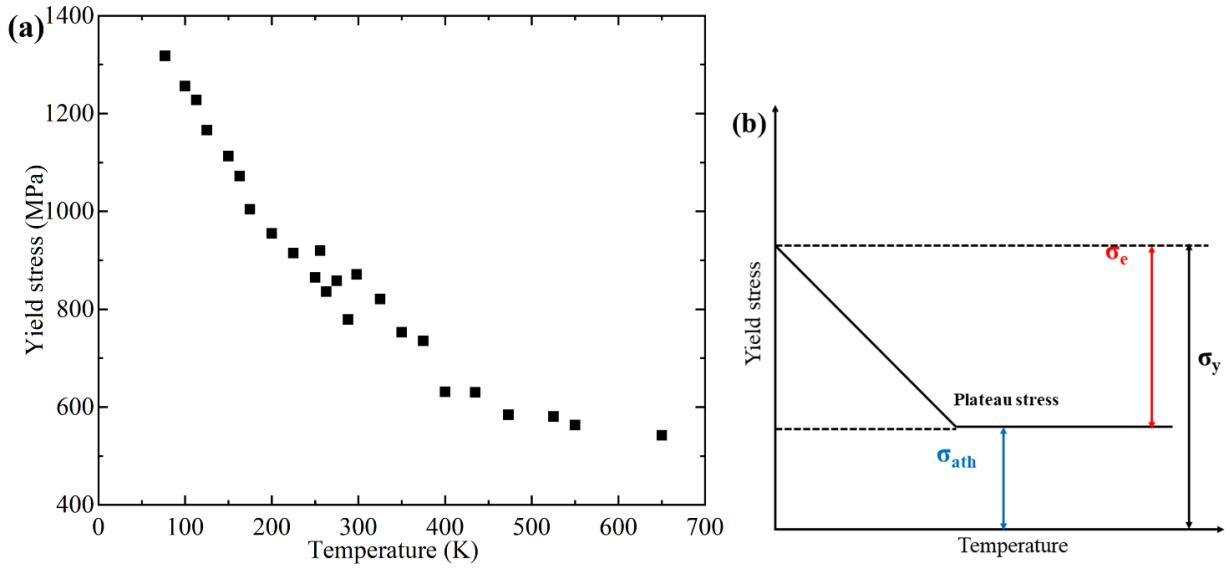

Figure 2.6 (a) Temperature dependence of yield stress obtained in this study. (b) Schematic drawing of the temperature dependence of yield stress.

2.3.3. Temperature dependence of effective stress

In order to understand thermally activated processes, it is essential to analyze the temperature dependence of effective stress. Figure 2.7 shows the temperature dependence of effective stress. Two 2nd-order polynomial fits in black and red curves are constructed in Fig.2.7 by considering the temperature dependence altered at 325 K. It is clearly indicated that different trend of the effective stress is manifested at below and above 325 K. In addition to that, it looks large scattering at the temperature range between 225 K and 300 K. The change in the trend, and the scattering of data between 225 K and 300 K suggest the change in the thermally activated process for yielding at this

temperature range. The similar characteristic of abnormality temperature range in Ti alloys is reported and summarized by Majorell *et al* [30]. The temperature range and stress levels change with precise chemical compositions, microstructures, prior processing, and heat treatments. In order to assess the change in the thermally activated process, it will be discussed with the temperature dependence of activation volume and enthalpy because they are one of the most prominent parameters relating to the thermally activated process.

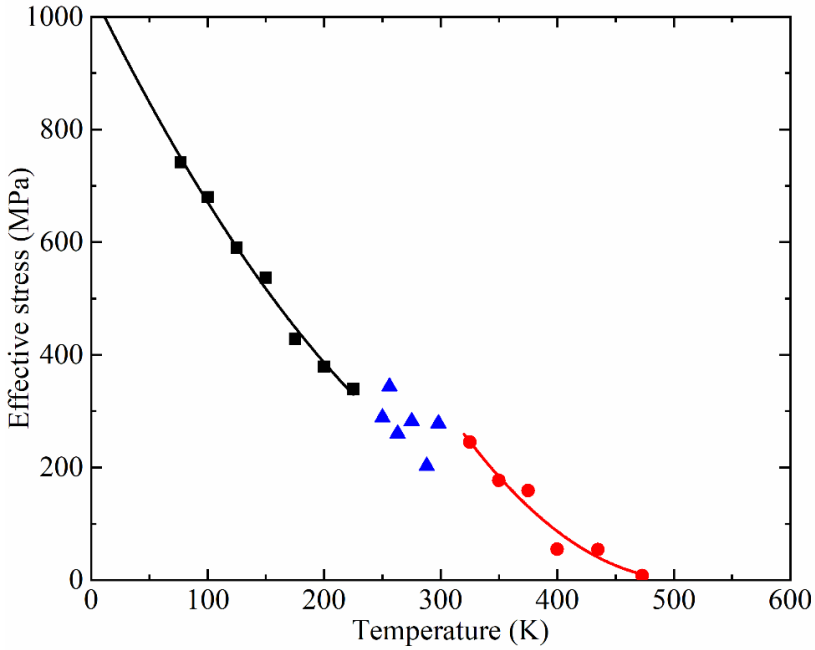

Figure 2.7 Temperature dependence of effective stress.

2.4 Discussion

2.4.1 Thermally activated process to control yielding

In the yield process, which is controlled by dislocation motion, the strain rate at yielding is given by the Orowan equation:

$$\dot{\gamma} = \rho b v, \quad (2.2)$$

where ρ is the mobile dislocation density, b is the absolute value of Burgers vector, and v is the dislocation velocity. Here, v is given by the following equation [31]:

$$v = v_0 exp[-\frac{\Delta G}{kT}], \quad (2.3)$$

where v_0 is a pre-exponential factor, $\Delta G(\tau_e, T)$ is the activation energy for dislocation glide, τ_e is the effective shear stress. Equations (2.2) and (2.3) suggest that the activation enthalpy for yielding is that for dislocation glide. Obtaining the value of activation enthalpy for yielding gives an insight into the slip activities which control the temperature dependence of yielding in the viewpoint of dislocation activities.

Change in the thermally activated processes can be explained with the help of the force-distance curve considering dislocation motion. Figure 2.8 (a) shows the force-distance curves with respect to a thermally activated process where dislocations overcome short range obstacles. Y-axis is the force acting on a dislocation per unit length denoted as F $\{f(x)\}$ in the figure when the dislocation overcome an obstacle. τ_m denotes the maximum stress for the dislocation to overcome the obstacle.

Supposing the minimum stress applied on the dislocation is zero level, a dislocation locates at the position shown in Fig. 2.8 (a) when the stress is not applied. The area under the curve colored in green represents the Helmholtz energy which is given as [29]:

$$\Delta F = \int f(x)dx, \quad (2.4)$$

Here, Helmholtz's free energy (ΔF) of the system corresponds to the total energy that a dislocation required to overcome the ascertained obstacle. The activation energy, ΔG, required for the dislocation to overcome the obstacle under the stress on the dislocations can be given as [29]:

$$\Delta G = \Delta F - \tau_e V^*, \quad (2.5)$$

where, τ_e is effective shear stress, and V^* is the activation volume. The activation volume is obtained by the multiplication of the activation area and the absolute value of the Burgers vector. The activation area is defined as the area where a dislocation swipes when it overcomes short range obstacles. ΔG corresponds to the energy which the dislocation overcoming the short-range obstacle under stress, so it thermodynamically corresponds to the Gibbs free energy. Figure 2.8 (b) visualize the relationship between ΔF, ΔG, and $\tau_e V^*$. When the stress of τ_e is applied, the equilibrium position of dislocation changes as shown in Fig. 2.8 (b). The energy for the dislocation to overcome the short range obstacles with the help of heat corresponds to ΔG while the work done on the dislocation corresponds to $\tau_e V^*$.

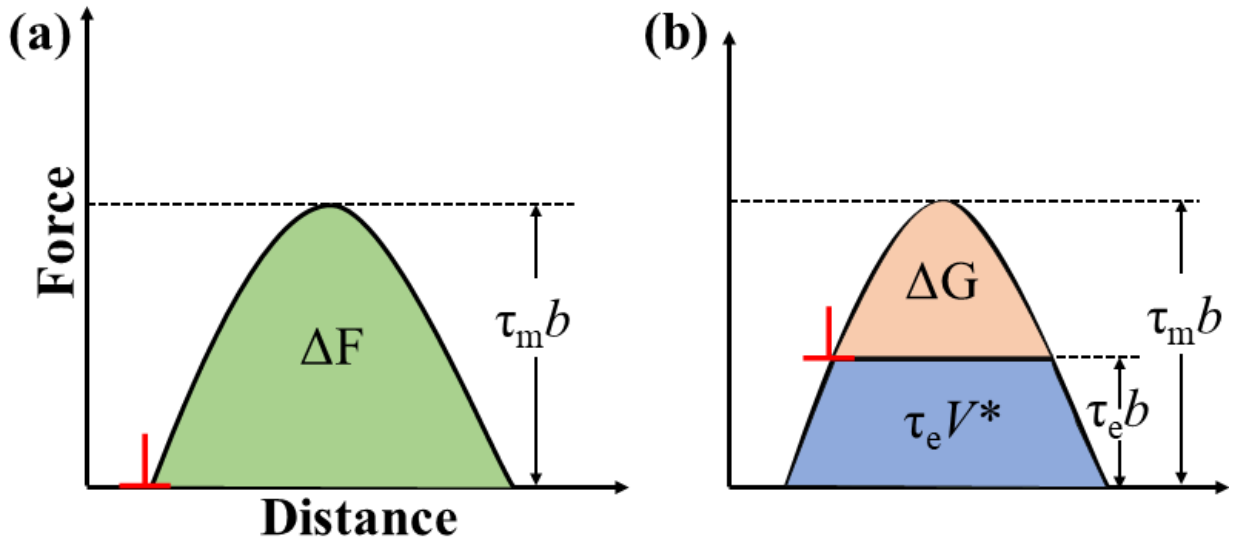

Figure 2.8. Schematic drawings of force on a dislocation when the dislocation overcome a short-range obstacle as a thermally activated process; A dislocation is represented as ⊥. (a) Without applied stress, (b) with applied stress.

Here, replacing v in Eq. (2.2) with Eq. (2.3) gives:

$$\dot{\gamma} = \rho b v_0 exp[-\frac{\Delta G}{kT}], \quad (2.6)$$

Supposing ρ and b are constant then,

$$\dot{\gamma} = \dot{\gamma}_0 exp[-\frac{\Delta G}{kT}], \quad (2.7)$$

where $\dot{\gamma}_0$ is a constant. Therefore,

$$-kln\frac{\dot{\gamma}}{\dot{\gamma}_0} = \frac{\Delta G}{T},$$

$$-k\left\{\frac{\partial l\, ln(\dot{\gamma}/\dot{\gamma}_0)}{\partial\frac{1}{T}}\right\}_{\tau_e} = \Delta G + \frac{1}{T}\left\{\frac{\partial \Delta G}{\partial\frac{1}{T}}\right\}_{\tau_e}$$

$$= \Delta G + T\Delta S(T)$$

$$\equiv \Delta H, \quad (2.8) \qquad \text{with} \left\{\frac{\partial \Delta G(\tau_e,T)}{\partial\frac{1}{T}}\right\}_{\tau_e} = -T^2\left\{\frac{\partial \Delta G}{\partial T}\right\}_{\tau_e} \equiv T^2\Delta S.$$

The equation of activation enthalpy can be modified by partial differential:

$$\Delta H = -k\left\{\frac{\partial\, ln(\dot{\gamma}/\dot{\gamma}_0)}{\partial\frac{1}{T}}\right\}_{\tau_e}$$

$$= kT^2\left\{\frac{\partial\, ln(\dot{\gamma}/\dot{\gamma}_0)}{\partial T}\right\}_{\tau_e}$$

$$= -kT^2\left\{\frac{\partial\, ln(\dot{\gamma}/\dot{\gamma}_0)}{\partial \tau_e}\right\}_T\left\{\frac{\partial \tau_e}{\partial T}\right\}_{\dot{\gamma}}, \quad (2.9)$$

Therefore, activation enthalpy can be obtained by strain rate jump tests.

2.4.2 Activation volume and activation enthalpy for yielding

In order to assess the change in the thermally activated process, the temperature dependence of activation volume and activation enthalpy were obtained. The value of activation volume is experimentally obtainable by the following equation with strain rate jump tests as explained in Fig. 2.3:

$$V^* = MkT\frac{\ln(\dot{\varepsilon}_2/\dot{\varepsilon}_1)}{\sigma_2-\sigma_1}, \quad (2.10) \quad [28]$$

where $\dot{\varepsilon}_1$ and $\dot{\varepsilon}_2$ are the strain rates before and after the strain rate jump tests respectively. σ_1 and σ_2 are the stress before and after the strain jump tests. *M* is a Taylor factor, *k* is Boltzmann constant, and *T* is the test temperature. The strain rate was raised with a factor of 10 at the total strain of approximately $4.5\text{x}10^{-3}$ during the tensile tests at each temperature.

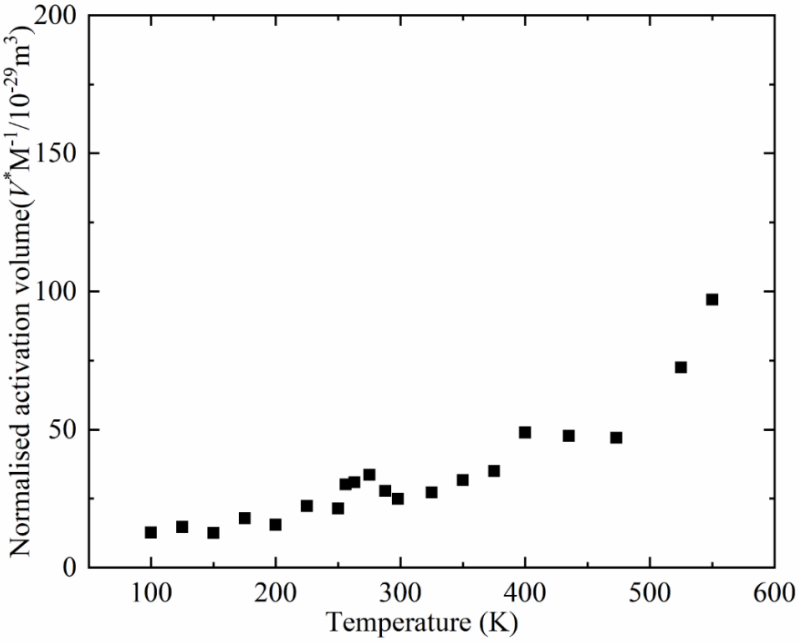

Figure 2.9. Temperature dependence of activation volume.

Figure 2.9 shows the temperature dependence of activation volume, where the y-axis was normalized by the Taylor factor (*M*). Activation volume increases with increasing temperature. The increase rate of the activation volume is different below 500 K and above 500 K. This suggests that the controlling processes for dislocations to move should change at around 500 K. It was shown in Fig. 2.7 that there is a different trend in effective stress observed at the temperature range between 225 K and 300 K, *i.e.*, as the same temperature range where the inverse temperature dependence was observed in the activation volume in Fig. 2.9. The change in the trend of the temperature dependence of effective stress in Fig.2.7 suggests that the thermally activated process which controls the yielding should change at between 225 K and 300 K. Therefore, the activation enthalpy for yielding will be investigated next.

Conrad *et al.* [32] summarised that the activation enthalpy for basal slip is higher than that for prismatic slip at any temperature in single-crystalline α-titanium. Therefore, obtaining the temperature dependence of the activation enthalpy gives an insight into the controlling mechanism behind yielding in Ti-6Al-4V. Here, activation enthalpy is obtained by the following equation replacing Eq. (2.10) with (2.9) [32]:

$$\Delta H = -\frac{TV^*}{M}\left(\frac{\partial \sigma}{\partial T}\right), \quad (2.11)$$

Figure 2.10 shows the temperature dependence of activation enthalpy obtained from Ti-6Al-4V in comparison with those for basal slips [33] and prismatic slips [31,34] obtained from single-crystalline α-Ti. Solid red plots are the results obtained in this study, *i.e.*, bimodal Ti-6Al-4V. The referred values of activation enthalpy for basal and prismatic slips are simply increased with temperature. If the yielding of Ti-6Al-4V is controlled by the activation of a single slip system such as prismatic seen in single crystals, the activation enthalpy obtained in this study should lie on the

line of prismatic or basal. However, the values of activation enthalpy from Ti-6Al-4V are plotted mostly between the regression lines from basal and prismatic slips. It is to be noted that it suggests that the controlling process of yielding Ti-6Al-4V should be the combination of both prismatic and basal slips in α phases. Therefore, slip bands that appeared on the specimen surface will be analyzed in the next chapter in order to investigate activated slip planes.

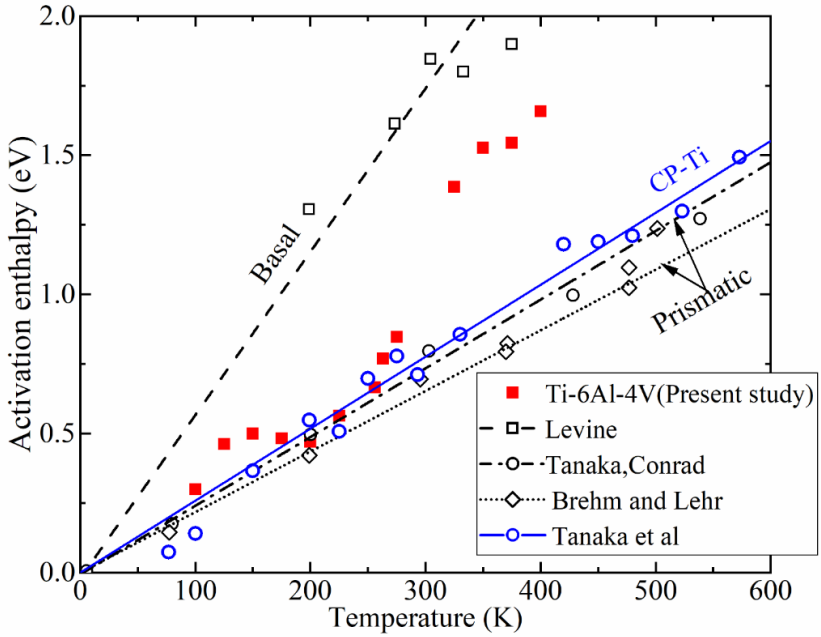

Figure 2.10. Activation enthalpy obtained from Ti-6Al-4V comparing with energy levels of basal [33] and prismatic slips [2,31,34].

2.5. Conclusions

The temperature dependence of mechanical properties was investigated in Ti-6Al-4V by performing tensile tests. The following results were obtained. Yield stress and effective stress show inverse relationships with temperature, showing the change in trend approximately at 325 K. Activation volume increases with temperature except for the temperature range between 225 K and 300 K. Temperature dependence of activation enthalpy obtained in this study suggests that both basal and prismatic slips are dominant at yielding. The trend of the temperature dependence of effective stress suggests that the controlling mechanisms behind yielding changes at between 225 K and 300 K. Thus, there is a great need to study slip activity at those temperatures to elucidate mechanisms behind the change in thermally activated processes that investigated and explained in the next chapter.

References

[1] Z. Zeng, S. Jonsson, H.J. Roven, The effects of deformation conditions on microstructure and texture of commercially pure Ti, Acta Mater. 57 (2009) 5822–5833.

[2] M. Tanaka, Y. Hayashi, Y. Okuyama, T. Morikawa, K. Higashida, Change in slip mode with temperature in Ti-0.49 mass% O, Mater. Trans. 60 (2019) 80–85.

[3] G.W. Geil, N.L. Carwile, Effect of low temperatures on the mechanical properties of a commercially pure titanium, J. Res. Natl. Bur. Stand. (1934). 54 (1955) 91–101.

[4] S.N. Monteiro, R.E. Reed-Hill, An empirical analysis of titanium stress-strain curves, Metall. Trans. 4 (1973) 1011–1015.

[5] A.M. Garde, R.E. Reed-Hill, The importance of mechanical twinning in the stress-strain behavior of swaged high purity fine-grained Titanium below 424K, Metall. Trans. 2 (1971) 2885–2888.

[6] A.T. Santhanam, R.E. Reed-Hill, The influence of strain rate dependent work hardening on the necking strain in $α$-Titanium at elevated temperatures, Metall. Trans. 2 (1971) 2619–2622.

[7] V. Vitek, M. Igarashi, Core structure of 1/3<1120>screw dislocations on basal and prismatic planes in hcp metals: An atomistic study, Philos. Mag. A. 63 (1991) 1059–1075.

[8] Y. Minonishi, S. Morozumi, {11-22}<-1-123> slip in Titanium, Scr. Metall. 16 (1982) 427–430.

[9] T. Obara, H. Yoshinaga, S. Morozumi, {11-22}<-1-123> Slip system in Magnesium, Acta Metall. 21 (1973) 845–853.

[10] D.R. Thornburg, H.R. Piehler, An analysis of constrained deformation by slip and twinning in hexagonal closed packed metals and alloys, Metall. Trans. A. 6A (1975) 1511–1523.

[11] D.J. Bacon, J.W. Martin, The atomic structure of dislocations in hcp metals II. Behaviour of the core under an applied stress, Philos. Mag. A. 43 (1981) 901–909.

[12] H. Numakura, Y. Minonishi, M. Koiwa, Atomistic study of 1/3 <1123> {1011} dislocations in hcp crystals I. Structure of the dislocations cores, Philos. Mag. A. 62 (1990) 525–543.

[13] H. Numakura, Y. Minonishi, M. Koiwa, Atomistic study of 1/3 <1123> {1011} dislocations in hcp crystals II. Motion of the dislocations, Philos. Mag. A. 62 (1990) 545–556.

[14] M.H. Yoo, c+a dislocation reactions in hcp metals, Scr. Metall. 2 (1968) 537–540.

[15] J.C. Williams, M.J. Blackburn, The identification of a Non-basal slip vector in Titanium and Titanium-Aluminum alloys, Phys. Status Solidi. 25 (1968) K1--K3.

[16] W.J.M. Tegart, No TitleIndependent slip systems and ductility of hexagonal polycrystals, Philos. Mag. 9 (1964) 339–341.

[17] Z. Wu, W.. Curtin, Mechanism and energetics of <c+a> dislocation cross-slip in hcp metals, Proc. Natl. Acad. Sci. USA. 113 (2016) 11137–11142.

[18] Y. Chong, T. Bhattacharjee, M.H. Park, A. Shibata, T. N, Factors determining room temperature mechanical properties of bimodal microstructures in Ti-6Al-4V alloy, Mater. Sci. Eng. A. 730 (2018) 217–222.

[19] J.C. Williams, R.G. Baggerly, N.E. Paton, Deformation behavior of HCP Ti-Al alloy single crystals, Metall. Mater. Trans. A. 33 (2002) 837–850.

[20] T. Sakai, M.E. Fine, Basal slip of Ti-Al single crystals, Scr. Metall. 8 (1974) 545–548.

[21] G. Lutjering, J.C. Williams, Titanium:Second edition, Springer, USA, 2007.

[22] S. Naka, A. Lasalmonie, P. Costa, L.. Kubin, The low-temperature plastic deformation of α-titanium and the core structure of a-type screw dislocations, Philos. Mag. 57 (1988) 717–740.

[23] A. Gysler, G. Lutjering, Influence of test temperature and microstructure on the tensile properties of Titanium alloys, Metall. Trans. A. 13 (1982) 1435–1443.

[24] W.S. Lee, C.F. Lin, Plastic deformation and fracture behaviour of Ti–6Al–4V alloy loaded with high strain rate under various temperatures, Mater. Sci. Eng. A. 241 (1998) 48–59.

[25] B.D. Meester, M. Doner, H. Conrad, Deformaton kinetic of the Ti-6Al-4V alloy at low temperatures, Metall. Trans. A. 6 (1975) 65–75.

[26] P.S. Follansbee, G.T. Gray III, An analysis of the low temperature, low and high strain-rate deformation of Ti-6Al-4V, Metall. Trans. A. 20 (1989) 863–874.

[27] L.M. Clarebrough, M.E. Hargreaves, Work hardening of metals, Prog. Met. Phys. 8 (1959) 1–40.

[28] T. Suzuki, T. Takeuchi, H. Yoshinaga, Dislocation dynamics and plasticity, Volume 12, Springer-Verlag, Berlin, 1991.

[29] D. Hull, D.J. Bacon, Introduction to dislocations, Fifth, Elsevier, Great Britain, 2011.

[30] A. Majorell, S. Srivatsa, R.C. Picu, Mechanical behavior of Ti–6Al–4V at high and moderate temperatures—Part I: Experimental results, Mater. Sci. Eng. A. 326 (2002) 297–305.

[31] T. Tanaka, H. Conrad, Deformation kinetics for {10-10} <11-20> slip in Titanium single crystals below 0.4Tm, Acta Metall. 20 (1972) 1019–1029.

[32] H. Conrad, M. Doner, B.D. Meester, Critical Review: Deformation and fracture in Titanium Science and Technology, Volume 2, Plenum Press, Newyork, 1973.

[33] E.D. Levine, Deformation mechanisms in titanium at low temperatures, Trans. Metall. Soc. AIME. 236 (1966) 1558–1565.

[34] C. Brehm, P. Lehr, Etude dynamique du glissement prismatique dans le cas de monocristaux de titane, Mem. Sci. La Rev. Metall. LXVIII (1971) 277–285.

Chapter 3 Trace analysis of slip deformation using EBSD

3.1. Introduction

Temperature dependence of fundamental mechanical properties such as yield stress, effective stress, activation volume, and activation enthalpy in bimodal Ti-6Al-4V was thoroughly performed in the previous chapter. It showed ambiguity in deformation mechanisms behind the change in the trend of effective stress with respect to temperature. Thus, further analysis is necessary to understand the controlling mechanisms behind thermally activated processes. One of the major differences in mechanical properties of pure Ti and Ti-6Al-4V arises from the microstructure and material with a dual phase such as bimodal Ti-6Al-4V is much more complex to deal with as explained in Chapter 1 [1,2].

There were several attempts made to study activated slip systems. Li et al [3] reported that 38% of grains deformed with basal slips, 43% of grains deformed with prismatic slips, 10% of grains deformed with pyramidal slips, and 3% of grains deformed with twins at room temperature under uniform tensile loads in Ti-6Al-4V. Among all the deformed grains, the activation of slips in primary α grains was higher compared to that in α+β lamellar colonies even after reaching higher strains. Both basal and prismatic slips activated at higher Schmid factors which are greater than 0.4. Deformed twins observed at very high Schmid factor ranging 0.48~0.5. Few grains deformed with multiple slips such as the combination of prismatic and pyramidal, or prismatic and basal. In such cases, prismatic slips were activated even with lower Schmid factors. All the activated slip systems deformed with the Schmid factors not less than 0.14. The Schmid factor of the grains with basal and prismatic at high temperature is distributed between 0.23~0.4. There was no significant change in the percentage of activated grains associated with basal and prismatic slips in comparison with room temperature [4,5]. However, the relationship between the activated slip system and the Schmid factor distribution has not

clearly understood or correlated in bimodal Ti-6Al-4V at low temperatures and at moderately high temperatures.

In the present chapter, we focus on understanding the deformation mechanisms at low, middle, and moderately high temperatures in terms of activated slip systems by analyzing traces of slip planes on the specimen surfaces, and the distribution of Schmid factors. Tensile tests were conducted in order to investigate activated slip systems at 77 K, 225 K, and 550 K. Schmid factor distributions were also demonstrated at these temperatures.

3.2. Experimental

3.2.1. Trace analysis

The material employed was bimodal Ti-6Al-4V, and sample preparation techniques until polishing were the same as those shown in Chapter 2. For slip trace analysis, tensile tests with the initial strain rate of 5×10^{-4} s^{-1} were stopped after yielding at the strain of 0.5%. Afterwards, EBSD was performed with the deformed specimens. As shown in Fig. 2.7, the trend of temperature dependence of effective stress changes around at 325 K. Therefore, trace analysis of slip planes was performed on the specimens deformed at three different temperatures *i.e.* at 77 K, 225 K, and 550 K. FE-SEM (Zeiss: Ultra 55) equipped with EBSD camera (EDAX-TSL) was used to determine crystal orientations with TSL OIM analysis 7. In general, the deformed grain leaves an impression of slip traces on the surface of the material as shown in Fig. 3.1. Plane traces of basal, prismatic, and pyramidal slips were obtained on image quality maps of EBSD. Then, the plane trace of each slip system was compared with the slip trace on the surface of deformed grains. If the slip trace of grain is identical with the plane trace of any slip system, the grain was considered to be activated in the corresponded slip system.

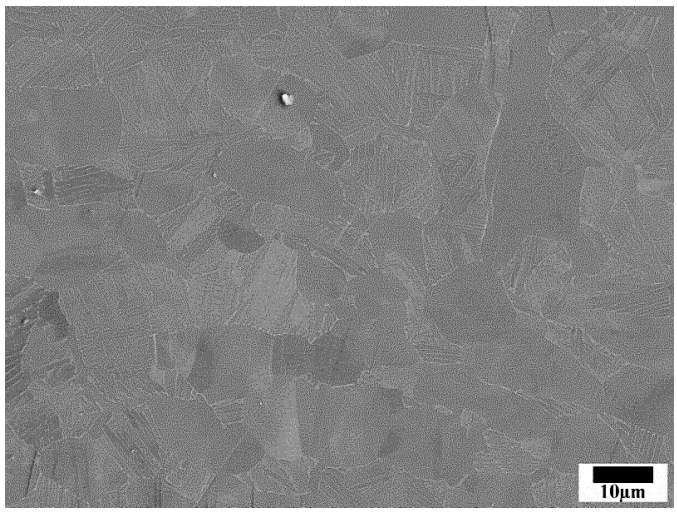

Figure 3.1. Microstructure showing slip traces at 0.5% strain.

3.2.2. Calculation of Schmid factor and Taylor factor

Schmid factor of each slip system in each grain was calculated from Euler angles obtained by using EBSD observations with the following equation:

$$P_{ij}^{(n)} = \frac{1}{2}\,(v_i^{(n)} b_j^{(n)} + v_j^{(n)} b_i^{(n)}), \qquad (3.1)$$

where $P_{ij}^{(n)}$ is a component of Schmid tensor for the nth slip system, v$^{(n)}$ is the unit vector parallel to the normal vector of slip plane, and b$^{(n)}$ is the unit vector parallel to the slip direction. The distribution of the Schmid factor with respect to each slip system of deformed grains was manifested. Taylor factor was also estimated in order to investigate the contribution of activated slip systems to the macroscopic deformation. Here, Taylor factor of *M* is defined with the macroscopic plastic strain of ε, and the summation of the values of plastic shear strain on each slip system:

$$M \equiv \frac{\sum \gamma_i}{\varepsilon}, \quad (3.2)$$

where γ_i is the shear strain of ith slip system. Some grains were not plastically deformed in the specimens even after 0.5 % of tensile deformation due to the small values of tensile strain. Taylor factor in such a specimen with elasto-plastic deformation can be expressed as follows, supposing that the plastic shear strain in each slip system is identical:

$$M_i = \frac{\sum D_i \gamma_i}{\varepsilon_i}$$

$$= \sum \frac{D_i}{Sc_i}, \qquad (3.3)$$

where D_i is the ratio of the number of deformed grains with the ith slip system to the total number of deformed grains investigated, and Sc_i is the average of the Schmid factor of the ith slip system obtained from deformed grains.

3.3. Results

3.3.1. Slip trace analysis

In order to elucidate the phenomena behind the change in the trend of effective stress, detailed trace analysis was performed identifying the slip activities at different temperatures. Figure 3.2 shows image quality (IQ) maps after the tensile deformation with 0.5% strain. Figures 3.2. (a~c), 3.2. (d~f), and 3.2. (g-i) are results from 77 K, 225 K, and 550 K, respectively. Lines in each figure indicate the traces expected to appear on the surface when basal, prismatic, or pyramidal is activated. It indicates that the basal trace shows one variant, the prismatic trace shows three variants, and the pyramidal trace shows six variants. Activated slip systems were assessed with the slip bands seen on the specimen surfaces.

Some grains exhibit slip bands on the grain surface when a grain deforms in a specific crystallographic plane, *i.e.* slip plane. Grains are considered to be activated in the specified slip system when the orientations of both the slip bands and the slip traces are identical. Fig. 3.3 (a) shows an enlarged image of the square marked in red in Fig. 3.2 (a). The line of the plane trace shown in Fig. 3.3. (a) is basal, the grain of which shows the activation of a basal slip as the slip band and the trace of the basal plane were identical. Fig 3.2 (b) shows an enlarged image of the green square in Fig. 3.2 (e). The variants of prismatic slips were drawn in a grain. The orientation of the slip band was identical to one of the variants of prismatic plane trace as the grain was activated in prismatic slip. Fig. 3.3 (c) shows an enlarged image of the blue square in 3.2 (i). The plane traces of the pyramidal slip were drawn in one of the grains. The grain was activated in pyramidal slip as the orientation of the slip band was identical to one of the variants of pyramidal.

Table 3.1 shows the percentage of grains with slip traces in the measured area of 8000 μm^2. It was found that 33% of grains were deformed at 77 K in which 66% of deformed grains are α grains, and 32% of deformed grains are α+β grains. Basal slips, prismatic slips, and

pyramidal slips were observed in 56%, 38%, and 3% of deformed grains, respectively. 3% of grains were not clearly identified between basal slips or twinning. At 225 K, 26.4% of grains were deformed. 69% of the deformed grains were α, and 31% of the deformed grains were α+β. Basal slips, prismatic slips, and pyramidal slips were observed in 53%, 41%, and 6% of the deformed grains, respectively. At 550 K, 51% of grains were deformed. 90% of the deformed grains were α while 10% of the deformed grains were α+β. Traces of basal, prismatic, and pyramidal slips were found in 22%, 24% and 53% of the deformed grains, respectively. 33% of deformed grains showed multiple slip traces, which indicates that the possibility of more than one slip systems activated in some grains.

Table 3.1. Percentage of deformed grains of each slip system in nodular and lamellae colonies.

Temperature	**P_d (%)**	**$P_{d\alpha}$ (%)**			**P_{dL} (%)**			**P_{dS} (%)**		
		Basal	***Prismatic***	***Pyramidal***	***Basal***	***Prismatic***	***Pyramidal***	***Basal***	***Prismatic***	***Pyramidal***
77 K	33	38	25	3.1	19	12.5	-	56	38	3.1
225 K	26.4	46.8	18.7	3.1	6.2	21.8	3.1	53.1	40.6	6.2
550 K	51	22.4	22.4	44.8	-	1.7	8.6	22.4	24.2	53.4

P_d: Percentage of deformed grains, $P_{d\alpha}$: Percentage of deformed α grains, P_{dL}: Percentage of deformed lamellae grains, P_{dS}: Percentage of total deformed grains in each slip system.

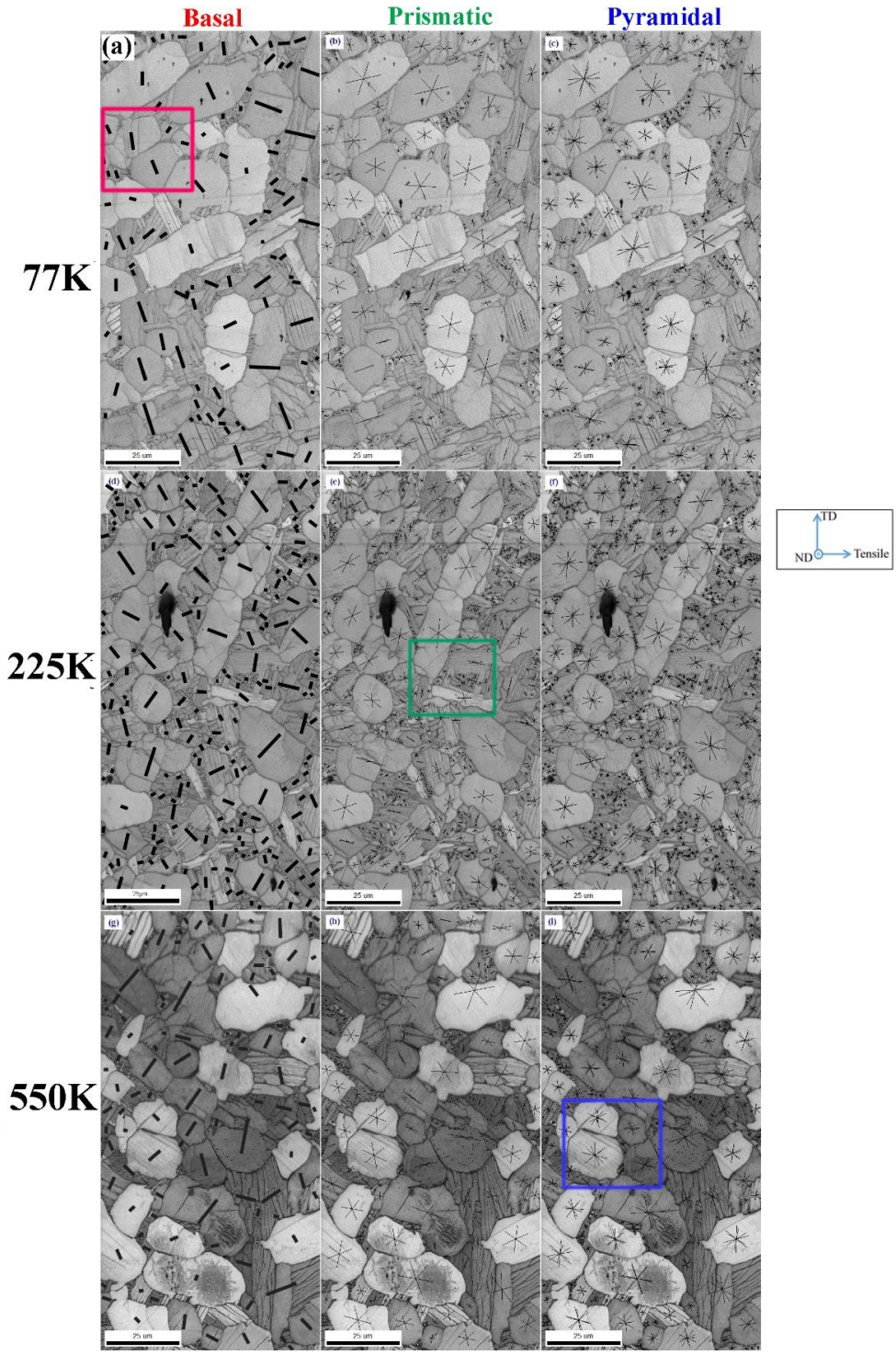

Figure 3.2. Image quality maps for trace analysis in Ti-6Al-4V, (a) expected trace of basal slip at 77 K, (b) expected trace of prismatic slip at 77 K, (c) expected trace of pyramidal slip at 77 K, (d) expected trace of basal slip at 225 K, (e) expected trace of prismatic slip at 225 K, (f) expected trace of pyramidal slip at 225 K, (g) expected trace of basal slip at 550 K, (h) expected trace of prismatic slip at 550 K, (i) expected trace of pyramidal slip at 550 K.

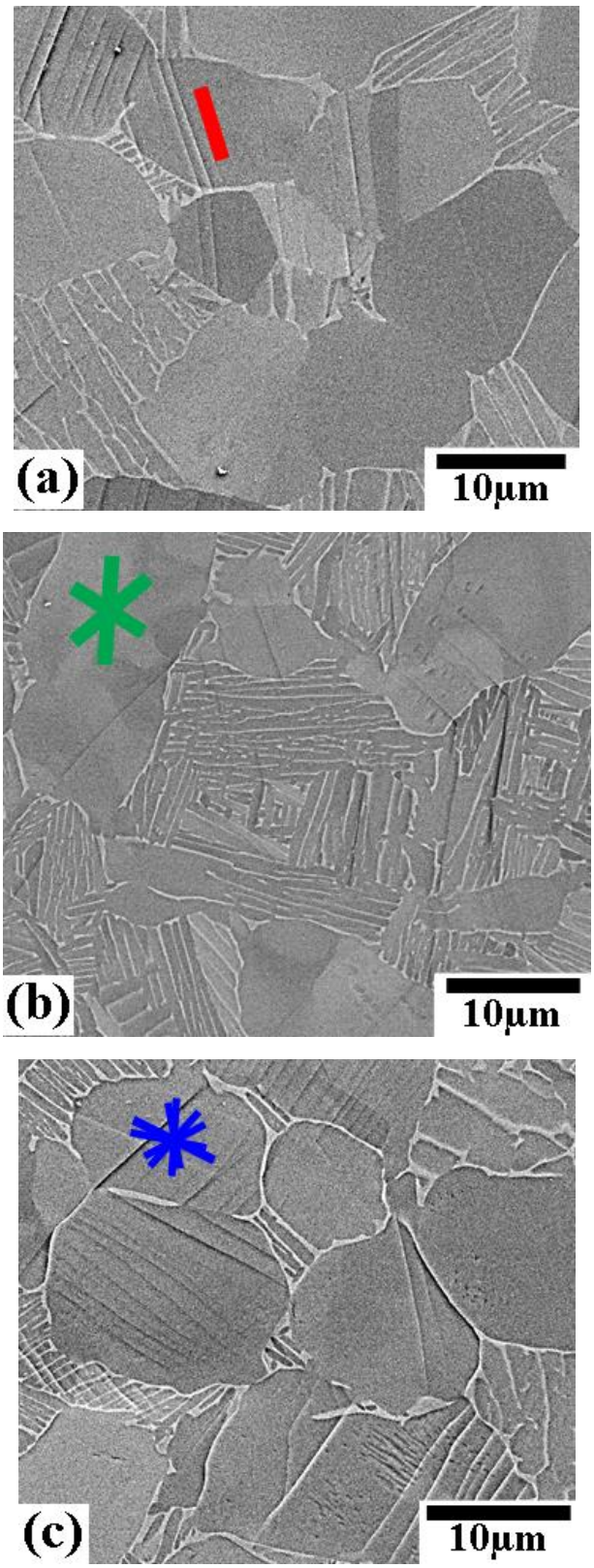

Figure. 3.3. SEM images of deformed grains corresponded to the rectangle areas in Fig.3.2. (a) grain activated in basal slip, (b) grain activated in prismatic slip, (c) grain activated in pyramidal slip.

3.3.2. Schmid factor distribution

The trace analysis does not take into account the effect of tensile direction, *i.e.*, the effect of the Schmid factor. Therefore, the distribution of the Schmid factor was also investigated. Figures 3.4 (a) and (b) show histograms of Schmid factor of each slip system from all grains in the area investigated, and deformed grains, respectively, in the specimen deformed at 77 K up to the strain of 0.05. Only the activated slip system in a deformed grain was counted for the frequency in Fig.3.4 (b). Figure 3.4 (c) shows the possibility of activated slip systems obtained by dividing data in Fig. 3.4 (b) with those in Fig.3.4 (a). Frequencies of each slip systems are put in the same bin altogether. The labels of the x-axis are put at the center of the bin, the size of which is 0.05, for example, the label of 0.425 in the x-axis means the bin width is between 0.4 and 0.45. In between the Schmid factor range of 0.2 and 0.4, only basal slips were activated as shown in Fig. 3.4 (b). Figure 3.3 (c) shows the possibility of each slip system in the grains with each Schmid factor range, which clarifies the chance of activated slip systems at a given Schmid factor eliminating the effect of the number of counted grains. Although the basal and prismatic slips have nearly similar chances to be activated in the Schmid factor larger than 0.4, the possibility of basal slips to activate is higher at Schmid factors lower than 0.4, which suggests that CRSS of basal is closer to that of CRSS of prismatic or slightly lower than that of prismatic at 77 K. It suggests that dominant slip deformations are in the grains with Schmid factors higher than 0.3. Whereas the frequency from all grains for pyramidal is the highest and basal is lowest as shown in Fig. 3.4. (a), the frequency for deformed grains for basal is the highest and lowest for pyramidal as shown in Fig. 3.4. (b). It indicates that CRSS for basal is the lowest or slightly equal to that of prismatic and pyramidal is the highest at 77 K.

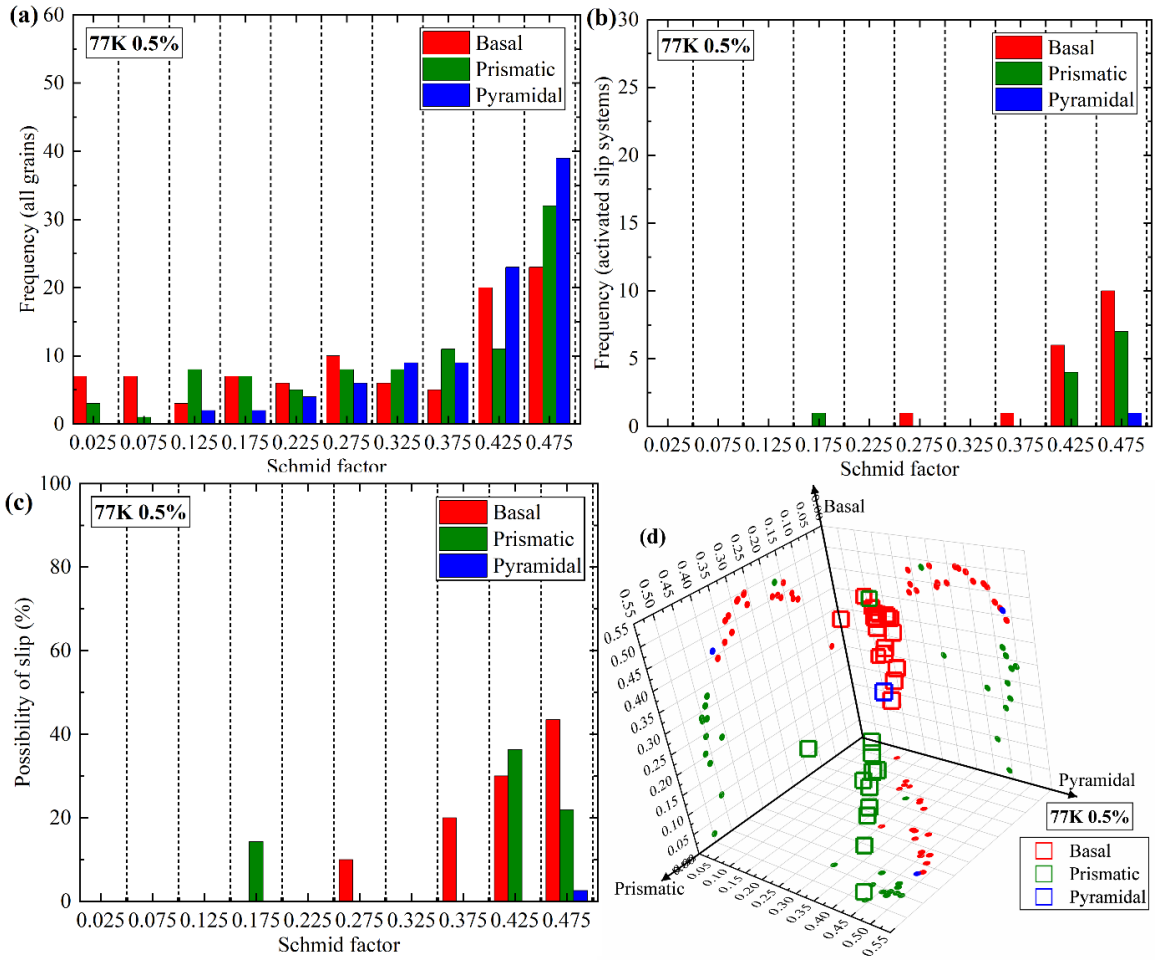

Figure 3.4. Consolidated histograms of Schmid factor for three slip systems at 77 K with the strain of 0.05. (a) for all grains, (b) for activated slip systems in deformed grains, (c) possibility of the slip activation, (d) Schmid factor distribution of activated slip systems in 3D.

Since one grain has three independent Schmid factors of basal, prismatic, and pyramidal, individually, 3-dimensional plots of Schmid factors from each grain were also obtained. Figure 3.4 (d) shows the Schmid factors of each slip system in 3-D space from deformed grains. The 3D view provides the Schmid factors of the slip systems for basal, prismatic, and pyramidal at the same time. Solid plots indicate the projections of the Schmid factor on the planes with respect to the respective axes. The 3D view helps to assess the possibility of multiple slip systems activated in the same grain in the viewpoint of Schmid factor. There were no overlapped plots in Fig. 3.4 (d) as the multiple slip traces were not observed at 77 K. It indicates that the Schmid factors of grains with basal slips have lager value than those of prismatic and pyramidal while the Schmid factor of grains with prismatic slips also had a higher value than those of basal and pyramidal. The fact that the lower boundary of the Schmid factor for the activation of basal or prismatic slips is 0.4 indicates that the CRSS for basal and prismatic are nearly the same at 77 K. Figure 3.3 also shows that Schmid factors of almost all grains with prismatic activated have the pyramidal Schmid factor higher than 0.4. However, prismatic slips were not activated. It indicates that CRSS for pyramidal slips are much higher than that for prismatic at 77 K.

Figures 3.5 (a), (b), and (c) show histograms of Schmid factors of each slip system from all grains in the area investigated, activated slip planes in deformed grains, and the possibility of slip, respectively, where the specimen was deformed at 225 K. Figures 3.5 (b) and (c) show the prismatic slips were highly activated in the grains with lower range of Schmid factors in between 0.025 and 0.3, and only a few grains were activated in basal in the Schmid factors range between 0.15 and 0.20. The possibility of activated prismatic slips is relatively higher at lower Schmid factors as shown in Fig. 3.5 (c). Figures 3.5 (b) and (c) indicate that the activation of basal and prismatic slips expanded to the whole range of Schmid factor comparing to those at 77 K. Figure 3.5 (c) also indicates that the possibility of prismatic slips was increased at low

range of Schmid factors comparing to those of other two slip systems. Pyramidal slips were only activated in the grains with the Schmid factor higher than 0.45, which is the same as that of 77 K. Fig. 3.5 (d) indicates that there are no grains with multiple slip systems are activated at 225 K.

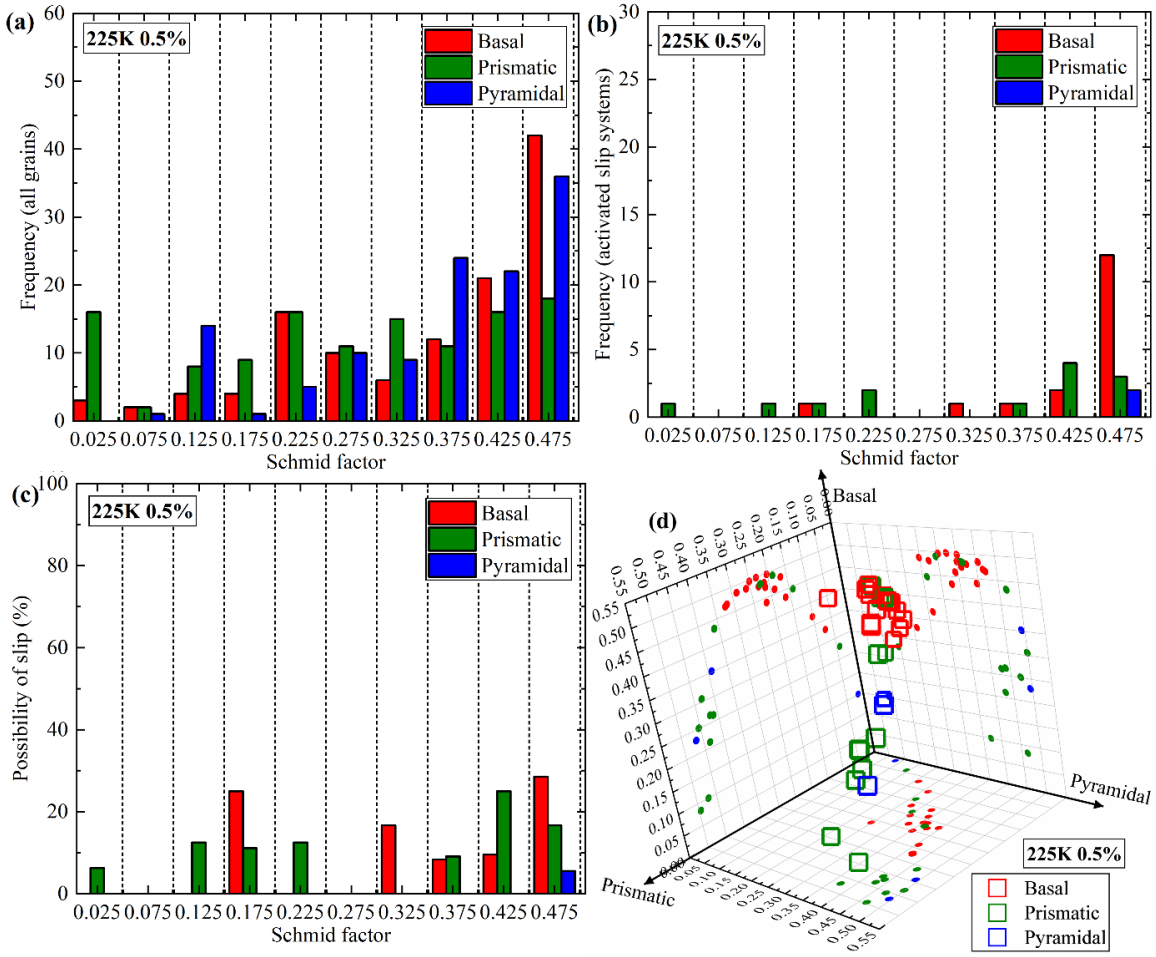

Figure 3.5. Consolidated histograms of Schmid factor for three slip systems at 225 K with the strain of 0.05. (a) for all grains, (b) for activated slip systems in deformed grains, (c) possibility of the slip activation, (d) Schmid factor distribution of activated slip systems in 3D.

Figures 3.6 (a), (b), and (c) show histograms of Schmid factors of each slip system from all grains in the area investigated, activated slip planes from deformed grains, and the possibility of slip, respectively, where the specimen was deformed at 550 K. There are no grains where neither basal nor prismatic were activated below the Schmid factor of 0.3 in as shown in Figs. 3.6 (b) and (c). The greater number of pyramidal slips were activated at 550 K comparing to the specimens deformed at 77 K or 225 K. Pyramidal slips were highly activated in the grains with the Schmid factor higher than 0.2. Although only a few grains were activated in pyramidal at 0.175 Schmid factor as shown in Fig.3.6. (b), the possibility of pyramidal slips to activate is 100% at that range as shown in Fig.3.6. (c). Figure 3.6 (d) shows the 3D plots of Schmid factors from grains with slip traces. There were several grains with multiple slip traces. The projections of all the Schmid factors were indicated in the respective planes. The overlapped data of projections represent multiple slips, *i.e.* more than one slip system has been activated in the grain. The majority of multiple slips were found in the grains with high Schmid factor of both prismatic and pyramidal while a few in grains with prismatic and basal. Prismatic slips were not activated while pyramidal slips were activated in the grain with Schmid factors of both prismatic and pyramidal lower than 0.3. It indicates that the CRSS of pyramidal becomes lower than that of prismatic at 550 K.

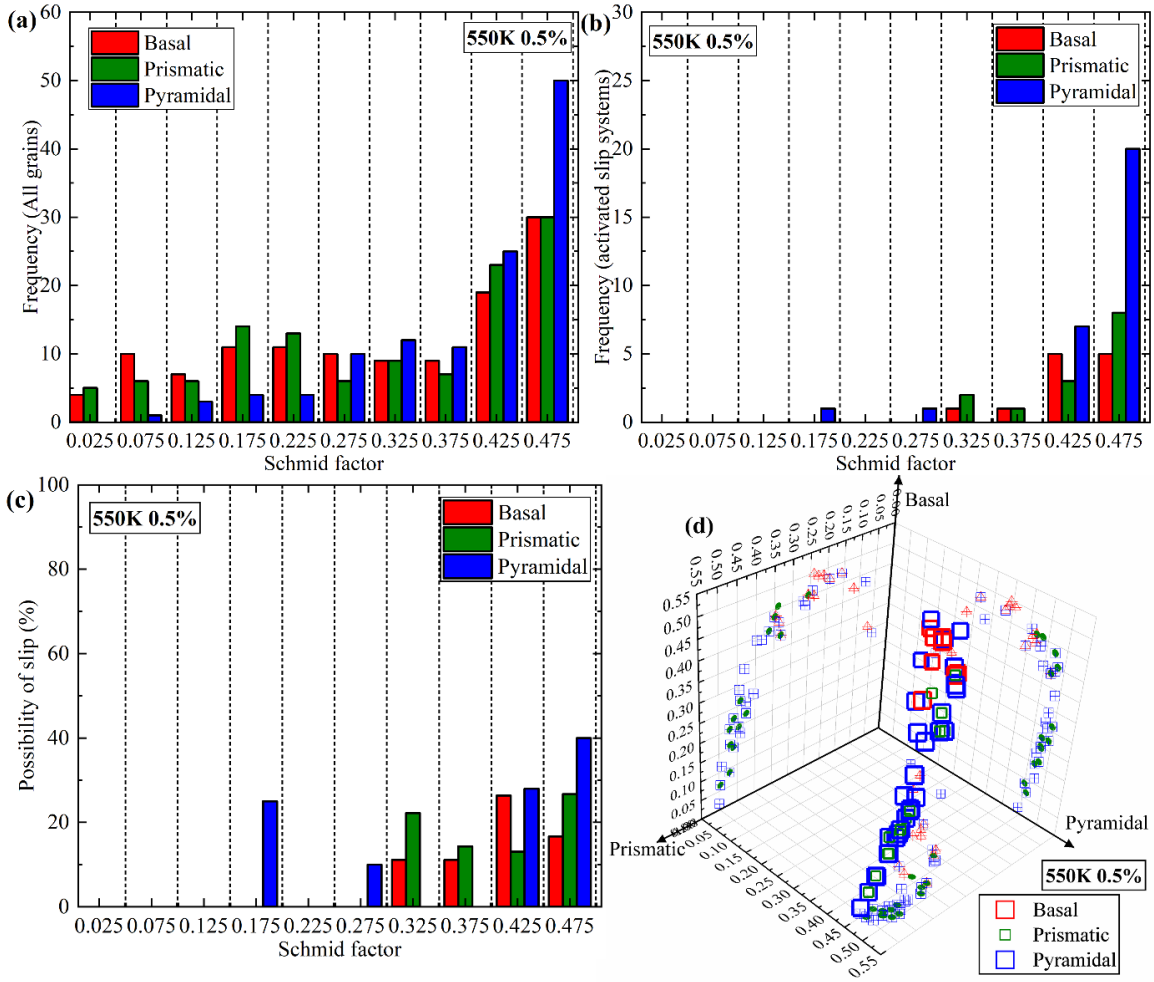

Figure 3.6. Consolidated histograms of Schmid factor for three slip systems at 550 K with the strain of 0.05. (a) for all grains, (b) for activated slip systems in deformed grains, (c) possibility of the slip activation, (d) Schmid factor distribution of activated slip systems in 3D. The projected symbols are different from those in Figs. 4 and 5 for the visibility in case of multiple slips.

3.4. Discussion

3.4.1. Taylor factor analysis

Taylor factor was estimated in order to investigate the contribution of activated slip systems to the macroscopic deformation. Figure 3.7 shows the temperature dependence of the Taylor factor, M_i for each slip system. Since the applied strain was constant, the increase in M_i from total slip systems with temperature indicates that the greater magnitude of slips contributed to the shear strain at the higher temperature. It also clarifies that the dominant slip system at 77 K and 225 K are both basal and prismatic slips while that at 550 K is pyramidal slips. However, basal slips contributed greatly to the total macroscopic strain compared to other two slips as the Taylor factor of basal slip is the highest at 77 K. Figure 3.7 also suggests that the increase in total M_i from 77 K to 225 K corresponds to the increase in M_i from prismatic and pyramidal. However, the increase rate of prismatic is higher than that of pyramidal, the percentage of deformed grains contributed to the macroscopic strain is higher in prismatic over pyramidal. The increase in total M_i from 225 K to 550 K is due to the increase in M_i from pyramidal. Prismatic and pyramidal slips became more active from 77 K to 225 K while the contribution of pyramidal increases from 225 K to 550 K.

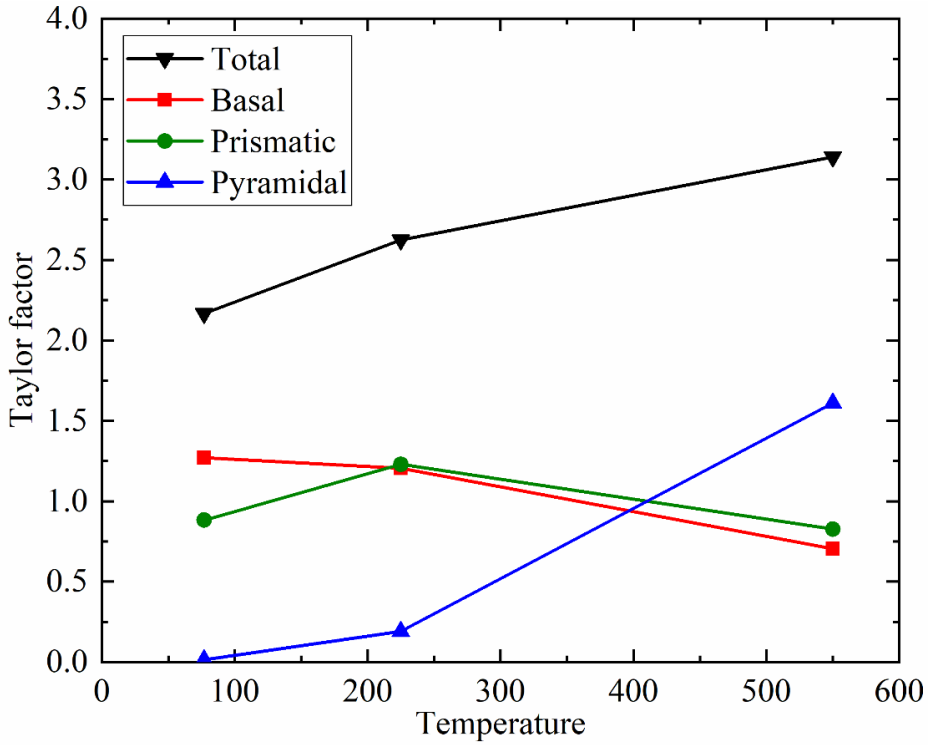

Figure 3.7. Temperature dependence of Taylor factor in each slip system.

In contrast to CP-Ti, Ti-6Al-4V used in this study deforms predominantly with basal slips at lower temperatures. It has been reported that the basal slip is activated even at cryogenic temperatures, *i.e.,* at 20 K in Ti-6Al-4V [6]. The ease of activation of the slip system has been well established by c/a ratio. When c/a has a larger ratio, basal is relatively easy to be activated and *vice versa* for prismatic [7]. The fact that c/a ratio increases with aluminum content up to 6.2 mass% suggests that the c/a ratio of primary α is larger than that of CP-Ti. It can explain that the basal slip should be dominant in Ti-6Al-4V. In order to understand the higher possibility of basal slip, the change in the CRSS of both basal and prismatic slips with an aluminum content must be taken into account.

Fig. 3.8 shows the temperature dependencies of CRSS from prismatic and basal of single-crystalline CP-Ti and Ti-6.6Al [11–13]. It indicates that CRSS of both the basal and prismatic slips increase with the aluminum content, however, the increase rate of CRSS for prismatic is larger than that for basal. The CRSS for prismatic is still slightly lower than that for basal at 77 K in Ti-6.6Al while their CRSS are nearly the same at around room temperature. The important point on the activation of basal slip in Ti-6Al-4V at 77 K even though the CRSS of prismatic is slightly lower than that of basal is presumed to be the difference in the microstructure. Bimodal Ti-6Al-4V used in this study is bimodal microstructure which has α/β interfaces, and grain boundaries between primary α and α-β lamellar colonies. There are orientation relationships of $<11\bar{2}0>_{\alpha}$ // $<111>_{\beta}$ and $\{0001\}_{\alpha}$ // $\{110\}_{\beta}$ at lamellar boundaries, which is called Burgers relationship [6]. Because of the good compatibility of continuous slip over the interfaces of α and β, it is reported that dislocations on basal slip planes channel between α and β phases without suppression while dislocations on prismatic or pyramidal slip planes cannot. This should induce the higher possibility of basal slips than prismatic at low temperatures.

At 550 K, pyramidal slip becomes dominant as shown in Fig. 3.6 and the contributions of basal and prismatic slips were relatively decreased at 550 K compared to those at 77 K and 225 K. In addition to that, the prismatic and basal slips are identically activated at 550 K as explained in Fig. 3.7. Although there is no CRSS for pyramidal available at 550 K, those results suggest that the CRSS for pyramidal becomes lower than those for basal and prismatic taking into account that the suppression of channeling of dislocations on pyramidal into β from α is not much temperature sensitive. It is concluded here that the onset of the pyramidal slips leads to the change in the trend of the temperature dependence of effective stress approximately at 325 K, *that is*, the change in the dominant active slip systems with temperature can explain the change in the trend of temperature dependence of the effective stress shown in Fig.2.7.

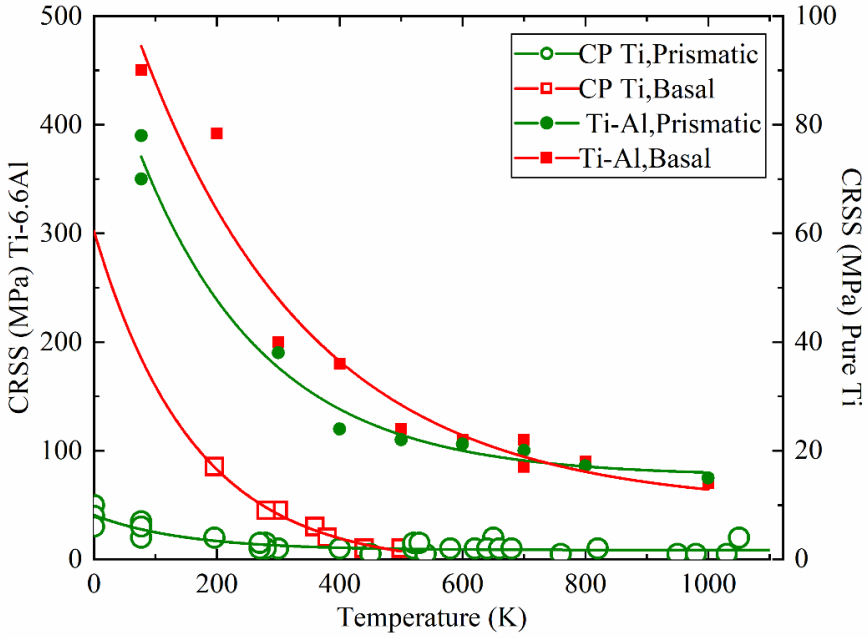

Figure. 3.8. Temperature dependence of CRSS in CP-Ti [8–10] and Ti-6.6Al [11–13].

3.5. Conclusions

The temperature dependence of deformation mechanisms was investigated in bimodal Ti-6Al-4V. The trace analysis with Schmid factor distributions indicated that basal slips are dominant at 77K, both basal and prismatic slips were identically dominant at 225 K, and pyramidal slips were dominant at 550 K. The onset of the pyramidal slips leads to the change in the trend of the temperature dependence of effective stress at around 325 K, *that is*, the change in the dominant active slip systems with temperature can explain the change in the trend of temperature dependence of the effective stress approximately at 325 K.

References

[1] B.R. Anne, M. Tanaka, T. Morikawa, Temperature dependence of activation enthalpy for yielding in bimodal Ti-6Al-4V, Mater. Trans. 60 (2019). doi:matertrans.ME201902.

[2] G. Lutjering, J.C. Williams, Titanium:Second edition, Springer, USA, 2007.

[3] H. Li, C. J.Boehlert, T. R.Bieler, M. A.Crimp, Examination of the distribution of the tensile deformation systems in tension and tension-creep of Ti-6Al-4V (wt.%) at 296K and 728K, Philos. Mag. 95 (2015) 691–729.

[4] F. Bridier, P. Villechaise, J. Mendez, Analysis of the different slip systems activated by tension in a α/β titanium alloy in relation with local crystallographic orientation, Acta Mater. 53 (2004) 555–567.

[5] S. Hemery, P. Nizou, P. Villechaise, In situ SEM investigation of slip transfer in Ti-6Al-4V: Effect of applied stress, Mater. Sci. Eng. A. 709 (2018) 277–284.

[6] A. Ambard, L. Guétaz, F. Louchet, D. Guichard, Role of interphases in the deformation mechanisms of an α/β titanium alloy at 20 K, Mater. Sci. Eng. A. 319–321 (2001) 404–408. doi:10.1016/S0921-5093(00)02003-7.

[7] S. Naka, L.P. Kubin, C. Perrier, The plasticity of titanium at low and medium temperatures, Philos. Mag. 63 (1991) 1035–1043.

[8] T. Tanaka, H. Conrad, Deformation kinetics for $\{10\bar{1}0\}\langle 11\bar{2}0\rangle$ slip in titanium single crystals below 0.4 T m, Acta Metall. 20 (1972) 1019–1029.

[9] C. Brehm, P. Lehr, Etude dynamique du glissement prismatique dans le cas de monocristaux de titane, Mem. Sci. La Rev. Metall. LXVIII (1971) 277–285.

[10] E.D. Levine, Deformation Mechanisms in Titanium at low temperatures, Trans. Metall. Soc. AIME. 236 (1966) 1558–1565.

[11] J.C. Williams, R.G. Baggerly, N.E. Paton, Deformation behavior of HCP Ti-Al alloy single crystals, Metall. Mater. Trans. A. 33 (2002) 837–850.

[12] T. Sakai, M.E. Fine, Basal slip of Ti-Al single crystals, Scr. Metall. 8 (1974) 545–548.

[13] N.E. Paton, R.G. Baggerly, J.C. Williams, Deformation and solid solution strengthening of titanium-aluminum single crystals, 1976.

Chapter 4 Effect of temperature and stress ratio on fatigue crack propagation

4.1 Introduction

The pervasive use of titanium alloys was expanded in the wide ranges of applications over the decades, among which aerospace applications are relatively preeminent. Titanium alloys often exposed to cyclic loads during applications such as aerospace, structural, etc. Fatigue failures are the persistent trouble encountered by aero-components throughout the years since the first catastrophic failure of comet airplanes in the 1950s [1,2].

The crack growth under fatigue loading can be divided into three stages *viz*., crack initiation of stage I, crack propagation of stage II, the catastrophe of stage III among which stage I and stage II decide the lifetime of a component. Generally, stage II *i.e.* crack propagation occupies most of the lifetime in case that the component has a small notch. Thus, the crack propagation regime (stage II) is the more important to investigate beyond which catastrophic failure occurs without any prior indication. Figure 4.1 shows stage II is further divided into stage IIa and stage IIb. The main crack deviates towards energetically favorable positions which depends on the local driving force around the crack tip in stage IIa, afterward, the crack grows stably in stage IIb. Many circumstantial and mutually competitive mechanisms strongly affect fatigue crack growth (FCG) rates such as fluctuations with applied load, microstructure, alloy composition, mechanical load variables, crack closure, atmosphere, temperature, etc. Fatigue crack propagation is such a complex phenomenon that cannot be comprehended or concluded by a single theory. Nevertheless, there have been several researches dedicated to annotating the theory behind the fatigue science since the origin of metal fatigue in 1829 [3].

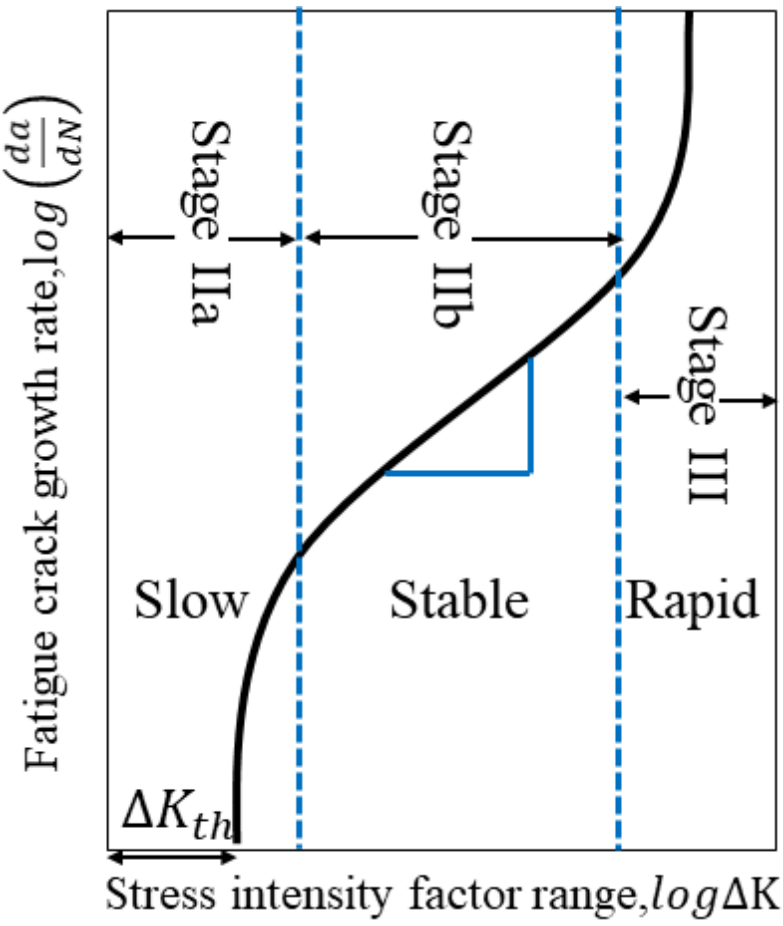

Figure 4.1. Stages of fatigue crack propagation in a notched specimen.

Several endeavors have been reported widely on the fatigue properties of many materials as well as Ti-6Al-4V. The fatigue propagation threshold in Ti-6Al-4V was first measured by G. Marci *et al* [4]. Afterwards, proceeded by the other researchers to determine the variables which affect fatigue threshold such as the effect of stress ratio of R. J. Ding *et al* [5] reported that the fatigue threshold decreases with increasing stress ratio. Fatigue threshold increases with temperature though stabilized at higher stress ratios in case $R > 0.9$. The researches also focused on the effect of crack closure on FCG in Ti-6Al-4V. The effects of several crack closure mechanisms *viz*., plasticity induced, oxide-induced, and roughness induced crack closures were studied by changing microstructure, stress ratio, load levels, environment. The decrease in the stress intensity level for the crack closure was found when the α lath size is equal to the size of the cyclic plastic zone, which is explained by slip reversibility.

Significant researches were performed on the effects of stress ratio and temperature on FCG. Xiaolong *et al* [6] studied the effect of stress ratio mainly on stage I, which revealed that the type of failures changes with stress ratio. Fracture surface with facets increased with increasing stress ratio while surface with interior facets first increases then decreased afterwards. T. Goswami [7] determined the changes in the transition between stage IIa and stage IIb by the effect of stress ratio and temperature. The transition phenomena were clearly distinguishable at lower stress ratios, whereas it was diminished at higher stress ratios. Several phenomena activated at higher temperatures such as cavity formations, secondary cracks, the interaction of secondary crack with primary crack, creep, cyclic cleavage etc. The study created ambiguity on lowering stress intensity at the tip of a dominating crack by the introduction of secondary cracks at higher stress ratios and the phenomena of voids on FCG acceleration.

Plentiful researches were reported on several dimensions in fatigue properties of Ti-6Al-4V with a variety of microstructures with pre-processing histories. A few significant

observations were accomplished on the effects of stress ratio, crack closure, and short fatigue cracks. Stress ratio pertinently contributed to the change in threshold stress intensity range, which is an important parameter for crack growth characteristics. As stress ratio increases, threshold stress intensity range decreased up to a certain value of the critical stress ratio. Crack closure was remarkably affected FCG rate at lower stress ratio ranges. Fatigue short cracks increase the FCG rate due to the local effective driving force is largely affected [8–15]. However, it is difficult to compare the results of material with different microstructure with pre-processing histories, so the fundamental theory behind fatigue should be adapted for further understanding. Furthermore, the theory behind the evolution of temperature dependence of FCG by considering several effects has not been clearly understood especially in bimodal Ti-6Al-4V. Hence, the current study mainly focuses on the understanding of temperature dependence of FCG at different stress ratios by critiquing several aspects, those can appreciably affect FCG.

4.2 Experimental methods

4.2.1 Fatigue tests

An in-situ high temperature testing machine with a function of single sinusoidal loading (CATY-T3H by Yonekura Seisakusho) equipped with a high vacuum was assigned to perform fatigue tests. A rotary pump and a turbo molecular pump were used to create the high vacuum. The machine has been equipped with a maximum load level of up to 5 kN. A specimen chamber was heated by condensing heating method. The maximum attainable temperature is 1473 K. A thermocouple was spot-welded on the parallel portion of a specimen to monitor the temperature. An optical microscope was attached to the fatigue machine to monitor the crack growth in-situ. The oxygen partial pressure during the fatigue test was approximately 10Pa. The system of the fatigue test machine was as shown in Fig. 4.2. An electric discharge machine (EDM) (Mitsubishi Electronic, MV1200R) was used to prepare all the specimens. Corner-notched specimens were used to carry out fatigue tests with the dimensions of 46 mm×10 mm×1 mm (length × width × thickness) as shown in Fig. 4.3. EDM was also used to introduce a notch in the specimen before polishing. All the specimens were fine-polished using modified colloidal silica (particle size: 0.05μm) with hydrogen peroxide with 9:1 ratio. Fatigue tests were performed in the temperature range between room temperature and 550 K at the stress ratios (R) of 0.1, 0.7, 0.8, and 0.9 under the crosshead speed of 20 mm/min (strain rate: 1.67×10^{-2} s^{-1}). Fracture surfaces and crack wakes of each specimen were observed under scanning electron microscope.

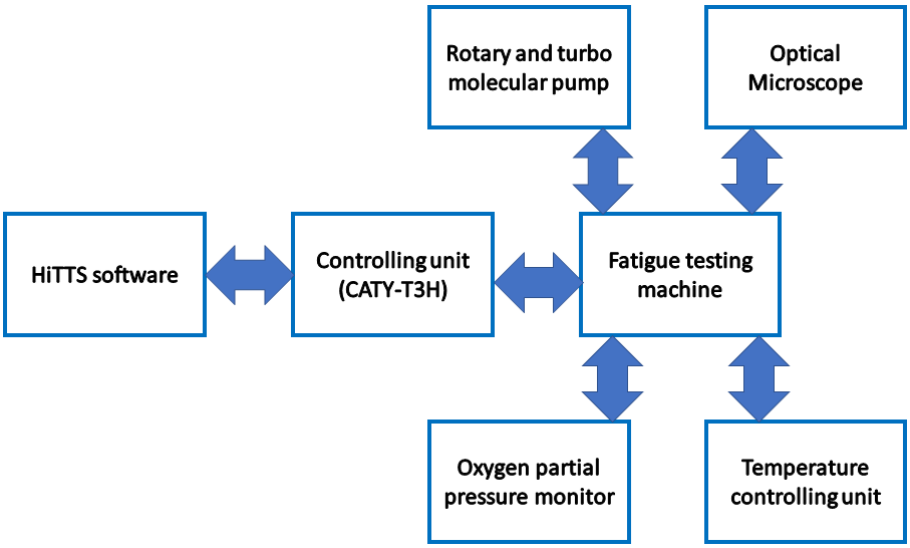

Figure 4.2. Fatigue testing system.

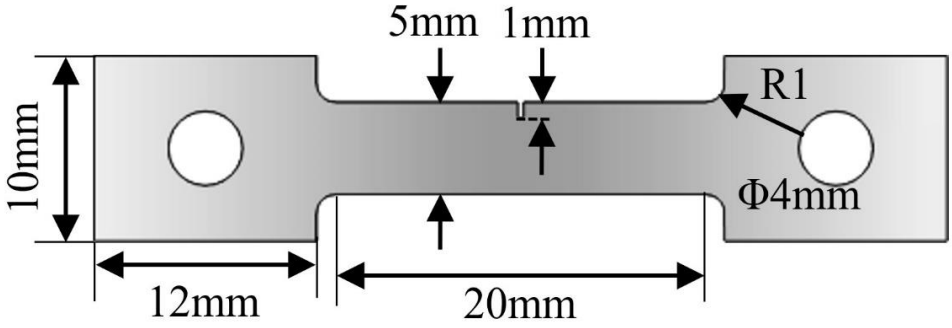

Figure 4.3 Schematic of a specimen for fatigue tests.

4.2.2 Calculations of fatigue crack length, crack growth rates and stress intensity range.

During the fatigue test, crack length was captured at a consecutive number of cycles consistently. The crack length was measured from the notch tip to the propagating crack tip at a certain number of cycles as shown in Fig. 4.4. The crack length at the n^{th} cycle is defined as:

$$a = \frac{a_n + a_{n-1}}{2}, \quad (4.1)$$

The crack growth rate (da/dN) was obtained by measuring the crack length at n^{th} cycles. The crack length at n^{th} time is $a_{(N+n)}$ of N repetitions by:

$$\frac{da}{dN} = \frac{a_n - a_{n-1}}{n-(n-1)}, \quad (4.2)$$

The stress intensity factor range, ΔK, was calculated under the criteria of operating cyclic stresses below the yield strength of the material, and the cyclic plastic zone must be sufficiently smaller than that of crack length to satisfy the small-scale yielding. The stress intensity factor and the stress intensity factor range are given by:

$$K = \sigma\sqrt{\pi a} * F(\xi),$$

$$with \ F(\xi) = 1.12 - 0.231\xi + 10.55\xi^2 - 21.72\xi^3 + 30.39\xi^4, \xi \leqq 0.6, \ (4.3).$$

$$\Delta K = K_{max} - K_{min} = (\sigma_{max} - \sigma_{min})\{\sqrt{\pi a} * F(\xi)\}, \quad (4.4)$$

where $F(\xi)$ is a shape factor which is dimensionless which depends on the specimen geometry, $\xi = {}^{a}/_{W}$ in which a is a crack length measured by the Eq. (4.1) and W is the width of the parallel portion, σ is the stress. Stress ratio is defined as:

$$R = \frac{K_{min}}{K_{max}}, \quad (4.5)$$

Fatigue tests were performed with R = 0.1, 0.7, 0.8, and 0.9 at 298 K, 350 K, 400 K and 550 K.

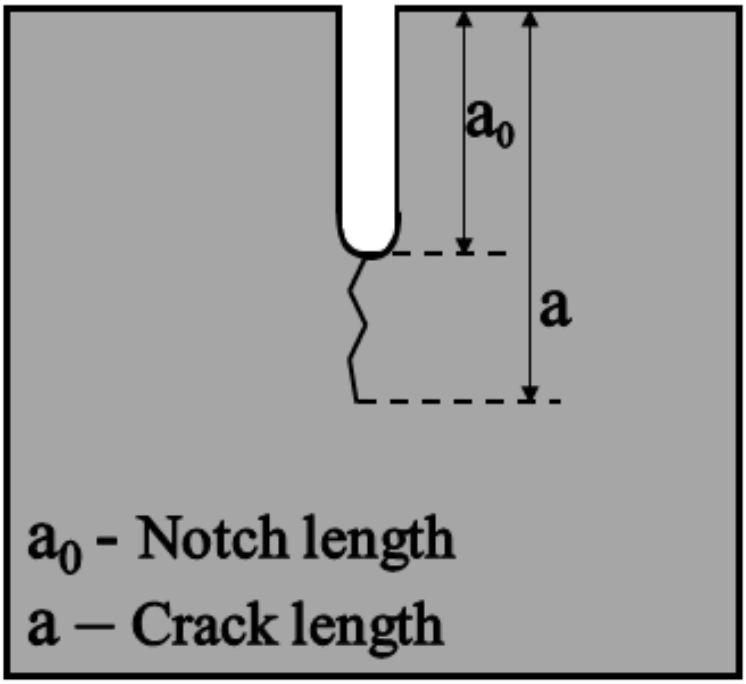

Figure 4.4. Method for measuring crack length.

4.3 Results

Figs. 4.5 (a) - (d) represent fatigue crack growth rates at several temperatures in case of R = 0.1, 0.7, 0.8, and 0.9, respectively. In stage IIb, there is a linear relationship between ln(da/dN) and ln(ΔK_I) at a constant temperature as mentioned as Paris law [16]:

$$\frac{da}{dN} = C(\Delta K_I)^n, \quad (4.6)$$

where C and n are constants depending on the material, and ΔK_I is the applied stress intensity range for mode I crack. As Paris law explains, da/dN is exponentially proportional to ΔK. The value of n in Eq. (4.6) from the specimens with R = 0.1 is 2.7. Fig.4.7 shows a fracture surface fatigued at 298 K with R = 0.1, showing typical striations on the fracture surface. The striation spacing was found to be 1.1×10^{-6}m at ΔK = 36.4 MPam$^{1/2}$, which is in good agreement with da/dN from the specimen of R = 0.1 as shown in Fig.4.5 (a). Figure 4.5 indicates that FCG rates, da/dN, for R = 0.1, 0.7 are nearly independent of temperature. FCG rates for R = 0.8 show weak temperature dependence bordering at 400 K while those of R = 0.9 shows the strong temperature dependence.

In order to elucidate the origin of the temperature dependence of da/dN, da/dN were replotted at given temperatures associated with different stress ratios. Figures 4.6 (a) – (c) indicate the da/dN with R = 0.9 is higher than those with other R when comparing at the same ΔK_I. If FCG rate is controlled by stress-controlled deformation at the crack tip, FCG rate should lie on one line at a given temperature. Figure 4.6 indicates that da/dN at 550 K with any stress ratio is on one line with respect to ΔK. At other temperatures, the results from R = 0.1, 0.7, and 0.8 are nearly on one line while the results from R = 0.9 are the exception. Those results suggest that FCG rates in cases of R = 0.1, 0.7, and 0.8 at 298 K, 350 K, 400 K, and 550 K in addition to the case of R = 0.9 at 550 K are stress controlled.

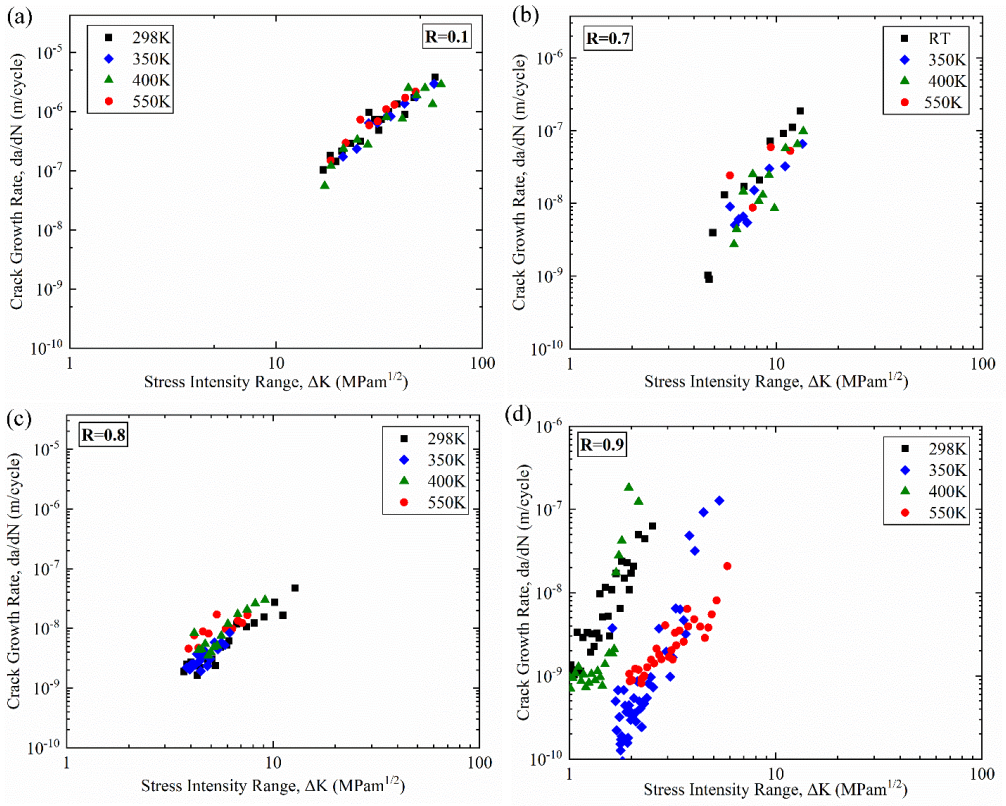

Figure 4.5. Fatigue crack growth rates of bimodal Ti-6Al-4V at various temperatures with different stress ratios. (a) R=0.1, (b) R=0.7, (c) R=0.8, and (d) R=0.9

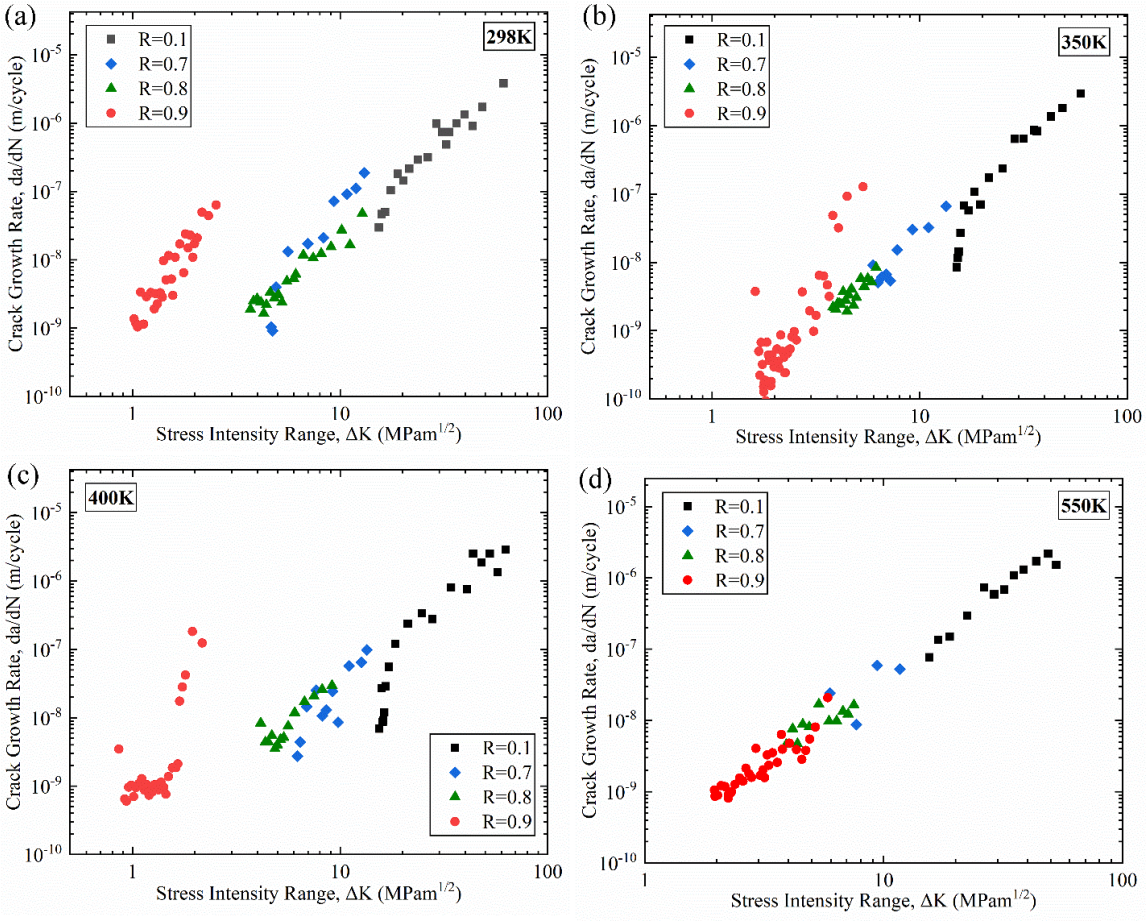

Figure 4.6. FCG rates at a given temperatures with various stress ratios. (a) 298 K, (b) 350K, (c) 400K, and (d) 550K.

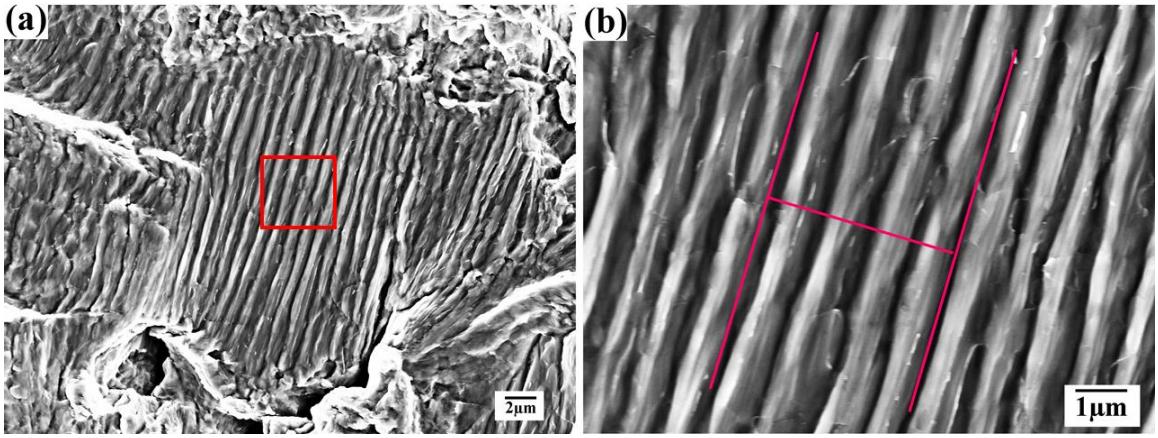

Figure 4.7. Fracture surface at 298 K, ΔK =26.5MPam$^{1/2}$, and R=0.1, (a). Striations at low magnification, (b) Spacing between striations that equals to da/dN.

4.4 Discussion

One of the major considerations behind the fatigue crack propagation at different stress ratios or temperature will be discussed. Since the FCG is due to the emission of dislocations at the crack tip, da/dN must correlate to the dislocation activities at the crack tip. Here, it is reasonable to consider that the FCG rate is controlled by dislocation emission at the crack tip. If the dislocation emission is controlled by a thermally activated process, FCG rate should also show temperature dependence. Figures 4.5, and 4.6 exhibited that the FCG rate with R = 0.9 shows temperature dependence while those with R =0.1, 0.7, and 0.8 do not. It suggests that dislocation emission at the crack tip only with R = 0.9 should be controlled by a certain thermally activated process. It is also to be noted that FCG with R = 0.1, 0.7, 0.8 is not controlled by a thermally activated process even though the propagation of the crack itself is controlled by dislocation emissions. Therefore, the change in the controlling mechanism will be discussed. First, the reasoning for temperature independence of FCG rates with R = 0.1, 0.7, 0.8 will be discussed.

4.4.1 Temperature independence of FCG rates with R = 0.1, 0.7, and 0.8.

The fact that FCG rate is on one line indicates that the FCG is controlled by stress in front of the crack, so the FCG rate increases as the stress intensity range increases. In such cases, the controlling mechanism of dislocation emission is presumed to be the change in dislocation structure in front of the crack tip. It is expected that the dislocation microstructures of fatigue should be developed in front of the crack tip before the fatigue crack propagates during the cyclic deformation, which is different from the uniform deformation in the specimen of normal tensile tests when monotonic stress applied. The dislocation microstructure developed in front of the crack is one of energetically stable, which suppresses the dislocation

emission from the crack due to the dislocation shielding. Here, the stress intensity factor range for dislocation emissions at mode I crack can be written as [17]:

$$\Delta k_{Ie} = \frac{\mu}{\sqrt{2\pi r_c}} \frac{b_s^2 + b_e^2(1-\nu)^2}{b_e sin\theta cos\frac{\theta}{2}} + |\sum k_d|, \quad (4.7)$$

where b_s and b_e are screw and edge components of the Burgers vector, respectively. μ and ν are Shear modulus and Poisson's ratio, respectively. r_c and θ are crack core size and an angle between the crack plane and slip planes, respectively. k_d is a local stress intensity factor due to dislocations with $k_d < 0$. The absolute value of $\sum k_d$ depends on the number of dislocations and the positions of the dislocations at the crack tip.

Δk_{Ie} should change every cycle reflecting the number of dislocations and the dislocation microstructure in front of the crack tip. When dislocations emitted from the crack tip, ΔK should increase because the fatigue crack length becomes longer proportional to the number of emitted dislocations. Supposing a cycle of a fatigue test, in order for the crack to propagate in the next cycle, the increase in ΔK and $|\Delta k_{Ie}|$ after one cycle should be:

$$\Delta(\Delta K) > \Delta(|\Delta k_{Ie}|). \quad (4.8)$$

When dislocations emitted from the crack tip, ΔK increases due to the increase in the crack length. When ΔK increases, the number of dislocations emitted from the crack should be increased because of higher stress intensification at the crack tip. Then, $|\Delta k_{Ie}|$ should be increased with the number of dislocations in front of the crack tip. Therefore, the number of dislocations emitted from the crack tip, *that is* da/dN, is influenced by the dislocation microstructure in front of the crack tip.

One of the metallurgical parameters to affect dislocation microstructure is the recovery of dislocations in a deformed specimen. That is, work-hardening is presumed to be the

controlling mechanism behind the FCG rate. It is known that the temperature dependence of the work-hardening rate is much weaker than that of the yield stress. Figure 4.8 (a) exhibits true stress-strain curves and work-hardening rates obtained from tensile tests at 100 K, 275 K, RT, 400 K, and 500 K. The abrupt drops of the work-hardening rate in each stress-strain curve are due to elasto-plastic deformation just after yielding. Ignoring the elasto-plastic region, the decreasing rates of work-hardening rate is nearly the same whereas the temperature deformed. Especially, those obtained at R.T., 400 K, and 500 K are identical. This supports the assumption that work-hardening controls the FCG rate, which is temperature independent in cases of R = 0.1, 0.7, and 0.8.

Furthermore, da/dN curves for different stress levels applied to the specimen to confirm the stress-controlled fatigue crack growth as shown in Fig. 4.9. Specimens were fatigued at two temperatures and two stress levels by maintaining the stress ratio of 0.1. K_{max} was set to be 117 MPa and 226 MPa. FCG rates are on the same line whereas the value of K_{max}. The slope and the trend of the FCG rates at both K_{max} levels were identical. It confirms that FCG is stress-controlled, *i.e.*, work-hardening, in case of $R \leq 0.8$. The assumption that the FCG is controlled by work-hardening can also explain the reason why the da/dN from the specimen with R = 0.9 is on the same line with the results from the specimens with R = 0.1, 0.7, and 0.8 at 550 K. The results indicate that the da/dN from the specimen R = 0.9 is also stress-controlled propagation. In the temperature dependence of yield stress as shown in Fig. 4.8 (b), 550K falls into the athermal region in which dislocation activity is not temperature dependent. Therefore, even a large value of R, FCG becomes stress-controlled at this temperature.

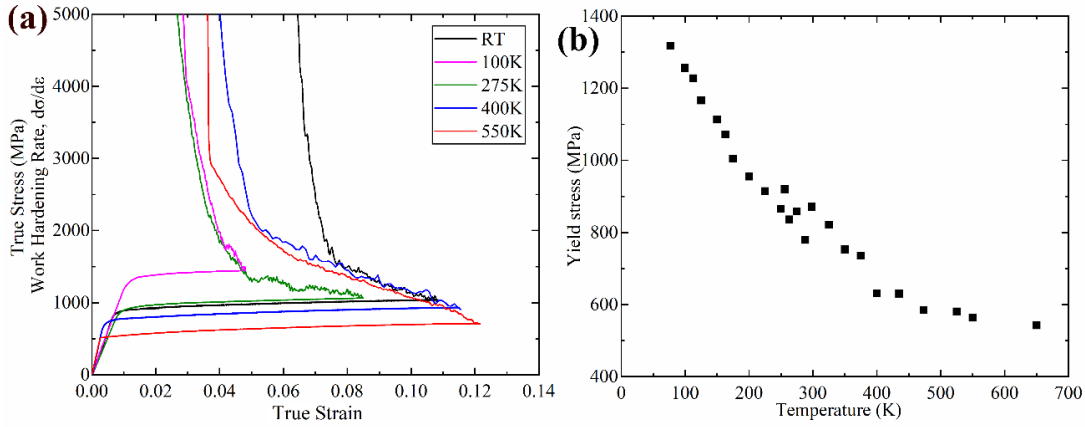

Figure 4.8. (a) Temperature dependence of work hardening rate for Ti-6Al-4V. (b) Temperature dependence of yield stress.

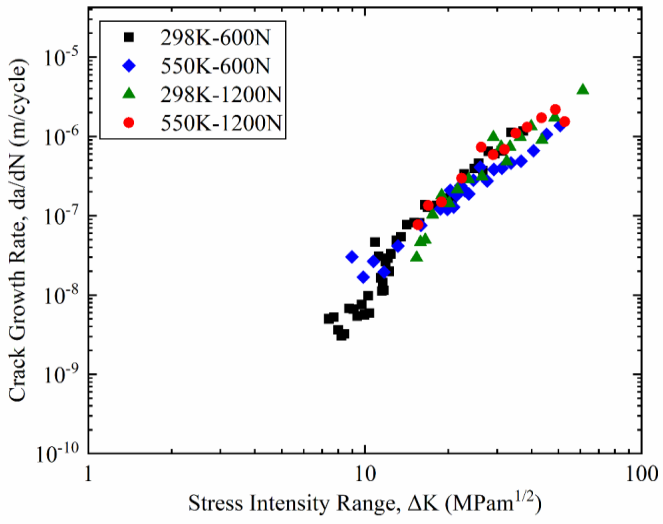

Figure 4.9. FCG rates at different K_{max} for Ti-6Al-4V preserving R=0.1.

4.4.2 Temperature dependence of FCG rate with R = 0.9.

Next, FCG rate in the case of R = 0.9 will be discussed. There are two points to discuss; one is why there is the temperature dependence of da/dN in the specimen with R = 0.9, and the other is why da/dN in the specimen with R = 0.9 is faster than those in the specimens with other values of R excepting at 550 K. First, the existence of the temperature dependence in the specimen with R = 0.9 will be discussed.

The fact there is temperature dependence if FCG rate indicates that the controlling mechanism behind it is a certain thermally activated process. In such a case, the FCG rate should be represented by an Arrhenius type equation at constant stress (or constant ΔK_I) [18]:

$$\frac{da}{dN} = A\exp\left(\frac{-\Delta H}{kT}\right), \quad (4.9)$$

where A is a constant, k is the Boltzmann constant, T is absolute temperature, and ΔH is the activation enthalpy for the rate-controlling process of the FCG rate. The dislocation velocity, v, is given by the activation enthalpy for dislocation glide, ΔH_d:

$$v = v_o\exp\left(\frac{-\Delta H_d}{kT}\right), \quad (4.10)$$

Where v_o is constant. Eqs. 4.9 and 4.10 indicate that da/dN increases with temperature with the increase in dislocation velocity when da/dN is controlled by dislocation glide, $i.e.$ in case $\Delta H = \Delta H_d$.

One of the significant differences in FCG rates under the condition of different values of K is the amount of reverse deformation during unloading. Inverse deformation must be induced at the crack tip during unloading with the condition of small R, such as R = 0.1, in order to close the crack tip during unloading while the amount of the inverse deformation is weakened at large R such as R = 0.9. It suggests that the microstructures should not be identical

at the crack tips among the specimens with different values of R, *i.e.*, dislocations need to accommodate or annihilate during unloading in case of small R while the significant accommodation of dislocations are not much necessarily in case of large R. It suggests that the plastic deformation at the crack tip at large R should be close to those just after yielding while that in case of small R should be close to the plastic deformation during work-hardening in the viewpoint of dislocation activities. Therefore, the existence of temperature dependence in the specimen with R = 0.9 suggests that the FCG rate is controlled by dislocation gliding at the crack tip. In addition to that, the increase in FCG rates with temperature as shown in Fig. 4.6 can be explained by the assumption that the dislocation velocity increases with temperature, which leads to an increase in da/dN as expected by the Eqs. (4.9) and (4.10).

Next, the reason why da/dN in the specimen is faster than those with other R will be discussed. The local driving force or local stress at a crack tip is not constant even though the applied stress is the same. The local stress at a crack tip continuously changes during crack propagation due to the changes in the crack length, crack closure, microstructural factors, etc. When the crack closure operates, a certain value of stress intensity is necessary for crack opening. The effective stress intensity factor range, ΔK_{eff}, is given as [4]:

$$\Delta K_{eff} = K_{max} - K_{op}, \quad (4.11)$$

where K_{max} and K_{op} are the maximum stress intensity factor applied, and the stress intensity factor at which fatigue crack opens, respectively, as shown in Fig.4.10 (a). The relationship between K_{max} and ΔK derive:

$$\Delta K = K_{max} - K_{min},$$

$$\frac{\Delta K}{K_{max}} = 1 - \frac{K_{min}}{K_{max}},$$

$$\frac{\Delta K}{K_{max}} = 1 - R,$$

$$\Delta K = (1 - R)K_{max}, \quad (4.12)$$

The fact that the fatigue crack keeps being sharp during propagation indicates that the minimum stress intensity factor applied, K_{min} is always smaller than K_{op}, otherwise, the crack blunts, hence

$$\Delta K_{eff} = K_{max} - K_{op} < K_{max} - K_{min} = \Delta K, \quad (4.13)$$

Equations (4.12) and (4.13) set up an inequality condition:

$$\Delta K_{eff} = K_{max} - K_{op} < (1 - R)K_{max}, \quad (4.14)$$

Equation (4.14) indicates that ΔK_{eff} linearly decreases with increasing R. If K_{op} is identical whereas the values of R as shown in Fig. 4.10 (b), ΔK_{eff} should decrease with constant K_{max}. The decrease in ΔK_{eff} induces the decrease in da/dN. It contradicts the fact that the da/dN increased in the specimen with R = 0.9 as shown in Fig. 4.5, so it should be ruled out. The other possibility is that K_{op} is increased at R=0.9 as shown in Fig. 4 10 (c), which results in the decrease in ΔK_{eff} with constant ΔK_{max}. It also contradicts the fact that the da/dN increased in the specimen with R = 0.9 as shown in Fig.4.5. Then, the left possibility is the decrease in K_{op} with constant K_{op} as shown in Fig. 4.10 (d), which results in an increase in ΔK_{eff}. It can explain the fact, as shown in Fig.4.5, that da/dN from R = 0.9 at a certain ΔK is larger than those from the specimens with R = 0.1, 0.7, and 0.8 at 298 K, 350K, and 400K. It is because of the value of ΔK_{eff} in the specimen with R = 0.9 is higher than those with other R. It is presumed that the reason why the K_{op} should be decreased in the specimen with R = 0.9 tested at 298 K, 350K, and 400K is smaller than those with R = 0.1, 0.7, and 0.8 is that the

shielding effect in the specimen with R = 0.9 is smaller than those with other R. The reason of the change in K_{op} is also presumed that the dislocation microstructure around the crack is in the specimen with R = 0.9 is different from those with other R.

Figure 4.11 shows a model to explain the change in K_{op} proposed in this study, reflecting the change in the position of the dislocation source due to crack shielding. Figure 4.11 (a) shows a motion of dislocations in front of a mode I crack during repetitive cycles. Dislocations are emitted from the crack tip under loading cycles, and then some dislocations move back to the crack under unloading cycles. The stress field of dislocations shields the crack tip, which suppresses the emission of dislocations from the crack tip. The shielding effect induces the existences K_{op} and reduces the ΔK_{eff} as shown in Eq. 4.13. Suppose a dislocation source locates in front or in the wake of a crack as shown in Fig.4. 11 (b). In the case of low R, the FCG rates depend on local effective stress intensity *i.e.* ΔK_{eff} due to the existence of the crack shielding (closure). In the case of higher stress ratio, *i.e.* R=0.9, K_{op} is decreased due to the weakening of the shielding (closure). It leads to the increase in ΔK_{eff} as expected from the Eq. 4.11, then FCG rate becomes faster as shown in Fig.4.6.

The increase in ΔK_{eff} also suggests the change in the position of dislocation sources at the crack tip because the rate of stress accumulation at the crack tip depends on ΔK_{eff}. It is considered that the dislocation source is the position where the force on a dislocation to emit becomes positive. Because of the lower shielding effect in case of high R, the position should be closer to the crack tip comparing to those with low R. The change in the position of the dislocation source also suggests that the change in the temperature dependence of FCG rate. When dislocation sources are far from the crack tip at low R that results in large plastic deformation at the crack tip as shown in Fig. 4.11(b), it is presumed that the dislocation emission from the crack tip is controlled by the internal stress field of dislocations as those of

work hardening. On the other hand, when dislocation source is near the crack tip at higher values of R as shown in Fig. 4.11 (c), there are not many dislocations emitted from the crack tip compared to those in the specimens with lower R. In this case, it is presumed that the dislocation emission from the crack tip should be controlled by dislocation glide. Dislocation structure in front of the crack tip is also expected to be changed with either higher or lower stress ratios as a result of changing in dislocation emission sources and their positions.

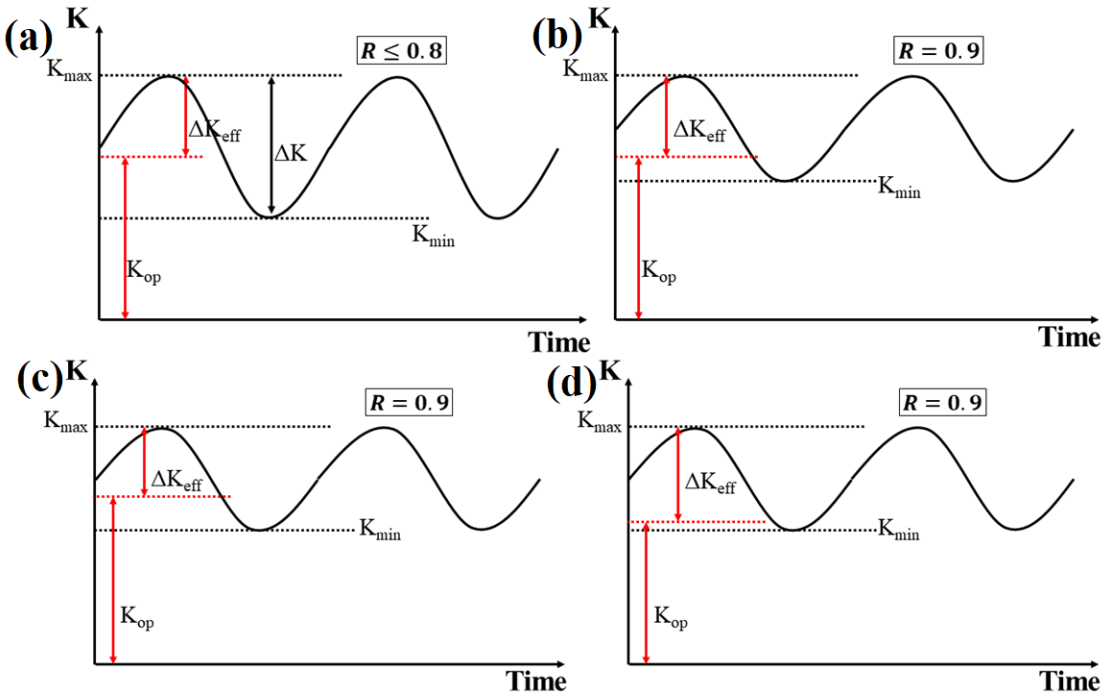

Figure. 4.10. The schematic of the change in ΔK_{eff} and K_{op} levels at lower and higher R ratios.

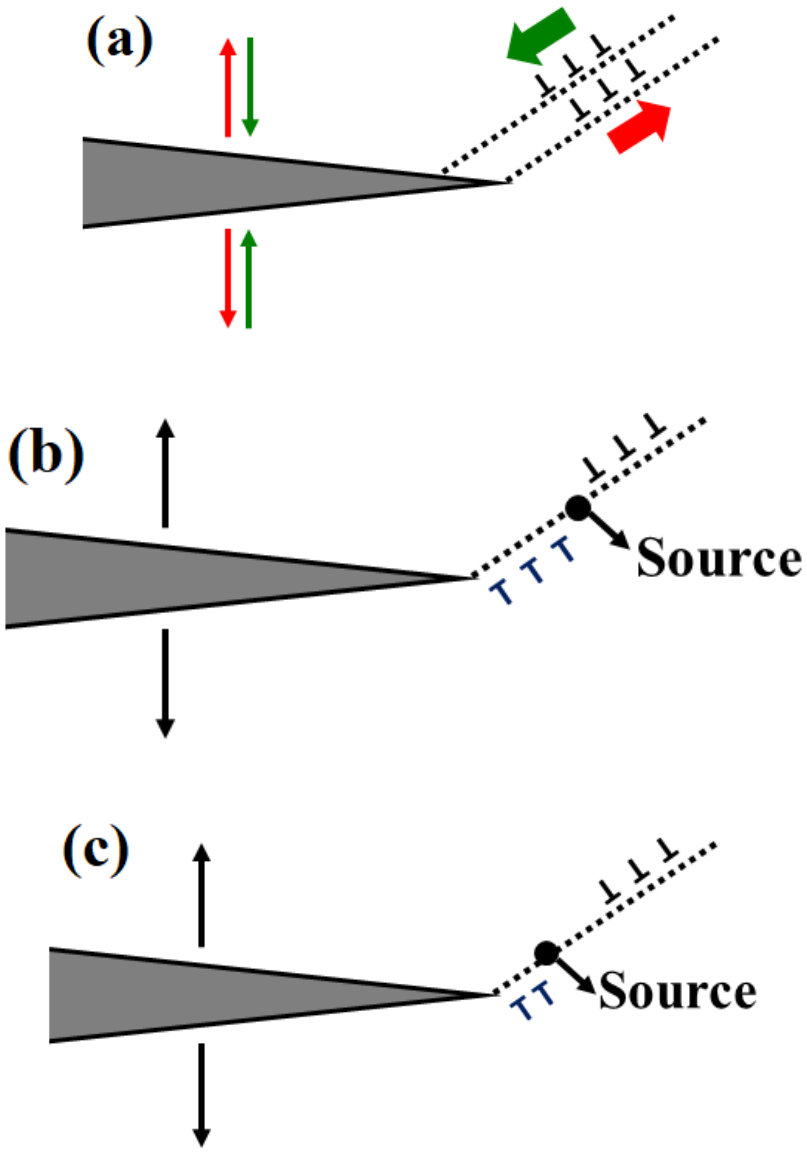

Figure 4.11. Model to explain the position of dislocation source. (a) dislocation emission and absorption, (b) dislocation source at lower stress ratios, (c) dislocation source at higher stress ratio.

4.5. Conclusions:

The effect of stress ratio on the temperature dependence of FCP was investigated in bimodal Ti-6Al-4V. FCG rates were nearly independent of temperature in cases of R = 0.1, 0.7, and 0.8 while it is dependent on temperature in the case of R = 0.9. It can be explained by the assumption that the fatigue crack is controlled by work-hardening in the conditions of R $\leq$ 0.8 while it is controlled by dislocation glide in the condition of R = 0.9.

References:

[1] D.D. Dempster, The tale of the Comet: The story of the British Jet Airliner, Technol. Cult. 2 (1961) 291–293.

[2] H. Petroski, Invention by design: how engineers get from thought to thing, Cambridge, Harvard University Press, London, 1996.

[3] W.A.. Albert, Über Treibseile am Harz, Arch. Für Mineral. Geognosie Bergbau Und Hüttenkd. 10 (1838) 215–234.

[4] G. Marci, D.. Castro, V. Bachmann, Fatigue crack propagation threshold, J. Test. Eval. 17 (1989) 28–39.

[5] J. Ding, R. Hall, J. Byrne, Effects of stress ratio and temperature on fatigue crack growth in a Ti-6Al-4V alloy, Int. J. Fatigue. 27 (2005) 1551–1558.

[6] L. Xiaolong, S. Chengqi, H. Youshi, Effects of stress ratio on high-cycle and very-high-cycle fatigue behavior of a Ti-6Al-4V alloy, Mater. Sci. Eng. A. 622 (2015) 228–235.

[7] T. Goswami, Fatigue crack growth behavior of Ti-6Al-4V alloy forging, Mater. Des. 24 (2003) 423–433.

[8] J. Petit, W. Berata, B. Bouchet, Fatigue crack growth behavior of Ti-6Al-4V in high vacuum, Scr. Metall. Mater. 26 (1992) 1889–1894.

[9] D.. Neal, P.. Blenkinsop, Internal fatigue origins in α-β Titanium alloys, Acta Metall. 24 (1976) 59–63.

[10] R.. Ritchie, D.. Davidson, B.. Boyce, J.. Campbell, O. Roder, High-cycle fatigue of Ti-6Al-4V, Fatigue Fract. Eng. Mater. Struct. 22 (1999) 621–631.

[11] O. Brend, Modeling the fatigue crack growth behavior of Ti-6Al-4V by considering grain size and stress ratio, Mater. Sci. Eng. A. 528 (2011) 5983–5992.

[12] N.. Arakere, T. Goswami, J. Krohn, N. Ramachandran, High temperature fatigue crack growth behavior of Ti-6Al-4V, High Temp. Mater. Process. 21 (2002) 229–235.

[13] J.. Newman, An improved method of collocation for the stress analysis of cracked plates with various shaped boundaries, Virginia, 1971.

[14] N.. Dowling, Notched member fatigue life predictions combining crack initiation and propagation, Fatigue Enigneering Mater. Struct. 2 (1979) 129–138.

[15] S. Suresh, Fatigue crack deflections and fracture surface contact: micromechanical models, Metall. Trans. 16A (1985) 249–260.

[16] P. Paris, F. Erdogan, A critical analysis of crack propagation laws, J. Basic Eng. 85 (1963) 528–534.

[17] R. Thomson, Solid state Physics, Academic press, Orlando, 1986.

[18] M. Tanaka, A. Fuji, H. Noguchi, K. Higashida, Thermally activated processes of fatigue crack growth in steels, Philos. Mag. Lett. 94 (2014) 95–102.

Chapter 5 Conclusions

In this thesis, the fundamental deformation mechanisms behind thermally activated processes in bimodal Ti-6Al-4V were addressed under both uniform monotonic loads and cyclic loads.

In Chapter 1, it was focused on overviewing on titanium alloys and their mechanical properties. As the present thesis focuses on the α+β alloy of bimodal Ti-6Al-4V, details of deformation modes in individual α and β phase, and mechanical properties of three types of alloys were reviewed such as α alloys of CP-Ti and Ti-Al, a β alloy of Ti-V, and an α+β alloy of Ti-6Al-4V. The effects of several parameters such as microstructural parameters, processing histories, heat treatments, mechanical variables in case of fatigue were focused.

In Chapter 2, the temperature dependence on the fundamental mechanical properties under uniform loads was investigated. Ti-6Al-4V exhibits strong temperature dependence of yield stress and effective stress. They decrease with increasing temperature, demonstrating the change in trend approximately at 325 K with some scattering in between temperature range of 225 K and 300K. The temperature dependence of activation volume showed an inverse temperature dependence in the temperature range between 225 K and 300 K. Temperature dependence of activation enthalpy was also measured, indicating that both basal and prismatic slips reasonably equal in the contribution to the yielding. The change in the trend of effective stress anticipates that it is due to the change in controlling mechanisms behind yielding at between 225 K and 300 K.

In Chapter 3, the change in the trend of the temperature dependence of deformation mechanisms as expected in Chapter 2 was further investigated by analyzing the traces of slips that appeared on specimen surfaces after 0.5 % tensile deformation. The activated slip systems were obtained experimentally by analyzing slip traces and Schmid factor distributions at three

temperatures *viz.,* low temperatures: 77 K, middle temperatures: 225 K and high temperatures: 550 K. It has been determined that basal slips are dominant at 77K, both basal and prismatic slips were apparently identical at 225 K while pyramidal slips were dominant at 550 K. Taylor factor analysis attributed to the activated slip systems by recognizing the contribution of each slip system to the macroscopic deformation at a given temperature. Under constant strain, it was found that the Taylor factor from total slip systems increased with temperature, indicating that the greater magnitude of activated slip systems contributed to the macroscopic deformation at higher temperature. The increase in total Taylor factor from 77 K to 225 K is due to the increase in individual Taylor factor of prismatic and pyramidal while the increase in Taylor factor of pyramidal contributes to the total increase of Taylor factor from 225 K to 550 K. Conclusively, the change in temperature dependence of effective stress approximately at 325 K corresponds to the onset of the pyramidal slips. Therefore, the change in the trend of effective stress can be explained by the change in activated slip systems.

In Chapter 4, the change in mechanical properties of Ti-6Al-4V under cyclic loads was investigated. The study is focused on the temperature dependence of fatigue crack propagation by changing the stress ratio. The effect of stress ratio on the temperature dependence of fatigue crack propagations was investigated in bimodal Ti-6Al-4V. According to Arrhenius law, crack growth rate increases with temperature due to increase in dislocation velocity when the crack growth rate is expected to be controlled by dislocation glide. However, there is no temperature dependence of the fatigue crack growth rate in the specimens with R = 0.1, 0.7, and 0.8 while there is temperature dependence in the specimen with R = 0.9. The temperature dependence of fatigue crack propagation at different stress ratios can be explained by the assumptions that the fatigue crack is controlled by work-hardening mechanism in the conditions of $R \leq 0.8$ while it is controlled by dislocation glide at R = 0.9.

In Chapter 5, summary of the thesis has been demonstrated in the perspective of understanding thermally activated processes during deformation of bimodal Ti-6Al-4V under monotonic deformation and cyclic deformation in accordance with investigation of temperature dependence of mechanical properties. The change in the trend of temperature dependence of effective stress has been experimentally ascertained to be associated with the change in activated slip systems. Basal, prismatic, and pyramidal slips contributed majorly to the macroscopic deformation pertaining to the different temperatures. The controlling mechanisms behind temperature dependence of fatigue crack propagation under cyclic loads at different stress ratios have been postulated as the mechanism which is similar to the dislocation activity of work-hardening at lower stress ratios. The controlling mechanism at higher stress ratio has been associated to the dislocation glide.